Aalto University
School of Science

Master's programme in Engineering Physics

Resonance valence bond superconductivity and quantum critical points in multiband systems

Eeli Lamponen

Master's Thesis
2023

Aalto University
School of Science

Author Eeli Lamponen

Title Resonance valence bond superconductivity and quantum critical points in multiband systems

Degree programme Engineering Physics

Major Engineering Physics

Supervisor Prof. Päivi Törmä

Advisor Dr. Kukka-Emilia Huhtinen

Date 28 February 2023 **Number of pages** 68 **Language** English

Abstract

Resonance valence bond states are quantum states where electrons on neighboring lattice sites form bonds with each other via a spin interaction. These pairs of electrons can act as superconducting charge carriers, and models with resonance valence bonds have been used to predict high critical temperatures in superconductors. In this thesis, we study the resonance valence bond interaction as an alternative to the conventional on-site interaction in Bardeen-Cooper-Schrieffer theory in the flat and multiband context. Using a mean-field approach, we find that the transition to a resonance valence bond state, where Cooper pairs can form, sometimes requires a non-zero critical interaction strength.

Cooper pairs are most easily formed near the Fermi surface. We find that with the resonance valence bond interaction, the localization properties of the Bloch states become important, as in some instances the electrons at the Fermi surface are localized on non-neighboring lattice sites, preventing the formation of Cooper pairs. Notably, this is the case for a certain class of lattices, including bipartite flat band models. Flat bands are dispersionless Bloch bands where the density of states diverges, and they have thus been predicted to enhance superconducting effects in models with on-site interactions. In contrast, we show that the flat band is of no benefit in some models, for instance in the Lieb lattice, since electrons on the flat band are not able to interact with each other. To take the Bloch state localization properties into account, instead of using the density of states, we propose a concept called the weighted density of pairs as an improved measure for counting candidate Cooper pairs at the Fermi surface.

Under an assumption about the symmetry of the transition order parameters, we also derive an analytical upper bound for the critical interaction strength. Results for various lattices show that while the assumption is not always correct, the upper bound still often closely approximates the true critical value, providing a method to estimate the transition point using only properties of the Bloch states.

The results of this thesis advance the understanding of the formation of Cooper pairs, and can be of help in the search of high-temperature superconductors. In particular, we have shown that combining resonance valence bond interactions and flat bands, both of which are studied in hopes of finding increased critical temperatures, is a nontrivial task.

Keywords superconductivity, resonance valence bond, quantum criticality

Aalto-yliopisto
Perustieteiden
korkeakoulu

Tekijä Eeli Lamponen

Työn nimi Suprajohtavuus resonanssivalenssisidoksilla ja kvanttikriittiset pisteet monen energiavyön systeemeissä

Koulutusohjelma Engineering Physics

Pääaine Engineering Physics

Työn valvoja Prof. Päivi Törmä

Työn ohjaaja TkT Kukka-Emilia Huhtinen

Päivämäärä 28.2.2023 **Sivumäärä** 68 **Kieli** englanti

Tiivistelmä

Resonanssivalenssisidostila on kvanttitila, jossa vierekkäisillä hilapisteillä olevat elektronit muodostava sidoksia toisensa kanssa spin-vuorovaikutuksen avulla. Näin muodostuvat parit voivat kuljettaa supravirtaa, ja resonanssivalenssisidosmallien avulla on ennustettu korkeita kriittisiä lämpötiloja suprajohteissa. Tässä diplomityössä tutkitaan resonanssivalenssisidosvuorovaikutuksia vaihtoehtona tavallisemmin tutkituille hilapisteen sisäisille vuorovaikutuksille Bardeen-Cooper-Schrieffer-teoriassa usean ja litteiden energiavöiden tapauksessa. Malleja simuloidaan keskeiskenttäteorian avulla keskittyen erityisesti kriittiseen vuorovaikutusvoimakkuuteen, jossa systeemi siirtyy normaalitilasta resonanssivalenssisidostilaan, jossa Cooperin pareja voi muodostua.

Cooperin pareja muodostuu helpoiten Fermi-pinnan läheisyydessä. Työssä saatujen tulosten perusteella resonanssivalenssisidosvuorovaikutuksilla myös Bloch-tilojen lokalisaatio-ominaisuudet ovat tärkeitä, sillä joissain tilanteissa Fermi-pinnan elektronit eivät ole lokalisoituneita vierekkäisille hilapisteille, mikä estää Cooperin parien muodostumisen. Näin tapahtuu erityisesti eräille litteän vyön malleille. Litteä vyö on tasainen Bloch-energiavyö, jolla tilatiheys on ääretön, ja niiden on siten ennustettu vahvistavan suprajohtavuutta kun vuorovaikutukset ovat hilapisteen sisäisiä. Litteästä vyöstä ei kuitenkaan ole joillekin hiloille, kuten Lieb-hilalle, hyötyä, sillä vyöllä olevat elektronit eivät voi vuorovaikuttaa keskenään. Tilatiheyden sijaan työssä määritellään suure nimeltään painotettu paritiheys, jotta Bloch-tilojen ominaisuudet voidaan ottaa huomioon arvioitaessa potentiaalisten Cooperin parien määrää Fermi-pinnalla.

Työssä johdetaan myös analyyttinen yläraja kriittiselle vuorovaikutusvoimakkuudelle käyttäen tiettyä oletusta transition järjestysparametrien symmetriasta. Useille eri hiloille saatujen tulosten perusteella yläraja on usein lähellä oikeaa kriittistä arvoa, vaikka käytetty symmetriaoletus ei aina pidäkään paikkaansa. Ylärajaa voi siten käyttää kriittisen arvon arviointiin tekemättä kokonaisia simulaatioita.

Työn tulokset edistävät ymmärrystä Cooperin parien muodostumisesta, ja voivat siten olla avuksi etsittäessä korkeampia kriittisiä lämpötiloja suprajohteille. Erityisesti tulokset osoittavat, että vaikka sekä resonanssivalenssisidosvuorovaikutuksia että litteitä vöitä tutkitaan kriittisten lämpötilojen kasvattamisen toivossa, niiden yhdistäminen on joissain tapauksissa haastavaa.

Avainsanat suprajohtavuus, resonanssivalenssisidos, kvanttikriittinen piste

Contents

1 Introduction

1.1 From Conventional BCS Theory to Resonance Valence Bonds

Ever since the discovery of superconductivity by Onnes in 1911 [1], the grand goal of the related research has been to increase the critical temperatures of superconductors. While nearly-room-temperature ($T_c \approx 200$ K) superconductivity has been achieved [2,3], such results require pressures on the order of gigapascals, 10^6 times the atmospheric pressure. At ambient pressures, critical temperatures between 0-140 K have been reported [4–7]. While unable to explain many of the recent high-temperature superconductors (for many of which the superconducting mechanism is not known), Bardeen-Cooper-Schrieffer (BCS) theory [8] still offers the most detailed picture of superconductivity, 60 years after its creation. The idea behind BCS theory is the existence of bound states for pairs of electrons: when a such Cooper pair forms, the momenta of the electrons become correlated, and a finite energy is required to break up the pair. The Cooper pairs act as charge carriers, able to carry current without being obstructed by energy fluctuations that are smaller than their pairing energy, which can lead to dissipationless current, the defining phenomenon of superconductivity.

The concept of a Cooper pair originates from the work by Cooper in 1956 [9], where, by considering a simple system of two electrons in the presence of a Fermi sea, it was shown that any finite attractive interaction, no matter how small, is enough to create a bound state. The key here is that the interaction has to be *attractive*, which seems to cause a problem: the Coulomb interaction between two electrons, both with a negative charge, is repulsive. Nevertheless, BCS theory was successful in explaining experimental features, such as the existence of a critical temperature and a band gap, as well the isotope effect (i.e. an electrical conductivity dependent on the nuclear mass) [10] of the superconductors that were known at the time, which led to the general acceptance of the concept of *phonon-mediated attraction*. Phonon-mediated attraction is the explanation of how an effective attractive interaction between electrons could form in the original BCS theory, and the idea of it is, roughly, the following: when an electron, a negatively charged particle, moves in a lattice of atoms, it interacts with the positively charged protons in the atom nuclei via the Coulomb interaction. From the point of view of the electron, the nuclei, being much heavier than the electron, are approximately stationary. However, this interaction causes the nuclei to vibrate slightly. As the nuclei also interact with each other, this creates a collective mode of vibration to the lattice, or a phonon. As a result, the charge density in the lattice is slightly more positive in the region where the electron passed by, which can be felt by another electron as an attraction. If this mechanism is strong enough to overcome the direct Coulomb repulsion between the electrons, the net effect can be an attractive interaction between them.

BCS theory is typically built on the famous Hubbard model [11–13], which, via a tight-binding approximation, considers electrons to be mostly bound to a single atomic nucleus and to only occasionally tunnel (or *hop*) to another nearby nucleus. In the model, the repulsive Coulomb interaction is applied only to electrons at the same lattice site. This is known as the Hubbard-U interaction, where U typically denotes

the interaction strength. When the interaction is repulsive, the dynamics of the model are determined by the competition between kinetic effects (particles lowering their energy by tunneling to other sites) and the on-site repulsion. When the interaction is attractive, superconducting solutions emerge. Since the Hubbard model has not been analytically solved in dimensions greater than one, a popular approach to tackle it is to use a mean-field approximation, which ignores quantum fluctuations. This is also the approach we use in this work.

In conventional BCS theory, on a dispersive band, the critical temperature is $T_c \propto \exp(-1/(|U|n(E_F)))$, where $n(E_F)$ is the density of states at the Fermi surface. In other words, T_c is exponentially suppressed at low interaction strengths. While this situation has been predicted to improve to $T_c \propto |U|$ on dispersionless flat bands with a diverging density of states [14, 15], this issue has led researchers to seek alternatives to the phonon-mediated attraction to explain experimentally discovered materials with critical temperatures that are seemingly higher than what conventional BCS theory can explain. One of these mechanisms is the *resonance valence bond* (RVB) interaction, which will be the main topic in this thesis. The concept of a valence bond originates in chemistry, describing a bond between the valence electrons of two atoms. In an RVB state, the lattice is divided into pairs of neighboring sites, the electrons of which form bonds with one another, and the total quantum state is a superposition over all such pairings. The RVB state was first proposed to explain the superconducting properties of the compound La_2CuO_4 [5] by Anderson in 1987 [16], but the concept has its roots [17] in Heisenberg's antiferromagnetic spin exchange interaction [18] and the t-J model originally developed by Chao and Spalek in 1978 [19].

Why do electrons form bonds with electrons on neighboring sites, instead of with those on the same site like in the phonon-mediated attraction? It turns out that this behaviour, too, is obtained from the Hubbard model, but instead of explicitly attractive interactions, one considers the limit of very strong repulsive interactions (typically written as $U \gg t$, where t denotes the scale of the hopping processes). Consider a half-filled system, i.e. one electron per site, in the extreme case $t = 0$. This is the atomic limit, where each electron is strictly bound to a single atom. If we now add a small t, the hoppings are still highly suppressed due to the large penalty ($\sim U$) of having double occupancy on a single lattice site, which in a half-filled system would necessarily happen if any electron hopped away from the atom it is bound to. Treating the kinetic effects perturbatively, the leading term is of second order, and it describes a "virtual hopping" of an electron to a neighboring site and back. Intuitively, we can picture the electron to briefly be at the neighboring site, but it cannot stay there because of the strong repulsion. From a more formal standpoint, what is meant is that the energy of the electron is lowered by being in the superposition of staying still and being in this virtual second-order hopping process. Now, due to the Pauli exclusion principle, this process is only possible if the spins of the neighboring electrons are of opposite signs. This interplay between a strong Coulomb repulsion and the Pauli principle can then create an effective attractive nearest-neighbour interaction between electrons with opposite spins, favoring the creation of singlet bonds. As described by Anderson [16], at exactly half-filling, the singlet pairs are stationary (again due to the Pauli principle), and the system is a Mott insulator, but at small non-zero dopings, the

pairs can start to move and the system transitions to a superconductor.

In the past decades, there has been plenty of research activity on models with the RVB interaction [20–29], often featuring exotic, unconventional forms of superconductivity, and predictions of high critical temperatures. In some cases the predictions reach up to the order of 1000 K [30], way past room temperature. While results from experiments are still of the order of 100 K and the ability of the RVB model to estimate critical temperatures has subsequently been put into question [31, 32], the resonating valence bond mechanism is still seen as one of the possible paths to high-T_c superconductivity. For a review of the RVB theory and its relation to experiments, see, e.g. Refs. [26, 29].

1.2 Quantum Criticality: Minimal Interaction Strength

In isolation, the picture of an electron interacting with another is simple enough: they repel each other via the Coulomb interaction. However, in larger interacting systems, the effective interaction can be attractive due to, e.g., the phonon-mediated attraction or resonance valence bonds. As shown by Cooper in 1956 [9], any non-zero, no matter how weak, attractive interaction between two electrons is enough for them to be able to form a Cooper pair. Thus, while the effects of the attraction mechanisms need to overcome the Coulomb repulsion for the net-effect to be an attraction, they don't need to be much larger than that. While increased interaction strength typically enhances pairing, one indeed often obtains small-but-non-zero order parameters for any non-zero attraction.

There is, however, an important exception, related to the properties of the Fermi surface. As was the premise in Cooper's two-electron problem, and as is evident by considering a weak interaction as a perturbation to the non-interacting case, electrons at the Fermi surface are the most susceptible to pairing. What happens, then, if there are no electrons near the Fermi surface? This could be the case, for example, in gapped systems if the Fermi energy is set in the band gap, or at Dirac points, which is a band-touching point (BTP) where the dispersion near the BTP is linear. The common factor of these scenarios is that the density of states at the Fermi surface is zero (for a Dirac point, this holds for dimensions greater than 1), i.e. there are either zero or a vanishingly small amount of states that could form the Cooper pairs. There are indeed (theoretical and/or computational) results that indicate that in these situations there is a minimal non-zero interaction strength that is required before pairing can occur [23–25, 33–40]. In other words, the system undergoes a quantum phase transition from a normal state to a BCS or an RVB state at a critical value of the interaction strength. The quantum critical point (QCP) is often present even in the absence of any thermal fluctuations, i.e. at zero temperature. In simplified terms, one can think that forming a pair induces an energy cost related to the difference between the energy of the pairing states and the Fermi energy, which has to be compared to the scale of the pairing energy, set by the interaction strength. Since there are no states available at the Fermi surface, a finite interaction strength is required before the forming a Cooper pair is energetically advantageous for a large enough number of pairs for the system as a whole to be able to transition to a BCS or an RVB state. This

explanation will be built further on in Section 3.2.

The opposite limit to the above is that of flat bands, i.e. energy bands where the dispersion is constant, and the density of states diverges. As mentioned before, the critical temperature of a flat-band system is predicted to depend linearly on the interaction strength, instead of being exponentially suppressed [14, 15]. This means that superconductivity is enhanced, especially for small interactions strengths [41–46].

However, this discussion of the Fermi surface, a momentum-space feature, bypasses an important point: what happens in real space? Are the particles localized on such lattice sites that they can interact in the first place, i.e. are the particles that could form a Cooper pair at least partially localized on the same site (for on-site pairing) or on neighboring sites (for nearest-neighbour pairing)? This question arises specifically in systems with multiple orbitals, i.e. in multiband systems, since in a system with only a single orbital, with a typical assumption of translational symmetry between unit cells, every lattice site is equivalent and the localization properties of the particles are trivial. On the other hand, with multiple orbitals, the particles can be localized across the orbitals in a unit cell in a nontrivial way, even if translational symmetry between unit cells is not broken. However, using a second typical assumption of time-reversal symmetry (TRS), the situation again becomes very simple even in multiband systems if on-site interactions are considered. TRS implies that a particle having a non-zero wave function amplitude on a given lattice site necessarily means that its main pairing counterpart, a particle with the same energy but opposite momentum and spin, also has the same non-zero wave function amplitude at the same site. This means that with on-site interactions, we can indeed often only focus on the Fermi surface and its density of states; wherever a particle is localized, there is always a pairing partner available at the same lattice site. The complicated case is that of a multiband system with nearest-neighbour interactions, such as RVB. In this case there is no guarantee that a pair can be formed between two states even if both of them are exactly on the Fermi surface, since for the particles to be able to interact in the first place, they need to be at least partially localized on neighboring states, which is not necessarily the case. This means that in addition to the dispersion relations, i.e. the Bloch energies, we also need to take into account properties of the Bloch states themselves.

While QCPs caused by a vanishing density of states at the Fermi surface have been predicted in the literature previously [23–25, 33–39], to the best of our knowledge the matter of Bloch state localization has not been thoroughly investigated before. It turns out that the localization properties can have dramatic consequences. As we will show analytically in Section 3.1 and numerically in Section 5, there is a class of flat-band models where the Bloch states are localized in such a way that particles at the flat band cannot interact with each other at all, rendering the associated divergence of the density of states almost useless when it comes to pairing. This is an important result, since both flat bands and the RVB interaction as a whole are used in hopes of achieving high-T_c superconductivity, but in this case the effect of combining the two is the opposite, as the RVB interaction largely cancels out the benefits of the flat band. However, this is not an unavoidable consequence of a flat band, as we show that for a different model without localization issues, it is indeed possible to combine RVB pairing with a flat band without inducing a QCP.

1.3 Goal and Outline of the Thesis

The goal of this thesis is to study RVB superconductivity, alongside conventional BCS superconductivity. We find that RVB interactions induce a phase transition from a normal to an RVB state at a finite interaction strength for multiple models. At the same time, we find that for the same models with the more standard on-site interactions, any non-zero interaction strength is enough to yield a superconducting solution. The rest of the thesis is dedicated to developing theory around why and when such a phase transition occurs, and to assessing the predictions of said theory by comparisons to numerical simulations.

The rest of this thesis is organized as follows. In Sections 2.1-2.4, we employ the RVB interaction on a multi-band BCS-type Hamiltonian, and, using a mean-field approach, introduce the superconducting order parameter and derive the corresponding gap equation needed to solve it. In Section 3.1, we show some general results related to the Bloch state localization for a class of flat band models, namely semi-bipartite lattices with unequal lattice sizes, building on the results of Ref. [47]. Notably, the flat-band particles in these models cannot interact with each other. In Section 3.2 we derive an analytical upper bound for the value of the interaction strength at which the phase transition from a normal to a BCS or an RVB state occurs. In Section 4, we highlight some details regarding the numerical simulation of our models, while in Section 5 we show results from said simulations and assess the validity of the theory developed in Sections 2-3. Finally, in Section 6 conclude by recapping our results and discussing their general features.

2 Theoretical Background

2.1 The Model Hamiltonian

Our model is defined by the multi-band second-quantized Hubbard Hamiltonian

$$\hat{H} = \hat{H}_{\text{kin}} - \mu\hat{N} + \hat{H}_{\text{int}}, \tag{2.1}$$

where $\hat{H}_{\text{kin}} = \sum_{\boldsymbol{i}\alpha,\boldsymbol{j}\beta}\sum_{\sigma} t^{\sigma}_{\boldsymbol{i}\alpha\boldsymbol{j}\beta}\hat{c}^{\dagger}_{\boldsymbol{i}\alpha\sigma}\hat{c}_{\boldsymbol{j}\beta\sigma}$ is the kinetic part, μ is the chemical potential and $\hat{N}$ the total particle number operator. The unit cells are labeled with integer-valued index vectors $\boldsymbol{i}, \boldsymbol{j}$, so that in e.g. a 2D system the position $\boldsymbol{R_i}$ of unit cell $\boldsymbol{i}$ is given by $\boldsymbol{R_i} = i_x\boldsymbol{a_x} + i_y\boldsymbol{a_y}$, with i_x, i_y the components of $\boldsymbol{i}$ and $\boldsymbol{a_x}, \boldsymbol{a_y}$ the basis vectors of the lattice. The orbitals inside unit cells are labeled with α and β, while σ labels the spin. Then, $\hat{c}^{\dagger}_{\boldsymbol{i}\alpha\sigma}$ ($\hat{c}_{\boldsymbol{i}\alpha\sigma}$) is the creation (annihilation) operator for site $\boldsymbol{i}\alpha$ and spin σ, while $t^{\sigma}_{\boldsymbol{i}\alpha\boldsymbol{j}\beta}$ gives the hopping amplitude from site $\boldsymbol{i}\alpha$ to $\boldsymbol{j}\beta$ for spin σ. In this work, we will mostly consider systems with only nearest-neighbour hoppings, corresponding to setting $t^{\sigma}_{\boldsymbol{i}\alpha\boldsymbol{j}\beta} = 0$ if $\boldsymbol{i}\alpha$ and $\boldsymbol{j}\beta$ are not nearest neighbours. All of the specific systems that we will eventually consider fulfill time-reversal symmetry (TRS), which for the Hamiltonian means $t^{\downarrow}_{\boldsymbol{i}\alpha\boldsymbol{j}\beta} = (t^{\uparrow}_{\boldsymbol{i}\alpha\boldsymbol{j}\beta})^*$. The theory in this section will be developed in general without using this assumption, but we will later specialize some results to systems with TRS.

For the interaction term, we consider two possibilities. The first one is the more standard, local on-site interaction

$$\hat{H}_{\text{int}} = \hat{H}_{\text{on-site}} = -U\sum_{\boldsymbol{i}\alpha}\hat{c}^{\dagger}_{\boldsymbol{i}\alpha\uparrow}\hat{c}^{\dagger}_{\boldsymbol{i}\alpha\downarrow}\hat{c}_{\boldsymbol{i}\alpha\downarrow}\hat{c}_{\boldsymbol{i}\alpha\uparrow}, \tag{2.2}$$

where $U > 0$ is the interaction strength, corresponding to an attractive interaction.

The second option for the interaction term is the nearest-neighbour RVB interaction

$$\hat{H}_{\text{int}} = \hat{H}_{\text{RVB}} = -\frac{J}{2}\sum_{<\boldsymbol{i}\alpha,\boldsymbol{j}\beta>}\hat{h}^{\dagger}_{\boldsymbol{i}\alpha\boldsymbol{j}\beta}\hat{h}_{\boldsymbol{i}\alpha\boldsymbol{j}\beta}, \tag{2.3}$$

where $\hat{h}_{\boldsymbol{i}\alpha\boldsymbol{j}\beta} = \hat{c}_{\boldsymbol{i}\alpha\uparrow}\hat{c}_{\boldsymbol{j}\beta\downarrow} - \hat{c}_{\boldsymbol{i}\alpha\downarrow}\hat{c}_{\boldsymbol{j}\beta\uparrow}$ so that $\hat{h}_{\boldsymbol{i}\alpha\boldsymbol{j}\beta}/\sqrt{2}$ is the singlet pair annihilation operator, and $J > 0$ is the interaction strength, again making the interaction attractive. The sum is taken over nearest neighbours, as denoted by $< \boldsymbol{i}\alpha, \boldsymbol{j}\beta >$.

Before starting to manipulate the Hamiltonian, we pause for a moment to consider the origin of Eq. (2.3). As discussed in Section 1, the RVB interaction is obtained as the strongly repulsive limit of the standard Hubbard model. To achieve this, one starts with the Hubbard Hamiltonian and performs a Schrieffer-Wolff transformation [48,49], which yields a perturbative series in powers of t with the first-order term diagonalized away, where t parameterizes the scale of the hopping amplitudes. The second-order term describes the RVB pairing and has a coefficient of $J = 4t^2/U$. Higher order

terms can be added, but with the assumption of strong repulsion $U \gg t$ they are often omitted. The pairing term has the form of Heisenberg's spin exchange interaction $J \sum_{<i\alpha, j\beta>} \boldsymbol{S}_{i\alpha} \cdot \boldsymbol{S}_{j\beta}$ [18], where $\boldsymbol{S}$ is a spin operator, which together with the kinetic Hamiltonian yields the t-J model mentioned in Section 1 [19]. An alternative form for the pairing term is the one we use in Eq. (2.3) [23, 29, 50]. The latter form nicely illustrates how the antiferromagnetic spin interaction favors the formation of singlet pairs.

With the RVB interaction expressed in terms of fermionic operators, the Hamiltonian is mathematically speaking very similar to the conventional BCS Hamiltonian with on-site interactions. In particular, one can perform a mean-field decoupling and a Bogoliubov-type transformation similarly to what is typically done in conventional BCS theory to obtain a superconducting order parameter for the singlet pairs. This will be done in the following. The corresponding treatment for the on-site pairing term is very similar, and widely available in the literature. While we will handle the RVB interaction step-by-step, we refer the reader to e.g. Ref. [41] for the details of the on-site interaction.

Let us now proceed by making a mean-field approximation for the interaction term. Specifically

$$\hat{H}_{\text{on-site}} \approx \sum_{i\alpha} \left(\Delta_{i\alpha} \hat{c}^{\dagger}_{i\alpha\uparrow} \hat{c}^{\dagger}_{i\alpha\downarrow} + \Delta^{*}_{i\alpha} \hat{c}_{i\alpha\downarrow} \hat{c}_{i\alpha\uparrow} + \frac{|\Delta_{i\alpha}|^2}{J} \right), \tag{2.4}$$

$$\hat{H}_{\text{RVB}} \approx \sum_{<i\alpha, j\beta>} \left(\Delta_{i\alpha j\beta} \hat{h}^{\dagger}_{i\alpha j\beta} + \Delta^{*}_{i\alpha j\beta} \hat{h}_{i\alpha j\beta} + \frac{2}{J} |\Delta_{i\alpha j\beta}|^2 \right), \tag{2.5}$$

where $\Delta_{i\alpha} = -J \langle \hat{c}_{i\alpha\downarrow} \hat{c}_{i\alpha\uparrow} \rangle$ and $\Delta_{i\alpha j\beta} = -\frac{J}{2} \langle \hat{h}_{i\alpha j\beta} \rangle$ are the on-site and RVB pairing order parameters, respectively. Here and from now on, we switch the label of the interaction strength for the on-site interaction from the more traditional U to J for consistency with the RVB interaction, and to avoid unnecessary notation.

To take advantage of the periodicity of the system, we transform the Hamiltonian into momentum-space via a Fourier transform $\hat{c}_{i\alpha\sigma} = \frac{1}{\sqrt{N_c}} \sum_{\boldsymbol{k}} e^{i\boldsymbol{k} \cdot (\boldsymbol{R}_i + \boldsymbol{\delta}_\alpha)} \hat{c}_{\boldsymbol{k}\alpha\sigma}$, where $\hat{c}_{\boldsymbol{k}\alpha\sigma}$ annihilates a particle with quasi-momentum $\boldsymbol{k}$ on orbital α and with spin σ, $\boldsymbol{\delta}_{\boldsymbol{\alpha}}$ is the relative position of orbital α within the unit cell, N_c is the number of unit cells in the system, and the sum runs over the first Brillouin zone. First, we transform the interaction term. As the first term on the right-hand side of Eq. (2.5) is just the Hermitian conjugate of the second term, let us focus only on the latter for now. We will define $\hat{h}_{\boldsymbol{k}\alpha\boldsymbol{k}'\beta} = \hat{c}_{\boldsymbol{k}\alpha\uparrow} \hat{c}_{\boldsymbol{k}'\beta\downarrow} - \hat{c}_{\boldsymbol{k}\alpha\downarrow} \hat{c}_{\boldsymbol{k}'\beta\uparrow}$, as well as the indicator variable

$$I_{i\alpha j\beta} = \begin{cases} 1 & \text{if } \boldsymbol{i}\alpha \text{ and } \boldsymbol{j}\beta \text{ are nearest neighbours,} \\ 0 & \text{otherwise.} \end{cases} \tag{2.6}$$

With the latter definition, we can write the summation over nearest neighbours as

$$\sum_{<i\alpha,j\beta>} \rightarrow \frac{1}{2}\sum_{i\alpha j\beta} I_{i\alpha j\beta}, \tag{2.7}$$

where the factor of $\frac{1}{2}$ is to avoid double counting the nearest-neighbour pairs. With these definitions, and assuming that the $\Delta_{i\alpha j\beta}$ are translationally invariant, the second term in Eq. (2.5) becomes

$$\begin{aligned}
&\sum_{<i\alpha,j\beta>} \Delta^*_{i\alpha j\beta}\hat{h}_{i\alpha j\beta} \\
=&\frac{1}{2}\sum_{i\alpha j\beta} I_{i\alpha j\beta}\Delta^*_{i\alpha j\beta}\hat{h}_{i\alpha j\beta} \\
=&\frac{1}{2N_c}\sum_{i\alpha j\beta}\sum_{kk'} I_{i\alpha j\beta}\Delta^*_{i\alpha j\beta}e^{i[\boldsymbol{k}\cdot(\boldsymbol{R}_i+\boldsymbol{\delta}_\alpha)+\boldsymbol{k}'\cdot(\boldsymbol{R}_j+\boldsymbol{\delta}_\beta)]}\hat{h}_{k\alpha k'\beta} \\
=&\frac{1}{2N_c}\sum_{i\alpha j\beta}\sum_{kk'} I_{0\alpha j\beta}\Delta^*_{0\alpha j\beta}e^{i[\boldsymbol{k}\cdot(\boldsymbol{R}_i+\boldsymbol{\delta}_\alpha)+\boldsymbol{k}'\cdot(\boldsymbol{R}_{j+i}+\boldsymbol{\delta}_\beta)]}\hat{h}_{k\alpha k'\beta} \\
=&\frac{1}{2N_c}\sum_{j\alpha\beta}\sum_{kk'} I_{0\alpha j\beta}\Delta^*_{0\alpha j\beta}e^{i[\boldsymbol{k}\cdot\boldsymbol{\delta}_\alpha+\boldsymbol{k}'\cdot(\boldsymbol{R}_j+\boldsymbol{\delta}_\beta)]}\left(\sum_i e^{i(\boldsymbol{k}+\boldsymbol{k}')\cdot\boldsymbol{R}_i}\right)\hat{h}_{k\alpha k'\beta} \\
=&\frac{1}{2}\sum_{j\alpha\beta}\sum_{k} I_{0\alpha j\beta}\Delta^*_{0\alpha j\beta}e^{i\boldsymbol{k}\cdot(\boldsymbol{R}_j+\boldsymbol{\delta}_\beta-\boldsymbol{\delta}_\alpha)}\hat{h}_{-k\alpha k\beta} \\
=&\frac{1}{2}\sum_{j\alpha\beta}\sum_{k} I_{0\alpha j\beta}\Delta^*_{0\alpha j\beta}e^{i\boldsymbol{k}\cdot\boldsymbol{r}^{\Delta}_{0\alpha j\beta}}\hat{h}_{-k\alpha k\beta}
\end{aligned} \tag{2.8}$$

Here, we have used the translational invariance of both the indicator variables $I_{i\alpha j\beta}$ and the order parameters $\Delta_{i\alpha j\beta}$ and made an index-shift $\boldsymbol{j} \rightarrow \boldsymbol{j}+\boldsymbol{i}$ (on the fourth line), used $\boldsymbol{R}_{j+i} = \boldsymbol{R}_j + \boldsymbol{R}_i$ (on the fifth line), and used the Fourier-transform property $\sum_{\boldsymbol{i}} e^{i(\boldsymbol{k}+\boldsymbol{k}')\cdot\boldsymbol{R}_i} = N_c\delta_{\boldsymbol{k},-\boldsymbol{k}}$ (on the sixth line), where $\delta_{\boldsymbol{k},-\boldsymbol{k}}$ is the Kronecker delta. Here, $\boldsymbol{r}^{\Delta}_{0\alpha j\beta}$ denotes the translation vector from site 0α to $\boldsymbol{j}\beta$, i.e. $\boldsymbol{r}^{\Delta}_{0\alpha j\beta} = \boldsymbol{R}_j + \boldsymbol{\delta}_\beta - \boldsymbol{\delta}_\alpha$.

The whole interaction term thus becomes

$$\hat{H}_{\mathrm{RVB}} = \frac{1}{2}\sum_{j\alpha\beta}\sum_{k}\left(I_{0\alpha j\beta}\Delta^*_{0\alpha j\beta}e^{i\boldsymbol{k}\cdot\boldsymbol{r}^{\Delta}_{0\alpha j\beta}}\hat{h}_{-k\alpha k\beta} + \mathrm{H.c.}\right) + \frac{N_c}{J}\sum_{j\alpha\beta} I_{0\alpha j\beta}|\Delta_{0\alpha j\beta}|^2, \tag{2.9}$$

where the last term results from applying translational invariance to the last term on the right-hand side in Eq. (2.5).

Fourier transforming the (mean-field) on-site interaction $\hat{H}_{\text{on-site}}$, the kinetic part of the Hamiltonian $\hat{H}_{\mathrm{kin}}$, as well as the particle number operator $\hat{N}$, involve steps that are similar to the above. The results are

$$\hat{H}_{\text{on-site}} = \sum_{\boldsymbol{k}\alpha} \left(\Delta_\alpha \hat{c}^\dagger_{\boldsymbol{k}\alpha\uparrow} \hat{c}^\dagger_{-\boldsymbol{k}\alpha\downarrow} + \text{H.c.} \right) + \frac{N_c}{J} \sum_\alpha |\Delta_\alpha|^2, \tag{2.10}$$

$$\hat{H}_{\text{kin}} = \sum_{\boldsymbol{k}\alpha\beta\sigma} [H^\sigma_{\boldsymbol{k}}]_{\alpha,\beta} \hat{c}^\dagger_{\boldsymbol{k}\alpha\sigma} \hat{c}_{\boldsymbol{k}\beta\sigma}, \tag{2.11}$$

$$\mu\hat{N} = \mu \sum_{\boldsymbol{k}\alpha\sigma} \hat{c}^\dagger_{\boldsymbol{k}\alpha\sigma} \hat{c}_{\boldsymbol{k}\alpha\sigma}, \tag{2.12}$$

where translational invariance is assumed also for the on-site interaction order parameters, allowing us to write $\Delta_{i\alpha} = \Delta_\alpha$. Here, the $\boldsymbol{k}$-sums are again taken over the first Brillouin zone, and $[H^\sigma_{\boldsymbol{k}}]_{\alpha,\beta} = \sum_{\boldsymbol{j}} t^\sigma_{0\alpha\boldsymbol{j}\beta} e^{i\boldsymbol{k}\cdot\boldsymbol{r}^\Delta_{0\alpha\boldsymbol{j}\beta}}$. Throughout this work, $[\cdot]_{\alpha,\beta}$ is used to denote a matrix element. We note that in systems with TRS, i.e. with $t^\downarrow_{i\alpha\boldsymbol{j}\beta} = (t^\uparrow_{i\alpha\boldsymbol{j}\beta})^*$, we have $(H^\downarrow_{-\boldsymbol{k}})^* = H^\uparrow_{\boldsymbol{k}}$.

2.2 BdG-form of the Hamiltonian

Next, to move towards diagonalizing the Hamiltonian with a Bogoliubov transformation [51], we introduce a Nambu spinor $\hat{\boldsymbol{c}}_{\boldsymbol{k}} = (\hat{c}_{\boldsymbol{k}\alpha=1\uparrow}, \ldots, \hat{c}_{\boldsymbol{k}\alpha=n_{\text{orb}}\uparrow}, \hat{c}^\dagger_{-\boldsymbol{k}\alpha=1\downarrow}, \ldots, \hat{c}^\dagger_{-\boldsymbol{k}\alpha=n_{\text{orb}}\downarrow})$, where n_{orb} is the number of orbitals, and seek to express the Hamiltonian in Bogoliubov-de Gennes (BdG) form as $\sum_{\boldsymbol{k}} \hat{\boldsymbol{c}}^\dagger_{\boldsymbol{k}} H_{\text{BdG}}(\boldsymbol{k}) \hat{\boldsymbol{c}}_{\boldsymbol{k}}$, with

$$H_{\text{BdG}}(\boldsymbol{k}) = \begin{pmatrix} H^\uparrow_{\boldsymbol{k}} - \mu\mathbf{1} & \Delta_{\boldsymbol{k}} \\ \Delta^\dagger_{\boldsymbol{k}} & -(H^\downarrow_{-\boldsymbol{k}})^* + \mu\mathbf{1} \end{pmatrix}. \tag{2.13}$$

The BdG-Hamiltonian is given in block form. We denote the $n_{\text{orb}} \times n_{\text{orb}}$ identity matrix with $\mathbf{1}$. The order parameter matrix $\Delta_{\boldsymbol{k}}$ has the same dimensions. In systems with on-site interactions this matrix is diagonal and independent of $\boldsymbol{k}$, if translational invariance is assumed. With nearest-neighbour interactions, such as RVB, the order parameter matrix becomes non-diagonal and in general $\boldsymbol{k}$-dependent (even with translational invariance). The next goal is to determine the structure of $\Delta_{\boldsymbol{k}}$ with the RVB interaction. To do this, we expand the spinor-matrix-spinor multiplication as

$$\begin{aligned} \sum_{\boldsymbol{k}} \hat{\boldsymbol{c}}^\dagger_{\boldsymbol{k}} H_{\text{BdG}}(\boldsymbol{k}) \hat{\boldsymbol{c}}_{\boldsymbol{k}} = & \sum_{\boldsymbol{k}\alpha\beta} \left([H^\uparrow_{\boldsymbol{k}}]_{\alpha,\beta} \hat{c}^\dagger_{\boldsymbol{k}\alpha\uparrow} \hat{c}_{\boldsymbol{k}\beta\uparrow} - [H^\downarrow_{-\boldsymbol{k}}]^*_{\alpha,\beta} \hat{c}_{-\boldsymbol{k}\alpha\downarrow} \hat{c}^\dagger_{-\boldsymbol{k}\beta\downarrow} \right) \\ & - \mu \sum_{\boldsymbol{k}\alpha} \left(\hat{c}^\dagger_{\boldsymbol{k}\alpha\uparrow} \hat{c}_{\boldsymbol{k}\alpha\uparrow} - \hat{c}_{-\boldsymbol{k}\alpha\downarrow} \hat{c}^\dagger_{-\boldsymbol{k}\alpha\downarrow} \right) \\ & + \sum_{\boldsymbol{k}\alpha\beta} [\Delta_{\boldsymbol{k}}]^*_{\beta\alpha} \hat{c}_{-\boldsymbol{k}\alpha\downarrow} \hat{c}_{\boldsymbol{k}\beta\uparrow} + \text{H.c.}. \end{aligned} \tag{2.14}$$

The first row on the right-hand side corresponds to $\hat{H}_{\text{kin}}$. Specifically, by using the hermiticity of $H^\downarrow_{-\boldsymbol{k}}$ alongside fermionic anti-commutation relations and replacing $-\boldsymbol{k} \to \boldsymbol{k}$, we get

$$\sum_{\boldsymbol{k}\alpha\beta}\left([H^{\uparrow}_{\boldsymbol{k}}]_{\alpha,\beta}\hat{c}^{\dagger}_{\boldsymbol{k}\alpha\uparrow}\hat{c}_{\boldsymbol{k}\beta\uparrow}-[H^{\downarrow}_{-\boldsymbol{k}}]^{*}_{\alpha,\beta}\hat{c}_{-\boldsymbol{k}\alpha\downarrow}\hat{c}^{\dagger}_{-\boldsymbol{k}\beta\downarrow}\right)=\sum_{\boldsymbol{k}\alpha\beta\sigma}[H^{\sigma}_{\boldsymbol{k}}]_{\alpha,\beta}\hat{c}^{\dagger}_{\boldsymbol{k}\alpha\sigma}\hat{c}_{\boldsymbol{k}\beta\sigma}-\sum_{\boldsymbol{k}}\mathrm{Tr}\,H^{\downarrow}_{-\boldsymbol{k}}$$
$$=\hat{H}_{\mathrm{kin}}-\sum_{\boldsymbol{k}}\mathrm{Tr}\,H^{\downarrow}_{-\boldsymbol{k}}. \tag{2.15}$$

Similarly, the second row becomes

$$-\mu\sum_{\boldsymbol{k}\alpha}\left(\hat{c}^{\dagger}_{\boldsymbol{k}\alpha\uparrow}\hat{c}_{\boldsymbol{k}\alpha\uparrow}-\hat{c}_{-\boldsymbol{k}\alpha\downarrow}\hat{c}^{\dagger}_{-\boldsymbol{k}\alpha\downarrow}\right)=-\mu\hat{N}+n_{\mathrm{orb}}N_c\mu. \tag{2.16}$$

Thus, the task is to define $[\Delta_{\boldsymbol{k}}]_{\alpha,\beta}$ so that the final row matches up with $\hat{H}_{\mathrm{RVB}}$ (up to a possible constant). To achieve this, let us continue to manipulate $\hat{H}_{\mathrm{RVB}}$. The first term on the right-hand side in Eq. (2.9) gives

$$\begin{aligned}
&\frac{1}{2}\sum_{\boldsymbol{j}\alpha\beta}\sum_{\boldsymbol{k}}I_{0\alpha\boldsymbol{j}\beta}\Delta^{*}_{0\alpha\boldsymbol{j}\beta}e^{i\boldsymbol{k}\cdot\boldsymbol{r}^{\Delta}_{0\alpha\boldsymbol{j}\beta}}\hat{h}_{-\boldsymbol{k}\alpha\boldsymbol{k}\beta}\\
=&\frac{1}{2}\sum_{\boldsymbol{j}\alpha\beta}\sum_{\boldsymbol{k}}I_{0\alpha\boldsymbol{j}\beta}\Delta^{*}_{0\alpha\boldsymbol{j}\beta}e^{i\boldsymbol{k}\cdot\boldsymbol{r}^{\Delta}_{0\alpha\boldsymbol{j}\beta}}\left(\hat{c}_{-\boldsymbol{k}\alpha\uparrow}\hat{c}_{\boldsymbol{k}\beta\downarrow}-\hat{c}_{-\boldsymbol{k}\alpha\downarrow}\hat{c}_{\boldsymbol{k}\beta\uparrow}\right)\\
=&-\frac{1}{2}\sum_{\boldsymbol{j}\alpha\beta}\sum_{\boldsymbol{k}}\left(I_{0\beta\boldsymbol{j}\alpha}\Delta^{*}_{0\beta\boldsymbol{j}\alpha}e^{-i\boldsymbol{k}\cdot\boldsymbol{r}^{\Delta}_{0\beta\boldsymbol{j}\alpha}}+I_{0\alpha\boldsymbol{j}\beta}\Delta^{*}_{0\alpha\boldsymbol{j}\beta}e^{i\boldsymbol{k}\cdot\boldsymbol{r}^{\Delta}_{0\alpha\boldsymbol{j}\beta}}\right)\hat{c}_{-\boldsymbol{k}\alpha\downarrow}\hat{c}_{\boldsymbol{k}\beta\uparrow}.
\end{aligned} \tag{2.17}$$

Above, we have again used fermionic anti-commutation relations, re-indexed $\boldsymbol{k}\to-\boldsymbol{k}$, and swapped α and β on the first part of the sum. Comparing this with the third row on the right-hand side of Eq. (2.14), we set

$$\begin{aligned}
[\Delta_{\boldsymbol{k}}]^{*}_{\beta,\alpha}&=-\frac{1}{2}\sum_{\boldsymbol{j}}\left(I_{0\beta\boldsymbol{j}\alpha}\Delta^{*}_{0\beta\boldsymbol{j}\alpha}e^{-i\boldsymbol{k}\cdot\boldsymbol{r}^{\Delta}_{0\beta\boldsymbol{j}\alpha}}+I_{0\alpha\boldsymbol{j}\beta}\Delta^{*}_{0\alpha\boldsymbol{j}\beta}e^{i\boldsymbol{k}\cdot\boldsymbol{r}^{\Delta}_{0\alpha\boldsymbol{j}\beta}}\right)\\
&=-\frac{1}{2}\sum_{\boldsymbol{j}}\left(I_{0\beta\boldsymbol{j}\alpha}\Delta^{*}_{0\beta\boldsymbol{j}\alpha}e^{-i\boldsymbol{k}\cdot\boldsymbol{r}^{\Delta}_{0\beta\boldsymbol{j}\alpha}}+I_{\boldsymbol{j}\beta0\alpha}\Delta^{*}_{\boldsymbol{j}\beta0\alpha}e^{-i\boldsymbol{k}\cdot\boldsymbol{r}^{\Delta}_{\boldsymbol{j}\beta0\alpha}}\right)\\
&=-\frac{1}{2}\sum_{\boldsymbol{j}}\left(I_{0\beta\boldsymbol{j}\alpha}\Delta^{*}_{0\beta\boldsymbol{j}\alpha}e^{-i\boldsymbol{k}\cdot\boldsymbol{r}^{\Delta}_{0\beta\boldsymbol{j}\alpha}}+I_{-\boldsymbol{j}\beta0\alpha}\Delta^{*}_{-\boldsymbol{j}\beta0\alpha}e^{-i\boldsymbol{k}\cdot\boldsymbol{r}^{\Delta}_{-\boldsymbol{j}\beta0\alpha}}\right)\\
&=-\frac{1}{2}\sum_{\boldsymbol{j}}\left(I_{0\beta\boldsymbol{j}\alpha}\Delta^{*}_{0\beta\boldsymbol{j}\alpha}e^{-i\boldsymbol{k}\cdot\boldsymbol{r}^{\Delta}_{0\beta\boldsymbol{j}\alpha}}+I_{0\beta\boldsymbol{j}\alpha}\Delta^{*}_{0\beta\boldsymbol{j}\alpha}e^{-i\boldsymbol{k}\cdot\boldsymbol{r}^{\Delta}_{0\beta\boldsymbol{j}\alpha}}\right)\\
&=-\sum_{\boldsymbol{j}}I_{0\beta\boldsymbol{j}\alpha}\Delta^{*}_{0\beta\boldsymbol{j}\alpha}e^{-i\boldsymbol{k}\cdot\boldsymbol{r}^{\Delta}_{0\beta\boldsymbol{j}\alpha}}\\
\Leftrightarrow\ [\Delta_{\boldsymbol{k}}]_{\alpha,\beta}&=-\sum_{\boldsymbol{j}}I_{0\alpha\boldsymbol{j}\beta}\Delta_{0\alpha\boldsymbol{j}\beta}e^{i\boldsymbol{k}\cdot\boldsymbol{r}^{\Delta}_{0\alpha\boldsymbol{j}\beta}}.
\end{aligned} \tag{2.18, 2.19}$$

The steps here involve using $I_{i\alpha j\beta} = I_{j\beta i\alpha}$, $\Delta_{i\alpha j\beta} = \Delta_{j\beta i\alpha}$, $\boldsymbol{r}^{\Delta}_{i\alpha j\beta} = -\boldsymbol{r}^{\Delta}_{j\beta i\alpha}$, re-indexing $\boldsymbol{j} \to -\boldsymbol{j}$, and invoking translational invariance with $I_{-\boldsymbol{j}\beta 0\alpha} = I_{0\beta \boldsymbol{j}\alpha}$, $\Delta^{*}_{-\boldsymbol{j}\beta 0\alpha} = \Delta^{*}_{0\beta \boldsymbol{j}\alpha}$ and $\boldsymbol{r}^{\Delta}_{-\boldsymbol{j}\beta 0\alpha} = \boldsymbol{r}^{\Delta}_{0\beta \boldsymbol{j}\alpha}$. With this, we have

$$\hat{H}_{\mathrm{RVB}} = \sum_{\boldsymbol{k}\alpha\beta} \left([\Delta_{\boldsymbol{k}}]^{*}_{\beta\alpha} \hat{c}_{-\boldsymbol{k}\alpha\downarrow} \hat{c}_{\boldsymbol{k}\beta\uparrow} + \mathrm{H.c.} \right) + \frac{N_c}{J} \sum_{\boldsymbol{j}\alpha\beta} I_{0\alpha\boldsymbol{j}\beta} |\Delta_{0\alpha\boldsymbol{j}\beta}|^2, \tag{2.20}$$

which finally gives the whole Hamiltonian in BdG-form:

$$\hat{H} = \sum_{\boldsymbol{k}} \hat{\boldsymbol{c}}^{\dagger}_{\boldsymbol{k}} H_{\mathrm{BdG}}(\boldsymbol{k}) \hat{\boldsymbol{c}}_{\boldsymbol{k}} + \frac{N_c}{J} \sum_{\boldsymbol{j}\alpha\beta} I_{0\alpha\boldsymbol{j}\beta} |\Delta_{0\alpha\boldsymbol{j}\beta}|^2 + \sum_{\boldsymbol{k}} \mathrm{Tr}\, H^{\downarrow}_{-\boldsymbol{k}} - n_{\mathrm{orb}} N_c \mu, \tag{2.21}$$

$$\hat{\boldsymbol{c}}_{\boldsymbol{k}} = (\hat{c}_{\boldsymbol{k}\alpha=1\uparrow}, \ldots, \hat{c}_{\boldsymbol{k}\alpha=n_{\mathrm{orb}}\uparrow}, \hat{c}^{\dagger}_{-\boldsymbol{k}\alpha=1\downarrow}, \ldots, \hat{c}^{\dagger}_{-\boldsymbol{k}\alpha=n_{\mathrm{orb}}\downarrow}), \tag{2.22}$$

$$H_{\mathrm{BdG}}(\boldsymbol{k}) = \begin{pmatrix} H^{\uparrow}_{\boldsymbol{k}} - \mu \mathbf{1} & \Delta_{\boldsymbol{k}} \\ \Delta^{\dagger}_{\boldsymbol{k}} & -(H^{\downarrow}_{-\boldsymbol{k}})^{*} + \mu \mathbf{1} \end{pmatrix}, \tag{2.23}$$

$$[H^{\sigma}_{\boldsymbol{k}}]_{\alpha,\beta} = \sum_{\boldsymbol{j}} t^{\sigma}_{0\alpha\boldsymbol{j}\beta} e^{i\boldsymbol{k}\cdot\boldsymbol{r}^{\Delta}_{0\alpha\boldsymbol{j}\beta}}, \tag{2.24}$$

$$[\Delta_{\boldsymbol{k}}]_{\alpha,\beta} = -\sum_{\boldsymbol{j}} I_{0\alpha\boldsymbol{j}\beta} \Delta_{0\alpha\boldsymbol{j}\beta} e^{i\boldsymbol{k}\cdot\boldsymbol{r}^{\Delta}_{0\alpha\boldsymbol{j}\beta}}. \tag{2.25}$$

With on-site interactions, the only changes to the above are that the second term on the right-hand side of Eq. (2.21) becomes $\frac{N_c}{J} \sum_{\alpha} |\Delta_{\alpha}|^2$, and $\Delta_{\boldsymbol{k}} = \mathrm{diag}(\{\Delta_{\alpha}\})$ becomes a simple diagonal matrix, independent of $\boldsymbol{k}$.

2.2.1 Band Basis

The BdG-Hamiltonian is written in a basis described by the spinors $\hat{\boldsymbol{c}}_{\boldsymbol{k}}$. This basis is the orbital basis, as the operators $\hat{c}_{\boldsymbol{k}\alpha\sigma}$ (and their conjugates) act on a specific orbital. Another useful basis is the band basis, which is obtained by diagonalizing $H^{\sigma}_{\boldsymbol{k}}$, the kinetic portion of the Hamiltonian. Specifically, we write $H^{\sigma}_{\boldsymbol{k}} = \mathcal{G}_{\boldsymbol{k}\sigma} \boldsymbol{\varepsilon}_{\boldsymbol{k}\sigma} \mathcal{G}^{\dagger}_{\boldsymbol{k}\sigma}$, where $\boldsymbol{\varepsilon}_{\boldsymbol{k}\sigma}$ is a diagonal matrix containing the single-particle energies, and the columns of $\mathcal{G}_{\boldsymbol{k}\sigma}$ are the Bloch states. We can then define a new set of operators $\hat{\boldsymbol{d}}_{\boldsymbol{k}}$ to transform the BdG-Hamiltonian with

$$\sum_{\boldsymbol{k}} \hat{\boldsymbol{c}}^{\dagger}_{\boldsymbol{k}} H_{\mathrm{BdG}}(\boldsymbol{k}) \hat{\boldsymbol{c}}_{\boldsymbol{k}} = \sum_{\boldsymbol{k}} \hat{\boldsymbol{d}}^{\dagger}_{\boldsymbol{k}} \tilde{H}_{\mathrm{BdG}}(\boldsymbol{k}) \hat{\boldsymbol{d}}_{\boldsymbol{k}}, \tag{2.26}$$

$$\tilde{H}_{\mathrm{BdG}}(\boldsymbol{k}) = \begin{pmatrix} \boldsymbol{\varepsilon}_{\boldsymbol{k}\uparrow} - \mu \mathbf{1} & \Delta^{\mathrm{band}}_{\boldsymbol{k}} \\ (\Delta^{\mathrm{band}}_{\boldsymbol{k}})^{\dagger} & -\boldsymbol{\varepsilon}_{-\boldsymbol{k}\downarrow} + \mu \mathbf{1} \end{pmatrix}, \tag{2.27}$$

$$\hat{\boldsymbol{d}}_{\boldsymbol{k}} = \begin{pmatrix} \mathcal{G}^{\dagger}_{\boldsymbol{k}\uparrow} & 0 \\ 0 & \mathcal{G}^{T}_{-\boldsymbol{k}\downarrow} \end{pmatrix} \hat{\boldsymbol{c}}_{\boldsymbol{k}}, \tag{2.28}$$

$$\Delta^{\mathrm{band}}_{\boldsymbol{k}} = \mathcal{G}^{\dagger}_{\boldsymbol{k}\uparrow} \Delta_{\boldsymbol{k}} \mathcal{G}^{*}_{-\boldsymbol{k}\downarrow}. \tag{2.29}$$

As the kinetic block is now diagonal, the operators in $\hat{\boldsymbol{d}}_{\boldsymbol{k}}$ act on the single-particle energy bands of the system. Correspondingly, the transformed order parameter matrix $\Delta_{\boldsymbol{k}}^{\text{band}}$ contains the pairing contributions of particles in specific bands. The diagonal components give the intra-band pairings, describing two particles on a same band forming a pair, while the off-diagonal components give the various inter-band pairings.

We note that in systems with TRS, we can use $(H_{-\boldsymbol{k}}^{\downarrow})^* = H_{\boldsymbol{k}}^{\uparrow}$ to simplify the above equations with $\boldsymbol{\varepsilon}_{-\boldsymbol{k}\downarrow} = \boldsymbol{\varepsilon}_{\boldsymbol{k}\uparrow}$ and $\mathcal{G}_{-\boldsymbol{k}\downarrow}^* = \mathcal{G}_{\boldsymbol{k}\uparrow}$.

2.2.2 Many-body Energies and Eigenstates

With the Hamiltonian written in BdG-form in Eq. (2.21), diagonalizing it becomes (formally) simple. We write the diagonalization of the matrix part (Eq. (2.23)) as $H_{\text{BdG}} = \mathcal{W}_{\boldsymbol{k}} E_{\boldsymbol{k}} \mathcal{W}_{\boldsymbol{k}}^{\dagger}$ and introduce yet another set of quasi-particle operators $\hat{\boldsymbol{\gamma}}_{\boldsymbol{k}} = \mathcal{W}_{\boldsymbol{k}}^{\dagger} \hat{\boldsymbol{c}}_{\boldsymbol{k}}$ to get

$$\sum_{\boldsymbol{k}} \hat{\boldsymbol{c}}_{\boldsymbol{k}}^{\dagger} H_{\text{BdG}}(\boldsymbol{k}) \hat{\boldsymbol{c}}_{\boldsymbol{k}} = \sum_{\boldsymbol{k}} \hat{\boldsymbol{\gamma}}_{\boldsymbol{k}}^{\dagger} E_{\boldsymbol{k}} \hat{\boldsymbol{\gamma}}_{\boldsymbol{k}}, \tag{2.30}$$

$$E_{\boldsymbol{k}} = \begin{pmatrix} \text{diag}(E_{\boldsymbol{k}1}^{+}, \ldots, E_{\boldsymbol{k}n_{\text{orb}}}^{+}) & 0 \\ 0 & \text{diag}(E_{\boldsymbol{k}1}^{-}, \ldots, E_{\boldsymbol{k}n_{\text{orb}}}^{-}) \end{pmatrix}, \tag{2.31}$$

where the $E_{\boldsymbol{k}m}^{\pm}$ are the energies of the quasi-particles, while $\mathcal{W}_{\boldsymbol{k}}$ contains the eigenstates.

As the $\hat{\boldsymbol{\gamma}}_{\boldsymbol{k}}$ are obtained with a unitary transformation from the $\hat{\boldsymbol{c}}_{\boldsymbol{k}}$, they obey the fermionic anti-commutation relations. The basis defined by the $\hat{\boldsymbol{\gamma}}_{\boldsymbol{k}}$ is useful because, as the Hamiltonian is diagonal in this basis, the quasi-particles described by $\hat{\boldsymbol{\gamma}}_{\boldsymbol{k}}$ are non-interacting. Thus, they follow Fermi-Dirac statistics, which we take advantage of in the following while deriving the gap equation.

2.3 The Gap Equation and Particle Number Densities

The order parameters $\Delta_{i\alpha j\beta}$ need to be solved self-consistently. Here, we derive the gap equation that the order parameters need to satisfy, and give expressions for the particle number densities in the system. To obtain the gap equation, the idea is to transform the definition of $\Delta_{i\alpha j\beta}$ into the quasi-particle basis described by $\hat{\boldsymbol{\gamma}}_{\boldsymbol{k}}$. In this basis, we can then evaluate the relevant expectation values using Fermi-Dirac statistics, given that the quasi-particles are non-interacting. As an intermediate step, consider first the expectation values $\langle \hat{c}_{\boldsymbol{k}\alpha\uparrow} \hat{c}_{\boldsymbol{k}'\beta\downarrow} \rangle$ and $\langle \hat{c}_{\boldsymbol{k}\alpha\downarrow} \hat{c}_{\boldsymbol{k}'\beta\uparrow} \rangle$. Using the definitions of $\hat{\boldsymbol{\gamma}}_{\boldsymbol{k}}$ and $\hat{\boldsymbol{c}}_{\boldsymbol{k}}$, the first one evaluates to

$$
\begin{aligned}
\langle \hat{c}_{\boldsymbol{k}\alpha\uparrow}\hat{c}_{\boldsymbol{k}'\beta\downarrow}\rangle &= \langle [\mathcal{W}_{\boldsymbol{k}}\hat{\boldsymbol{\gamma}}_{\boldsymbol{k}}]_{\alpha}[\hat{\boldsymbol{\gamma}}^{\dagger}_{-\boldsymbol{k}'}\mathcal{W}^{\dagger}_{-\boldsymbol{k}'}]_{\beta+n_{\mathrm{orb}}}\rangle \\
&= \sum_{ll'}\langle [\mathcal{W}_{\boldsymbol{k}}]_{\alpha,l}[\hat{\boldsymbol{\gamma}}_{\boldsymbol{k}}]_{l}[\hat{\boldsymbol{\gamma}}^{\dagger}_{-\boldsymbol{k}'}]_{l'}[\mathcal{W}^{\dagger}_{-\boldsymbol{k}'}]_{l',\beta+n_{\mathrm{orb}}}\rangle \\
&= \sum_{ll'}[\mathcal{W}_{\boldsymbol{k}}]_{\alpha,l}[\mathcal{W}^{\dagger}_{-\boldsymbol{k}'}]_{l',\beta+n_{\mathrm{orb}}}\langle [\hat{\boldsymbol{\gamma}}_{\boldsymbol{k}}]_{l}[\hat{\boldsymbol{\gamma}}^{\dagger}_{-\boldsymbol{k}'}]_{l'}\rangle \\
&= \delta_{\boldsymbol{k},-\boldsymbol{k}'}\left[\mathcal{W}_{\boldsymbol{k}}(\mathbf{1}_{2n_{\mathrm{orb}}\times 2n_{\mathrm{orb}}} - n_F(E_{\boldsymbol{k}}))\mathcal{W}^{\dagger}_{\boldsymbol{k}}\right]_{\alpha,\beta+n_{\mathrm{orb}}} \\
&= -\delta_{\boldsymbol{k},-\boldsymbol{k}'}\left[\mathcal{W}_{\boldsymbol{k}}n_F(E_{\boldsymbol{k}})\mathcal{W}^{\dagger}_{\boldsymbol{k}}\right]_{\alpha,\beta+n_{\mathrm{orb}}}
\end{aligned}
\tag{2.32}
$$

where $n_F(\epsilon) = (e^{\beta\epsilon}+1)^{-1}$ is the Fermi-Dirac distribution with β the inverse temperature, and $\mathbf{1}_{2n_{\mathrm{orb}}\times 2n_{\mathrm{orb}}}$ is the $2n_{\mathrm{orb}} \times 2n_{\mathrm{orb}}$ identity matrix. Here, we have expanded the matrix-vector multiplications into summations, and used the fact that $\langle [\hat{\boldsymbol{\gamma}}_{\boldsymbol{k}}]_l [\hat{\boldsymbol{\gamma}}^{\dagger}_{-\boldsymbol{k}'}]_{l'}\rangle$ is zero unless both $\boldsymbol{k} = -\boldsymbol{k}'$ and $l = l'$, in which case it equals one minus n_F evaluated at the corresponding energy (due to anti-commutation of the operators). The last row results from $\mathcal{W}_{\boldsymbol{k}}$ being a unitary matrix, and the fact that α and $\beta + n_{\mathrm{orb}}$ are never equal. For the latter expectation value, a similar calculation gives

$$
\begin{aligned}
\langle \hat{c}_{\boldsymbol{k}\alpha\downarrow}\hat{c}_{\boldsymbol{k}'\beta\uparrow}\rangle &= \langle [\hat{\boldsymbol{\gamma}}^{\dagger}_{-\boldsymbol{k}}\mathcal{W}^{\dagger}_{-\boldsymbol{k}}]_{\alpha+n_{\mathrm{orb}}}[\mathcal{W}_{\boldsymbol{k}'}\hat{\boldsymbol{\gamma}}_{\boldsymbol{k}'}]_{\beta}\rangle \\
&= \sum_{ll'}\langle [\hat{\boldsymbol{\gamma}}^{\dagger}_{-\boldsymbol{k}}]_{l}[\mathcal{W}^{\dagger}_{-\boldsymbol{k}}]_{l,\alpha+n_{\mathrm{orb}}}[\mathcal{W}_{\boldsymbol{k}'}]_{\beta,l'}[\hat{\boldsymbol{\gamma}}_{\boldsymbol{k}'}]_{l'}\rangle \\
&= \sum_{ll'}[\mathcal{W}^{\dagger}_{-\boldsymbol{k}}]_{l,\alpha+n_{\mathrm{orb}}}[\mathcal{W}_{\boldsymbol{k}'}]_{\beta,l'}\langle [\hat{\boldsymbol{\gamma}}^{\dagger}_{-\boldsymbol{k}}]_{l}[\hat{\boldsymbol{\gamma}}_{\boldsymbol{k}'}]_{l'}\rangle \\
&= \delta_{\boldsymbol{k},-\boldsymbol{k}'}\left[\mathcal{W}_{-\boldsymbol{k}}n_F(E_{-\boldsymbol{k}})\mathcal{W}^{\dagger}_{-\boldsymbol{k}}\right]_{\beta,\alpha+n_{\mathrm{orb}}}.
\end{aligned}
\tag{2.33}
$$

With these results, we get the gap equation

$$
\begin{aligned}
\Delta_{\boldsymbol{i}\alpha\boldsymbol{j}\beta} &= -\frac{J}{2}\langle \hat{h}_{\boldsymbol{i}\alpha\boldsymbol{j}\beta}\rangle \\
&= -\frac{J}{2}\langle \hat{c}_{\boldsymbol{i}\alpha\uparrow}\hat{c}_{\boldsymbol{j}\beta\downarrow} - \hat{c}_{\boldsymbol{i}\alpha\downarrow}\hat{c}_{\boldsymbol{j}\beta\uparrow}\rangle \\
&= -\frac{J}{2N_c}\sum_{\boldsymbol{k}\boldsymbol{k}'} e^{i[\boldsymbol{k}\cdot(\boldsymbol{R_i}+\boldsymbol{\delta}_\alpha)+\boldsymbol{k}'\cdot(\boldsymbol{R_j}+\boldsymbol{\delta}_\beta)]}\langle \hat{c}_{\boldsymbol{k}\alpha\uparrow}\hat{c}_{\boldsymbol{k}'\beta\downarrow} - \hat{c}_{\boldsymbol{k}\alpha\downarrow}\hat{c}_{\boldsymbol{k}'\beta\uparrow}\rangle \\
&= -\frac{J}{2N_c}\sum_{\boldsymbol{k}} e^{i\boldsymbol{k}\cdot\boldsymbol{r}^{\Delta}_{\boldsymbol{j}\beta\boldsymbol{i}\alpha}}\left(-\left[\mathcal{W}_{\boldsymbol{k}}n_F(E_{\boldsymbol{k}})\mathcal{W}^{\dagger}_{\boldsymbol{k}}\right]_{\alpha,\beta+n_{\mathrm{orb}}} - \left[\mathcal{W}_{-\boldsymbol{k}}n_F(E_{-\boldsymbol{k}})\mathcal{W}^{\dagger}_{-\boldsymbol{k}}\right]_{\beta,\alpha+n_{\mathrm{orb}}}\right) \\
&= \frac{J}{2N_c}\sum_{\boldsymbol{k}}\left(e^{-i\boldsymbol{k}\cdot\boldsymbol{r}^{\Delta}_{\boldsymbol{i}\alpha\boldsymbol{j}\beta}}\left[\mathcal{W}_{\boldsymbol{k}}n_F(E_{\boldsymbol{k}})\mathcal{W}^{\dagger}_{\boldsymbol{k}}\right]_{\alpha,\beta+n_{\mathrm{orb}}} + e^{i\boldsymbol{k}\cdot\boldsymbol{r}^{\Delta}_{\boldsymbol{i}\alpha\boldsymbol{j}\beta}}\left[\mathcal{W}_{\boldsymbol{k}}n_F(E_{\boldsymbol{k}})\mathcal{W}^{\dagger}_{\boldsymbol{k}}\right]_{\beta,\alpha+n_{\mathrm{orb}}}\right).
\end{aligned}
\tag{2.34}
$$

The relation $\boldsymbol{r}^{\Delta}_{\boldsymbol{i}\alpha\boldsymbol{j}\beta} = -\boldsymbol{r}^{\Delta}_{\boldsymbol{j}\beta\boldsymbol{i}\alpha}$ was used here, along with an index shift $\boldsymbol{k} \to -\boldsymbol{k}$ on the latter part of the summation. It should also be noted that due to the translational

invariance assumption, the order parameters are equal across unit cells. We can thus disregard the index $\boldsymbol{i}$ as it is enough to consider $\Delta_{0\alpha\boldsymbol{j}\beta}$.

This is a self-consistency equation for the order parameters; the right-hand side of the equation depends on the energies $E_{\boldsymbol{k}}$ and the many-body states $\mathcal{W}_{\boldsymbol{k}}$, which in turn depend on the $\Delta_{\boldsymbol{i}\alpha\boldsymbol{j}\beta}$ via the BdG-Hamiltonian. The ground-state order parameters should be solved such that this relation is satisfied.

The particle number densities $n_{\boldsymbol{i}\alpha\sigma} = \langle \hat{c}^\dagger_{\boldsymbol{i}\alpha\sigma} \hat{c}_{\boldsymbol{i}\alpha\sigma} \rangle$ for each of the lattice sites can be obtained similarly. Here, we just give the resulting expressions, which come out to be

$$n_{\boldsymbol{i}\alpha\uparrow} = \frac{1}{N_c} \sum_{\boldsymbol{k}} \left[\mathcal{W}_{\boldsymbol{k}} n_F(E_{\boldsymbol{k}}) \mathcal{W}_{\boldsymbol{k}}^\dagger \right]_{\alpha,\alpha} \tag{2.35}$$

$$n_{\boldsymbol{i}\alpha\downarrow} = \frac{1}{N_c} \sum_{\boldsymbol{k}} \left[\mathcal{W}_{\boldsymbol{k}} (\mathbf{1}_{2n\times 2n} - n_F(E_{\boldsymbol{k}})) \mathcal{W}_{\boldsymbol{k}}^\dagger \right]_{\alpha+n_{\mathrm{orb}},\alpha+n_{\mathrm{orb}}}. \tag{2.36}$$

Again, due to translational invariance, the index $\boldsymbol{i}$ can be dropped and we can simply consider $n_{\alpha\sigma}$, since the densities are equal across unit cells.

With on-site interactions, a similar derivation to the above yields the gap equation

$$\Delta_\alpha = -\frac{J}{N_c} \sum_{\boldsymbol{k}} \left[\mathcal{W}_{\boldsymbol{k}} n_F(E_{\boldsymbol{k}}) \mathcal{W}_{\boldsymbol{k}}^\dagger \right]_{\alpha,\alpha+n_{\mathrm{orb}}}, \tag{2.37}$$

while the expressions for the particle number densities remain the same.

2.4 The Grand Potential

Equivalently to satisfying the gap equation, the order parameters need to locally minimize the grand potential Ω of the system, with the global minimum determining the ground state in case of multiple local minima. Here, we will derive an expression for Ω in terms of the order parameters and the BdG-energies $E^{\pm}_{\boldsymbol{k}m}$. The grand potential is defined as $\Omega = -\frac{1}{\beta} \ln \mathcal{Z}_\Omega$ via the grand partition function $\mathcal{Z}_\Omega = \mathrm{Tr}\, e^{-\beta \hat{H}}$, where β is the inverse temperature. Inserting the BdG-form of the Hamiltonian from Eq. (2.21) gives

$$
\begin{aligned}
\Omega &= -\frac{1}{\beta}\ln \mathrm{Tr}\, e^{-\beta \hat{H}} \\
&= -\frac{1}{\beta}\ln \mathrm{Tr}\left[\exp\left(-\beta\Big\{\sum_{\boldsymbol{k}} \hat{\boldsymbol{c}}_{\boldsymbol{k}}^{\dagger} H_{\mathrm{BdG}}(\boldsymbol{k})\hat{\boldsymbol{c}}_{\boldsymbol{k}} \right.\right. \\
&\qquad\qquad \left.\left. + \frac{N_c}{J}\sum_{j\alpha\beta} I_{0\alpha j\beta}|\Delta_{0\alpha j\beta}|^2 + \sum_{\boldsymbol{k}} \mathrm{Tr}\, H^{\downarrow}_{-\boldsymbol{k}} - n_{\mathrm{orb}} N_c \mu\Big\}\right)\right] \\
&= -\frac{1}{\beta}\ln \mathrm{Tr}\left[\exp\left(-\beta\sum_{\boldsymbol{k}} \hat{\boldsymbol{c}}_{\boldsymbol{k}}^{\dagger} H_{\mathrm{BdG}}(\boldsymbol{k})\hat{\boldsymbol{c}}_{\boldsymbol{k}}\right)\right. \\
&\qquad\qquad \left.\times \exp\left(-\beta\Big\{\frac{N_c}{J}\sum_{j\alpha\beta} I_{0\alpha j\beta}|\Delta_{0\alpha j\beta}|^2 + \sum_{\boldsymbol{k}} \mathrm{Tr}\, H^{\downarrow}_{-\boldsymbol{k}} - n_{\mathrm{orb}} N_c \mu\Big\}\right)\right] \\
&= -\frac{1}{\beta}\ln \mathrm{Tr}\left[\exp\left(-\beta\sum_{\boldsymbol{k}} \hat{\boldsymbol{c}}_{\boldsymbol{k}}^{\dagger} H_{\mathrm{BdG}}(\boldsymbol{k})\hat{\boldsymbol{c}}_{\boldsymbol{k}}\right)\right] \\
&\quad + \frac{N_c}{J}\sum_{j\alpha\beta} I_{0\alpha j\beta}|\Delta_{0\alpha j\beta}|^2 + \sum_{\boldsymbol{k}} \mathrm{Tr}\, H^{\downarrow}_{-\boldsymbol{k}} - n_{\mathrm{orb}} N_c \mu.
\end{aligned}
\tag{2.38}
$$

To obtain the last two equalities, notice that the last three terms of the Hamiltonian are just scalars. Thus, they commute with the first term, and the single exponential can be broken up into a product of two exponentials. Subsequently, the scalar terms can be pulled out of the trace, and the logarithm cancels the exponential, while also turning the multiplication into addition again. To evaluate the remaining trace, we resort to the diagonalization of $H_{\mathrm{BdG}}(\boldsymbol{k})$, i.e. Eq. (2.30) to get

$$
\begin{aligned}
&\mathrm{Tr}\left[\exp\left(-\beta\sum_{\boldsymbol{k}} \hat{\boldsymbol{c}}_{\boldsymbol{k}}^{\dagger} H_{\mathrm{BdG}}(\boldsymbol{k})\hat{\boldsymbol{c}}_{\boldsymbol{k}}\right)\right] \\
&= \mathrm{Tr}\left[\exp\left(-\beta\sum_{\boldsymbol{k}} \hat{\boldsymbol{\gamma}}_{\boldsymbol{k}}^{\dagger} E_{\boldsymbol{k}} \hat{\boldsymbol{\gamma}}_{\boldsymbol{k}}\right)\right] \\
&= \mathrm{Tr}\left[\exp\left(-\beta\sum_{\boldsymbol{k}m} \left([\hat{\boldsymbol{\gamma}}_{\boldsymbol{k}}^{\dagger}]_m E^{+}_{\boldsymbol{k}m}[\hat{\boldsymbol{\gamma}}_{\boldsymbol{k}}]_m + [\hat{\boldsymbol{\gamma}}_{\boldsymbol{k}}^{\dagger}]_{m+n_{\mathrm{orb}}} E^{-}_{\boldsymbol{k}m}[\hat{\boldsymbol{\gamma}}_{\boldsymbol{k}}]_{m+n_{\mathrm{orb}}}\right)\right)\right] \\
&= \mathrm{Tr}\left[\prod_{\boldsymbol{k}m} \exp\left(-\beta[\hat{\boldsymbol{\gamma}}_{\boldsymbol{k}}^{\dagger}]_m E^{+}_{\boldsymbol{k}m}[\hat{\boldsymbol{\gamma}}_{\boldsymbol{k}}]_m\right)\exp\left(-\beta[\hat{\boldsymbol{\gamma}}_{\boldsymbol{k}}^{\dagger}]_{m+n_{\mathrm{orb}}} E^{-}_{\boldsymbol{k}m}[\hat{\boldsymbol{\gamma}}_{\boldsymbol{k}}]_{m+n_{\mathrm{orb}}}\right)\right] \\
&= \prod_{\boldsymbol{k}m} \mathrm{Tr}\left[\exp\left(-\beta E^{+}_{\boldsymbol{k}m}[\hat{\boldsymbol{\gamma}}_{\boldsymbol{k}}^{\dagger}]_m[\hat{\boldsymbol{\gamma}}_{\boldsymbol{k}}]_m\right)\right]\mathrm{Tr}\left[\exp\left(-\beta E^{-}_{\boldsymbol{k}m}[\hat{\boldsymbol{\gamma}}_{\boldsymbol{k}}^{\dagger}]_{m+n_{\mathrm{orb}}}[\hat{\boldsymbol{\gamma}}_{\boldsymbol{k}}]_{m+n_{\mathrm{orb}}}\right)\right] \\
&= \prod_{\boldsymbol{k}m}\left(1+e^{-\beta E^{+}_{\boldsymbol{k}m}}\right)\left(1+e^{-\beta E^{-}_{\boldsymbol{k}m}}\right).
\end{aligned}
\tag{2.39}
$$

To obtain this result, notice that the fermionic number operators $[\hat{\boldsymbol{\gamma}}_{\boldsymbol{k}}^\dagger]_m[\hat{\boldsymbol{\gamma}}_{\boldsymbol{k}}]_m$ and $[\hat{\boldsymbol{\gamma}}_{\boldsymbol{k}}^\dagger]_{m+n_{\text{orb}}}[\hat{\boldsymbol{\gamma}}_{\boldsymbol{k}}]_{m+n_{\text{orb}}}$ all commute with each other, which allows us to break the single exponential into a product of exponentials. We then have a trace of a tensor product, which is equal to the product of the individual traces. Finally, the trace of the exponential of a fermionic number operator is

$$\begin{aligned}
&\operatorname{Tr}\left[\exp\left(-\beta E^+_{\boldsymbol{k}m}[\hat{\boldsymbol{\gamma}}_{\boldsymbol{k}}^\dagger]_m[\hat{\boldsymbol{\gamma}}_{\boldsymbol{k}}]_m\right)\right] \\
&= \langle 0|e^{-\beta E^+_{\boldsymbol{k}m}[\hat{\boldsymbol{\gamma}}_{\boldsymbol{k}}^\dagger]_m[\hat{\boldsymbol{\gamma}}_{\boldsymbol{k}}]_m}|0\rangle + \langle 1|e^{-\beta E^+_{\boldsymbol{k}m}[\hat{\boldsymbol{\gamma}}_{\boldsymbol{k}}^\dagger]_m[\hat{\boldsymbol{\gamma}}_{\boldsymbol{k}}]_m}|1\rangle \\
&= \sum_{i=0}^{\infty}\frac{(-\beta E^+_{\boldsymbol{k}m})^i}{i!}\langle 0|([\hat{\boldsymbol{\gamma}}_{\boldsymbol{k}}^\dagger]_m[\hat{\boldsymbol{\gamma}}_{\boldsymbol{k}}]_m)^i|0\rangle + \sum_{i=0}^{\infty}\frac{(-\beta E^-_{\boldsymbol{k}m})^i}{i!}\langle 1|([\hat{\boldsymbol{\gamma}}_{\boldsymbol{k}}^\dagger]_m[\hat{\boldsymbol{\gamma}}_{\boldsymbol{k}}]_m)^i|1\rangle \\
&= 1 + \sum_{i=0}^{\infty}\frac{(-\beta E^-_{\boldsymbol{k}m})^i}{i!}1^i \\
&= 1 + e^{-\beta E^+_{\boldsymbol{k}m}}.
\end{aligned} \tag{2.40}$$

The steps for evaluating the latter number operator trace are the same. Inserting these results into the expression for the grand potential, we get

$$\begin{aligned}
\Omega = -\frac{1}{\beta}\sum_{\boldsymbol{k}m}\left(\ln\left(1+e^{-\beta E^+_{\boldsymbol{k}m}}\right)+\ln\left(1+e^{-\beta E^-_{\boldsymbol{k}m}}\right)\right) + \frac{N_c}{J}\sum_{\boldsymbol{j}\alpha\beta} I_{0\alpha\boldsymbol{j}\beta}|\Delta_{0\alpha\boldsymbol{j}\beta}|^2 \\
+ \sum_{\boldsymbol{k}}\operatorname{Tr} H^\downarrow_{-\boldsymbol{k}} - n_{\text{orb}}N_c\mu.
\end{aligned} \tag{2.41}$$

Some remarks on this result are in order. First, the last two terms on the right-hand side do not depend on the order parameters, so they can be ignored while minimizing the grand potential. The third term is always positive, so it serves as a regularizer to the order parameters, i.e. it makes the order parameters minimizing Ω finite. Thus, the interpretation is that for there to be pairing, the first two terms containing the energies $E^\pm_{\boldsymbol{k}m}$ need to become smaller than they are without pairing, and the decrease needs to be larger than the increase due to the regularizer. The interpretation becomes especially clear at zero temperature, when $\beta \to \infty$. To see what happens in this limit, let $f(x) = -\frac{1}{x}\ln(1+e^{-cx})$. Then, as $x \to \infty$,

$$f(x) \to \begin{cases} c & \text{if } c < 0 \\ 0 & \text{otherwise.} \end{cases} \tag{2.42}$$

Thus, the first summation becomes simply the sum of negative energies at zero temperature, and the ground state occurs when the decrease in energies due to pairing balances out the regularizing term.

We can get an alternative expression for the grand potential by transforming the regularizing term into momentum-space. Using the Fourier transform property $N_c \sum_{\boldsymbol{j}} I_{0\alpha\boldsymbol{j}\beta}|\Delta_{0\alpha\boldsymbol{j}\beta}|^2 = \sum_{\boldsymbol{k}} |[\Delta_{\boldsymbol{k}}]_{\alpha,\beta}|^2$ (which is also simple to verify), we can write Ω as a single momentum-space sum:

$$\Omega = \sum_{\boldsymbol{k}} \left(-\frac{1}{\beta} \sum_{m} \left\{ \ln\left(1 + e^{-\beta E^{+}_{\boldsymbol{k}m}}\right) + \ln\left(1 + e^{-\beta E^{-}_{\boldsymbol{k}m}}\right) \right\} + \frac{1}{J} \sum_{\alpha\beta} \left| [\Delta_{\boldsymbol{k}}]_{\alpha,\beta} \right|^2 \right) + \quad \text{const.} \tag{2.43}$$

At first glance, it would seem that to obtain the order parameters, we could minimize the expression in the sum independently for each $\boldsymbol{k}$. However, this is not the case, since the Fourier components $[\Delta_{\boldsymbol{k}}]_{\alpha,\beta}$ are not independent parameters; instead, they are determined by the real-space order parameters $\Delta_{0\alpha\boldsymbol{j}\beta}$. The fact that our model considers only nearest-neighbour interactions is equivalent to forcing $\Delta_{0\alpha\boldsymbol{j}\beta} = 0$ if sites 0α and $\boldsymbol{j}\beta$ are not neighbours, which imposes restrictions on the Fourier components. Physically, allowing the Fourier components to be independent for each $\boldsymbol{k}$ would allow interactions with an arbitrarily long range.

Finally, we note that for on-site interactions, the expression for the grand potential is otherwise identical to Eq. (2.41), but the regularizing term is replaced with $\frac{N_c}{J} \sum_{\alpha} |\Delta_{\alpha}|^2$. On the other hand, the form of Ω in Eq. (2.43) is exactly identical for both interaction types, as seen by using $\Delta_{\boldsymbol{k}} = \mathrm{diag}(\{\Delta_{\alpha}\})$ for on-site interactions.

3 Analytical Results

In this section, we move from existing background theory to new theoretical results.

3.1 Semi-bipartite Lattices with Nearest-neighbour Interactions

In the following, we will consider semi-bipartite lattices, and show some special results that are consequences of the structure of such lattices. We start by introducing the notions of bipartiteness and semi-bipartiteness, which are concepts from graph theory, but extend naturally also to lattices. After all, a lattice is really just a type of a graph, with the sites as its nodes, and the hoppings linking the sites as its edges. A bipartite graph is a type of graph where the nodes can be divided into two subgraphs such that there are no internal edges in either of them. In other words, all edges must be linking a node from one subgraph to a node from the other. Thus, for a bipartite lattice, a similar division must be possible for the orbitals. We give an example of a bipartite graph, a bipartite lattice, and a non-bipartite lattice in Fig. 1.

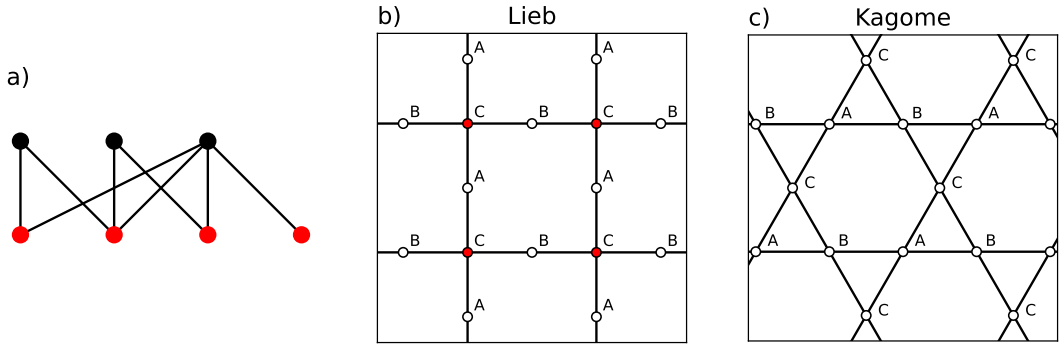

Figure 1: (**a**): A bipartite graph: there are no edges from a red node to a red node or from a black node to a black node; only from a red node to a black node. (**b**): The structure of the Lieb lattice, which is bipartite: orbital C (colored in red) forms one sublattice and orbitals A and B (colored in white) together another such that there are no internal edges in the sublattices. (**c**): The structure of the kagome lattice, which is not bipartite. Here, a similar division of the orbitals cannot be done.

Semi-bipartiteness is a relaxed version of this criterion: for semi-bipartite lattices, we allow internal edges in one of the sublattices. As such, every bipartite lattice is also a semi-bipartite lattice. As is, semi-bipartiteness is actually not a very restricting property: any lattice with at least one orbital that is not connected to itself (that is, a site being connected to a site at the same orbital in another unit cell) is semi-bipartite, since we can choose this single orbital to form the sublattice without internal edges, and group the rest of the orbitals to the other sublattice. However, in this section we are going to add two more restrictions: the sublattices have to be of unequal sizes, and internal edges are only allowed in the smaller sublattice, where the size of a sublattice is determined by the number of orbitals it contains. Note that every bipartite lattice automatically satisfies the latter of these restrictions, but not necessarily the former.

The Lieb lattice, shown in Fig. 1b, satisfies these conditions, as it is a bipartite lattice where the sublattice sizes are two and one.

In addition to this lattice structure, instead of the RVB interaction specifically, in this section we consider a generic nearest-neighbour interaction, since the results we will show hold for all such interactions, of which the RVB interaction is just an example. As it turns out, with this quite general setup, the following results hold:

- There will be one or more flat bands at zero energy in the single-particle spectrum of the system. This is a known result [47].
- If the chemical potential is set to zero, i.e. to the flat band, there will also be flat bands in the BdG-spectrum, i.e. flat quasi-particle energy bands. These flat bands will also be at zero energy. This is a result discovered in this thesis.
- Pairing in the single-particle flat band(s) is forbidden. That is, the intra-band component(s) of the order parameter matrix will always be zero for the flat band(s), and so will the inter-band components between flat bands in the case of multiple, degenerate single-particle flat bands. Pairing can, however, occur between flat and dispersive bands. This is also a result of this thesis.

Next, we will show these general properties, and afterwards consider the Lieb lattice as an example.

3.1.1 Flat Bands in the BdG-spectrum

The beginning part of this section will closely follow the discussion in Ref. [47]. Consider a lattice with n_{orb} orbitals. Divide it into two sublattices, L and $\tilde{L}$, with n_L and $n_{\tilde{L}}$ orbitals, respectively, so that $n_L + n_{\tilde{L}} = n_{\text{orb}}$. We will further assume that $n_L > n_{\tilde{L}}$, and that the lattice is semi-bipartite in such a way that there are no internal edges in the larger sublattice L. Then, the Fourier-transformed kinetic Hamiltonian $H^\sigma_{\boldsymbol{k}}$ of the lattice can be written in block form

$$H^\sigma_{\boldsymbol{k}} = \begin{array}{c} \begin{matrix} n_L & n_{\tilde{L}} \end{matrix} \\ \begin{pmatrix} 0 & S^\sigma_{\boldsymbol{k}} \\ (S^\sigma_{\boldsymbol{k}})^\dagger & B^\sigma_{\boldsymbol{k}} \end{pmatrix} \end{array} \begin{matrix} n_L \\ n_{\tilde{L}} \end{matrix} , \tag{3.1}$$

where $S^\sigma_{\boldsymbol{k}}$ is a rectangular matrix containing the inter-sublattice hoppings, $B^\sigma_{\boldsymbol{k}}$ is a square matrix containing the possible intra-sublattice hoppings of $\tilde{L}$, and the upper-left zero block reflects the fact that there are no hoppings in the larger sublattice. The dimensions of the blocks are indicated outside the matrix for clarity. Now, because of the zero block, the n_L left-most columns of this matrix can span at most $n_{\tilde{L}}$ dimensions. As a consequence, the rank of the matrix is at most $2n_{\tilde{L}}$, which implies that it has at least $n_{\text{orb}} - 2n_{\tilde{L}} = n_L - n_{\tilde{L}}$ zero eigenvalues. This holds for any $\boldsymbol{k}$, and there are thus at least $n_L - n_{\tilde{L}}$ flat bands at zero energy in the single-particle spectrum of this system.

These flat bands are the result of the mismatched dimensions $n_L > n_{\tilde{L}}$. This means that $S^\sigma_{\boldsymbol{k}}$ and its conjugate are rectangular matrices, which implies that they have non-trivial kernels. In particular, let $r_{\boldsymbol{k}} \leq n_{\tilde{L}}$ be the rank of $S^\sigma_{\boldsymbol{k}}$ (and $(S^\sigma_{\boldsymbol{k}})^\dagger$), and $\phi_{\boldsymbol{k}m}$, $1 \leq m \leq n_L - r_{\boldsymbol{k}}$ be a basis for the kernel of $(S^\sigma_{\boldsymbol{k}})^\dagger$. The eigenvectors $\Psi^{\text{flat}}_{\boldsymbol{k}m\sigma}$ of $H^\sigma_{\boldsymbol{k}}$, i.e. the Bloch states corresponding to the flat bands, are then of the form

$$\Psi^{\text{flat}}_{\boldsymbol{k}m\sigma} = \begin{pmatrix} \phi_{\boldsymbol{k}m} \\ 0 \end{pmatrix} \begin{matrix} n_L \\ n_{\tilde{L}} \end{matrix}, \tag{3.2}$$

as is easily seen via

$$H^\sigma_{\boldsymbol{k}} \Psi^{\text{flat}}_{\boldsymbol{k}m\sigma} = \begin{pmatrix} 0 & S^\sigma_{\boldsymbol{k}} \\ (S^\sigma_{\boldsymbol{k}})^\dagger & B^\sigma_{\boldsymbol{k}} \end{pmatrix} \begin{pmatrix} \phi_{\boldsymbol{k}m} \\ 0 \end{pmatrix} = \begin{pmatrix} 0 \\ (S^\sigma_{\boldsymbol{k}})^\dagger \phi_{\boldsymbol{k}m} \end{pmatrix} = \begin{pmatrix} 0 \\ 0 \end{pmatrix}, \tag{3.3}$$

since $\phi_{\boldsymbol{k}m}$ is in the kernel of $(S^\sigma_{\boldsymbol{k}})^\dagger$. If $S^\sigma_{\boldsymbol{k}}$ is full rank, i.e. $r_{\boldsymbol{k}} = n_{\tilde{L}}$, there are $n_L - n_{\tilde{L}}$ such states, constituting the flat band(s). Furthermore, these states are localized only on the larger sublattice L. The $\boldsymbol{k}$-points where $r_{\boldsymbol{k}} < n_{\tilde{L}}$ correspond to band touching points between the flat and the dispersive bands.

As shown in Ref. [47], the above result can be further generalized in that the upper-left block of Eq. (3.1) does not necessarily need to be zero for the flat bands to emerge. The generalized statement is this: if we have a matrix of the form

$$\begin{matrix} n_L & n_{\tilde{L}} \end{matrix} \\ \begin{pmatrix} A & S \\ S^\dagger & B \end{pmatrix} \begin{matrix} n_L \\ n_{\tilde{L}} \end{matrix}, \tag{3.4}$$

where A has an eigenvalue a with multiplicity $n_a > n_{\tilde{L}}$, then the whole matrix has the same eigenvalue a with a multiplicity of at least $n_a - n_{\tilde{L}}$. The labels $\boldsymbol{k}, \sigma$ are stripped here to draw attention to the fact that despite the lattice model context, this statement is purely linear-algebraic, resulting only from the structure of the matrix. Next, we will use this result to show that with nearest-neighbour interactions and zero chemical potential, the BdG-Hamiltonian inherits the flat band(s) of the single-particle Hamiltonian.

For a semi-bipartite lattice, a generic nearest-neighbour interaction results in a momentum-space order parameter matrix of the following form:

$$\Delta_{\boldsymbol{k}} = \begin{matrix} n_L & n_{\tilde{L}} \end{matrix} \\ \begin{pmatrix} 0 & \Delta^{\text{UR}}_{\boldsymbol{k}} \\ \Delta^{\text{LL}}_{\boldsymbol{k}} & \Delta^{\text{LR}}_{\boldsymbol{k}} \end{pmatrix} \begin{matrix} n_L \\ n_{\tilde{L}} \end{matrix}, \tag{3.5}$$

where UR stands for upper-right, LL for lower-left and LR for lower-right. The contents of these blocks depend on the specific form of the interaction; for RVB, they are

given by Eq. (2.25). Here, we only need to assume that the upper-left block is zero, i.e. that there are no internal edges in the larger sublattice. With this structure, the BdG-Hamiltonian of the system is

$$H_{\mathrm{BdG}}(\boldsymbol{k}) = \begin{array}{c} \begin{matrix} n_L & n_{\tilde{L}} & n_L & n_{\tilde{L}} \end{matrix} \\ \begin{pmatrix} -\mu\mathbf{1} & S_{\boldsymbol{k}}^{\uparrow} & 0 & \Delta_{\boldsymbol{k}}^{\mathrm{UR}} \\ (S_{\boldsymbol{k}}^{\uparrow})^{\dagger} & B_{\boldsymbol{k}}^{\uparrow} - \mu\mathbf{1} & \Delta_{\boldsymbol{k}}^{\mathrm{LL}} & \Delta_{\boldsymbol{k}}^{\mathrm{LR}} \\ 0 & (\Delta_{\boldsymbol{k}}^{\mathrm{LL}})^{\dagger} & \mu\mathbf{1} & -S_{\boldsymbol{k}}^{\downarrow} \\ (\Delta_{\boldsymbol{k}}^{\mathrm{UR}})^{\dagger} & (\Delta_{\boldsymbol{k}}^{\mathrm{LR}})^{\dagger} & -(S_{\boldsymbol{k}}^{\downarrow})^{\dagger} & -B_{\boldsymbol{k}}^{\downarrow} + \mu\mathbf{1} \end{pmatrix} \begin{matrix} n_L \\ n_{\tilde{L}} \\ n_L \\ n_{\tilde{L}} \end{matrix} \end{array}, \tag{3.6}$$

where μ is the chemical potential and $\mathbf{1}$ is the identity matrix of approriate dimensions. Next, let us permute the second and third rows and columns of this matrix. This is a unitary transformation, so it doesn't change the eigenvalues, which is physically understandable, since such a permutation corresponds only to re-labeling the operators in the corresponding Nambu spinor. The permuted Hamiltonian is

$$\tilde{H}_{\mathrm{BdG}}(\boldsymbol{k}) = \begin{array}{c} \begin{matrix} n_L & n_L & n_{\tilde{L}} & n_{\tilde{L}} \end{matrix} \\ \begin{pmatrix} -\mu\mathbf{1} & 0 & S_{\boldsymbol{k}}^{\uparrow} & \Delta_{\boldsymbol{k}}^{\mathrm{UR}} \\ 0 & \mu\mathbf{1} & (\Delta_{\boldsymbol{k}}^{\mathrm{LL}})^{\dagger} & -S_{\boldsymbol{k}}^{\downarrow} \\ (S_{\boldsymbol{k}}^{\uparrow})^{\dagger} & \Delta_{\boldsymbol{k}}^{\mathrm{LL}} & B_{\boldsymbol{k}}^{\uparrow} - \mu\mathbf{1} & \Delta_{\boldsymbol{k}}^{\mathrm{LR}} \\ (\Delta_{\boldsymbol{k}}^{\mathrm{UR}})^{\dagger} & -(S_{\boldsymbol{k}}^{\downarrow})^{\dagger} & (\Delta_{\boldsymbol{k}}^{\mathrm{LR}})^{\dagger} & -B_{\boldsymbol{k}}^{\downarrow} + \mu\mathbf{1} \end{pmatrix} \begin{matrix} n_L \\ n_L \\ n_{\tilde{L}} \\ n_{\tilde{L}} \end{matrix} \end{array}. \tag{3.7}$$

We can identify the structure of this matrix as similar to Eq. (3.4) but with doubled dimensions. The role of the matrix A in Eq. (3.4) is here played by

$$\begin{array}{c} \begin{matrix} n_L & n_L \end{matrix} \\ \begin{pmatrix} -\mu\mathbf{1} & 0 \\ 0 & \mu\mathbf{1} \end{pmatrix} \begin{matrix} n_L \\ n_L \end{matrix} \end{array}, \tag{3.8}$$

which has eigenvalues $\pm\mu$, both with multiplicity n_L (for non-zero μ) for all $\boldsymbol{k}$. Thus, if $n_L > 2n_{\tilde{L}}$, the BdG-Hamiltonian has at least $n_L - 2n_{\tilde{L}}$ flat bands at $\pm\mu$. Note that in this case the condition $n_L > n_{\tilde{L}}$ is not enough; instead, the larger sublattice needs to have more than twice the number of orbitals of the smaller sublattice. However, if we set $\mu = 0$, the above matrix becomes a zero matrix, the eigenvalues of which are trivially zeros, with multiplicity $2n_L$. In this case, the BdG-Hamiltonian has at least $2n_L - 2n_{\tilde{L}}$ flat bands at zero energy even without the stricter condition.

To summarize, the structure of a semi-bipartite lattice with sublattice sizes $n_L > n_{\tilde{L}}$, where internal edges are allowed only in the smaller sublattice, guarantees the existence of at least $n_L - n_{\tilde{L}}$ flat bands at zero energy. With nearest-neighbour interactions, the BdG-Hamiltonian inherits these flat bands in the following way. If the chemical

potential is zero, each of the single-particle flat bands corresponds to a pair of flat bands in the BdG-spectrum, still at zero energy. For non-zero μ, the behaviour depends on the stricter condition $n_L > 2n_{\tilde{L}}$. If this condition is met, each of the single-particle flat bands splits into a pair of flat bands at $\pm\mu$ in the BdG-spectrum. Otherwise, they might split into dispersive bands.

We note that the form of Eq. (3.4) hints that it should be possible to add some internal edges into the larger sublattice as well while still preserving the existence of the flat bands. This is indeed the case; one can perform analysis similar to the above to conclude that if the larger sublattice L itself has flat bands in its BdG-spectrum, then the BdG-Hamiltonian of the whole lattice can inherit some of these flat bands, provided that the size difference between the sublattices is large enough. For more discussion on what types of lattices are allowed in general, refer to Ref. [47].

3.1.2 Forbidden Pairing in the Flat Bands

It turns out that with nearest-neighbour interactions, pairing cannot occur between particles in the flat bands that emerge by the mechanism described above. This will be demonstrated below. Assume we have a kinetic Hamiltonian $H^{\sigma}_{\boldsymbol{k}}$ of the form in Eq. (3.1) and an orbital-space order parameter matrix $\Delta_{\boldsymbol{k}}$ of the form in Eq. (3.5). Then, by transforming into band basis with Eq. (2.29), we have

$$[\Delta^{\text{band}}_{\boldsymbol{k}}]_{m,n} = [\mathcal{G}^{\dagger}_{\boldsymbol{k}\uparrow}\Delta_{\boldsymbol{k}}\mathcal{G}^{*}_{-\boldsymbol{k}\downarrow}]_{m,n} = \sum_{\alpha\beta}[\mathcal{G}^{\dagger}_{\boldsymbol{k}\uparrow}]_{m,\alpha}[\Delta_{\boldsymbol{k}}]_{\alpha,\beta}[\mathcal{G}^{*}_{-\boldsymbol{k}\downarrow}]_{\beta,n}. \tag{3.9}$$

When m and n both correspond to a flat band, all terms in this sum are zero. This is because for $[\Delta_{\boldsymbol{k}}]_{\alpha,\beta}$ to be non-zero, we need either $\alpha > N_L$ or $\beta > N_L$ (or both). But then either $[\mathcal{G}^{\dagger}_{\boldsymbol{k}\uparrow}]_{m,\alpha} = 0$ or $[\mathcal{G}^{*}_{-\boldsymbol{k}\downarrow}]_{\beta,n} = 0$, since the columns of $\mathcal{G}_{\boldsymbol{k}\uparrow}$ and $\mathcal{G}_{-\boldsymbol{k}\downarrow}$ are the Bloch states, which for the flat bands have the same form as Eq. (3.2). Thus, there is no intra-band pairing in a flat band, nor is there pairing between possible degenerate flat bands.

This result has an intuitive physical meaning. As mentioned in the previous section and indicated by Eq. (3.2), the flat band states are localized on the larger sublattice L. Since we have assumed that there are no internal edges in the larger sublattice, particles on the flat bands are not nearest neighbours with any other flat band particles. Thus, with the interaction covering only nearest-neighbour pairs, pairing between these particles is structurally forbidden.

3.1.3 Example: Lieb Lattice

Next, we take a look at the Lieb lattice for a concrete example of the general results shown in this section. The structure of the lattice is shown in Fig. 2. As shown in the figure, the Lieb lattice is bipartite; the sites can be divided into two sublattices AB and C, with $n_{AB} = 2$ and $n_C = 1$ sites, respectively, such that there are no internal edges in them. Using Eq. (2.24), the momentum-space kinetic Hamiltonian reads

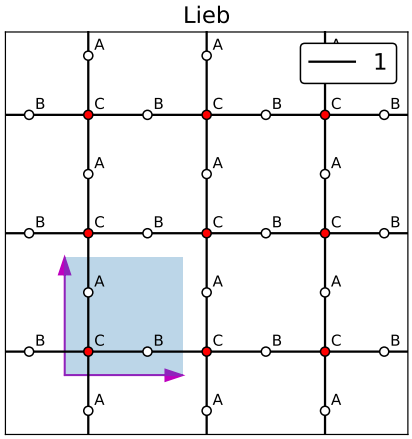

Figure 2: The Lieb lattice. The arrows are the lattice vectors, which define the unit cell; one unit cell is shown shaded in blue. There are three orbitals, or sites in the unit cell; different orbital are denoted with A, B and C. The lattice is bipartite; we can take orbitals A and B (colored in white) to be one sublattice and orbital C (colored in red) to be the other sublattice such that neither sublattice has internal edges. Hopping amplitudes are indicated by lines connecting pairs of nearest-neighbour sites. Here we have set all hopping amplitudes to unity.

$$H_{\boldsymbol{k}} = \begin{pmatrix} 0 & 0 & a_{\boldsymbol{k}} \\ 0 & 0 & b_{\boldsymbol{k}} \\ a_{\boldsymbol{k}} & b_{\boldsymbol{k}} & 0 \end{pmatrix}, \tag{3.10}$$

where $a_{\boldsymbol{k}} = 2\cos\frac{k_x}{2}$ and $b_{\boldsymbol{k}} = 2\cos\frac{k_y}{2}$, with the lattice spacing set to unity. For the purposes of this example, we have also set all of the hopping amplitudes to unity, but this is not necessary for the main results of this section to hold; we only need the bipartiteness of the lattice. We have dropped the spin index σ here, since we assume TRS. Here and henceforth, quantities without the spin index will denote the spin up case (e.g. $H_{\boldsymbol{k}} = H^{\uparrow}_{\boldsymbol{k}}$), and the corresponding spin down quantities can be obtained via transforming $\boldsymbol{k} \to -\boldsymbol{k}$ and taking the appropriate complex conjugates as detailed in previous sections (e.g. $(H^{\downarrow}_{-\boldsymbol{k}})^* = H^{\uparrow}_{\boldsymbol{k}}$). Now, diagonalizing $H_{\boldsymbol{k}}$ yields the single-particle energies $\epsilon_{\boldsymbol{k}m}$

$$\epsilon_{\boldsymbol{k}1} = -\epsilon_{\boldsymbol{k}}, \tag{3.11}$$
$$\epsilon_{\boldsymbol{k}2} = 0, \tag{3.12}$$
$$\epsilon_{\boldsymbol{k}3} = \epsilon_{\boldsymbol{k}}, \tag{3.13}$$

where m labels the band. Here, $\epsilon_{\boldsymbol{k}} = \sqrt{a^2_{\boldsymbol{k}} + b^2_{\boldsymbol{k}}}$, and the bands are numbered from lowest to highest in energy. Here we see the flat band that appears because $n_{AB} - n_C = 1$. The corresponding Bloch states $\Psi_{\boldsymbol{k}m}$ are

$$\Psi_{k1} = \frac{1}{\sqrt{2}\epsilon_k}\begin{pmatrix} -a_k \\ -b_k \\ \epsilon_k \end{pmatrix}, \tag{3.14}$$

$$\Psi_{k2} = \frac{1}{\epsilon_k}\begin{pmatrix} -b_k \\ a_k \\ 0 \end{pmatrix}, \tag{3.15}$$

$$\Psi_{k3} = \frac{1}{\sqrt{2}\epsilon_k}\begin{pmatrix} a_k \\ b_k \\ \epsilon_k \end{pmatrix}, \tag{3.16}$$

showing that the flat band states Ψ_{k2} are localized on the sublattice AB. The orbital-basis order parameter matrix $\Delta_{\boldsymbol{k}}$ has the form

$$\Delta_{\boldsymbol{k}} = \begin{pmatrix} 0 & 0 & \Delta_{13}(\boldsymbol{k}) \\ 0 & 0 & \Delta_{23}(\boldsymbol{k}) \\ \Delta^*_{13}(\boldsymbol{k}) & \Delta^*_{23}(\boldsymbol{k}) & 0 \end{pmatrix}, \tag{3.17}$$

where $\Delta_{13}(\boldsymbol{k})$ and $\Delta_{23}(\boldsymbol{k})$ are given by Eq. (2.25). Inserting all of this into the BdG-Hamiltonian (Eq. (2.23)) and diagonalizing gives the many-body energies $E^{\pm}_{\boldsymbol{k}m}$

$$E^{\pm}_{\boldsymbol{k}1} = 0, \tag{3.18}$$

$$E^{\pm}_{\boldsymbol{k}2} = \pm\sqrt{a_{\boldsymbol{k}}^2 + b_{\boldsymbol{k}}^2 + |\Delta_{13}|^2 + |\Delta_{23}|^2 + 2|a_{\boldsymbol{k}}\,\mathrm{Im}\,\Delta_{13} + b_{\boldsymbol{k}}\,\mathrm{Im}\,\Delta_{23}|}, \tag{3.19}$$

$$E^{\pm}_{\boldsymbol{k}3} = \pm\sqrt{a_{\boldsymbol{k}}^2 + b_{\boldsymbol{k}}^2 + |\Delta_{13}|^2 + |\Delta_{23}|^2 - 2|a_{\boldsymbol{k}}\,\mathrm{Im}\,\Delta_{13} + b_{\boldsymbol{k}}\,\mathrm{Im}\,\Delta_{23}|}, \tag{3.20}$$

where the chemical potential has been set to zero, and, for brevity, the $\boldsymbol{k}$-dependence of the order parameters has been suppressed. As expected, we have two flat bands at zero energy. Next, by transforming the order parameter matrix into band basis using Eq. (2.29) and the eigenvectors in Eqs. (3.14)-(3.16) yields

$$\Delta^{\mathrm{band}}_{\boldsymbol{k}} = \begin{pmatrix} -\,\mathrm{Re}\,z_1 & z_2 & -i\,\mathrm{Im}\,z_1 \\ z_2^* & 0 & z_2^* \\ i\,\mathrm{Im}\,z_1 & z_2 & \mathrm{Re}\,z_1, \end{pmatrix} \tag{3.21}$$

where $z_1 = \frac{1}{\epsilon_k}(a_{\boldsymbol{k}}\Delta_{13} + b_{\boldsymbol{k}}\Delta_{23})$, $z_2 = \frac{1}{\sqrt{2}\epsilon_k}(a_{\boldsymbol{k}}\Delta^*_{23} - b_{\boldsymbol{k}}\Delta^*_{13})$. As shown by the zero on the diagonal, there is no intra-band pairing in the flat band. The two other terms on the diagonal are the intra-band pairings on the dispersive bands, while the off-diagonal terms give the various inter-band pairings.

3.2 Quantum Criticality: Minimum Interaction Strength

At the heart of BCS theory is the idea that an arbitrarily weak attractive interaction is enough for two electrons near the Fermi surface to form a Cooper pair. This was first

demonstrated by Cooper in 1956 [9] for a simple model of two electrons. However, more recent studies suggest that for some models, a finite, non-zero interaction strength is required before pairing becomes energetically advantageous for the system as a whole. This minimum interaction strength is a quantum critical point (QCP); it marks the transition from a normal state without pairing (and thus without superconductivity) to a BCS state with non-zero pairing (where superconductivity is possible). QCPs have been found, for example, for the honeycomb lattice (which is used to model, e.g., graphene) with both on-site [33–39] and RVB [23–25, 37] interactions, for the π-flux square lattice with on-site interactions [39], and for the checkerboard lattice with (non-RVB) nearest-neighbour interactions [40]. Later in Section 5, we report our findings of QCPs for other models as well. Anticipating those results, in this section we seek to understand the possible causes of QCPs.

A common feature in the models where QCPs have been found is the existence of Dirac points in the single-particle energy spectrum of a given model. A Dirac point is a linear band touching point, i.e. a point in $\boldsymbol{k}$-space where two energy bands touch in such a way that dispersion near the touching point is linear; this is what happens, for example, in the honeycomb lattice at half-filling, as we will see later. A distinctive feature of a Dirac point is that its density of states (DoS) is zero. This is in contrast to another common type of band touching, a quadratic band touching point (QBTP), where the DoS is non-zero, even though for both Dirac points and QBTPs the Fermi surface shrinks to a single point. Generic depictions of a Dirac point, a QBTP and the corresponding densities of states are shown in Fig. 3. In the following, we will consider some simplified cases where the grand potential Ω can be minimized analytically to investigate possible causes for the QCPs, and see how the DoS might affect pairing at low interaction strengths. Specifically, we will derive an upper bound for the critical interaction strength, marking the transition from a normal to a BCS state, in two scenarios, one of which concerns on-site pairing, while the other is applicable to RVB pairing.

3.2.1 On-site Interactions: Uniform s-wave Pairing

The first scenario we will cover is the assumption that the order parameter matrix in band basis is proportional to the identity matrix, $\Delta_{\boldsymbol{k}}^{\text{band}} = \Delta\mathbf{1}$, where $\mathbf{1}$ is the $n_{\text{orb}} \times n_{\text{orb}}$ identity matrix, with n_{orb} the number of orbitals. In other words, we assume (1) only intra-band pairing, since $\Delta_{\boldsymbol{k}}^{\text{band}}$ is diagonal, (2) s-wave pairing symmetry, meaning $\Delta_{\boldsymbol{k}}^{\text{band}}$ doesn't depend on $\boldsymbol{k}$, and (3) that the diagonal elements of $\Delta_{\boldsymbol{k}}^{\text{band}}$ are all equal, namely Δ. In systems with TRS, this is equivalent to assuming on-site interactions with $\boldsymbol{k}$-independent uniform pairing (uniform over orbitals), since by Eq. (2.29) we have $\Delta\mathbf{1} = \Delta_{\boldsymbol{k}}^{\text{band}} = \mathcal{G}_{\boldsymbol{k}}^{\dagger}\Delta_{\boldsymbol{k}}\mathcal{G}_{\boldsymbol{k}} \Leftrightarrow \Delta_{\boldsymbol{k}} = \Delta\mathbf{1}$, as $\mathcal{G}_{\boldsymbol{k}}$ is unitary. In the next section, we will consider a similar scenario with RVB interactions.

The above assumption lets us write the BdG-Hamiltonian in the band basis as

$$\tilde{H}_{\text{BdG}}(\boldsymbol{k}) = \begin{pmatrix} \boldsymbol{\epsilon}_{\boldsymbol{k}} - \mu\mathbf{1} & \Delta\mathbf{1} \\ \Delta^{*}\mathbf{1} & -\boldsymbol{\epsilon}_{\boldsymbol{k}} + \mu\mathbf{1} \end{pmatrix}, \tag{3.22}$$

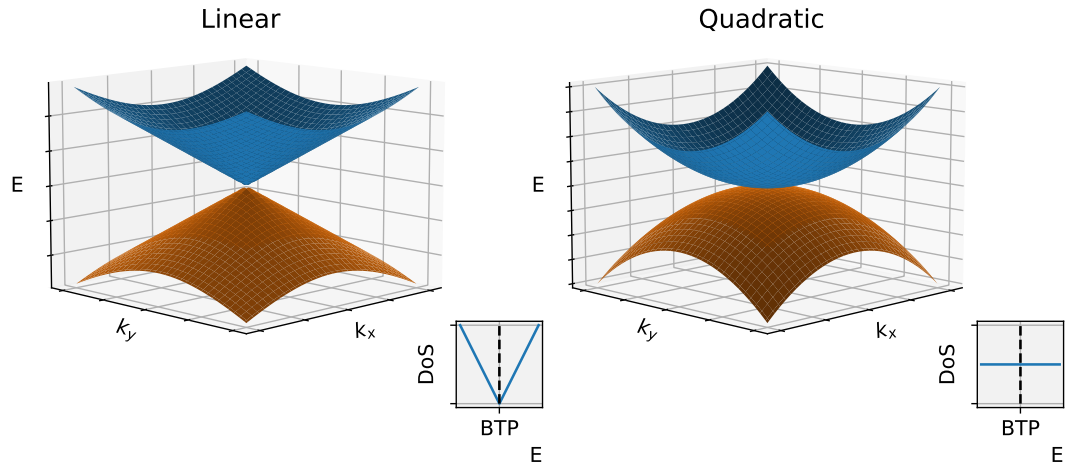

Figure 3: A cartoon of a linear and a quadratic band touching point. The smaller subfigures show the corresponding densities of states: for a Dirac point (a linear BTP), the DoS vanishes while for a QBTP it stays constant.

where $\boldsymbol{\epsilon_k}$ is a diagonal matrix containing the single-particle energies $\epsilon_{\boldsymbol{k}m}$, and Δ is a constant. Since the order parameters have an overall phase freedom, we can choose Δ to be real. Because the off-diagonal blocks are diagonal themselves, the eigenvalues of this matrix are particularly simple. In particular, we can permute the rows and columns in such a way that the whole matrix itself becomes block-diagonal, with 2×2 blocks

$$H_{\text{block},m} = \begin{pmatrix} \epsilon_{\boldsymbol{k}m} - \mu & \Delta \\ \Delta & -\epsilon_{\boldsymbol{k}m} + \mu \end{pmatrix}. \tag{3.23}$$

Note that this transformation is unitary, so it doesn't change the eigenvalues. The blocks can then be diagonalized independently, yielding the energies

$$E^{\pm}_{\boldsymbol{k}m} = \pm\sqrt{(\epsilon_{\boldsymbol{k}m} - \mu)^2 + \Delta^2}. \tag{3.24}$$

Next, we calculate the grand potential at zero temperature via Eq. (2.43) to get

$$\Omega = \sum_{\boldsymbol{k}m} \left(-\sqrt{(\epsilon_{\boldsymbol{k}m} - \mu)^2 + \Delta^2} \right) + \frac{n_{\text{orb}} N_c}{J} \Delta^2, \tag{3.25}$$

where the constant terms have been ignored. The ground state of the system minimizes Ω. Taking the derivative of Ω and setting it to zero gives, in the thermodynamical limit $N_c \to \infty$,

$$\frac{\mathrm{d}\Omega}{\mathrm{d}\Delta} = \sum_{\boldsymbol{k}m} -\frac{\Delta}{\sqrt{(\epsilon_{\boldsymbol{k}m}-\mu)^2+\Delta^2}} + \frac{2n_{\mathrm{orb}}N_c}{J}\Delta = 0 \tag{3.26}$$

$$\Rightarrow \frac{2n_{\mathrm{orb}}}{J} = \sum_m \frac{1}{A}\int_{\mathrm{B.Z}} \frac{1}{\sqrt{(\epsilon_{\boldsymbol{k}m}-\mu)^2+\Delta^2}}\mathrm{d}^2\boldsymbol{k}, \tag{3.27}$$

where the integral is over the Brillouin zone, with A its area (volume in 3D). This is where the importance of the Fermi surface and its DoS comes in. The left-hand side becomes arbitrarily large when J is small; thus, for there to be a solution for any non-zero J, we need the integral on the right-hand side to diverge when $\Delta \to 0$. In other words, we need a non-zero density of states at the Fermi surface (where $\epsilon_{\boldsymbol{k}} = \mu$). If we now assume two bands with energies $\epsilon = \pm\epsilon_{\boldsymbol{k}}$, and a simple linear dispersion, $\epsilon_{\boldsymbol{k}} = \sqrt{k_x^2 + k_y^2}$, we get a Dirac point with a vanishing DoS at $\boldsymbol{k} = 0$. Setting the Fermi surface to this point, i.e. $\mu = 0$, we arrive at (with now $n_{\mathrm{orb}} = 2$)

$$\frac{4}{J} = \frac{1}{A}\int\int_{\mathrm{B.Z}} \frac{2}{\sqrt{k_x^2+k_y^2+\Delta^2}}\,\mathrm{d}k_x\,\mathrm{d}k_y \tag{3.28}$$

$$\frac{4}{J} = \frac{1}{A}\int\int_{\mathrm{B.Z}} \frac{2k}{\sqrt{k^2+\Delta^2}}\,\mathrm{d}k\,\mathrm{d}\theta, \tag{3.29}$$

where in the last row we have switched to polar coordinates. This form highlights the finiteness of this integral: even if we make Δ really small, the integrand just becomes a constant (strictly speaking we cannot simply set $\Delta = 0$, since we have divided by Δ in Eq. (3.26); the derivative of Ω is always zero if $\Delta = 0$).

Regardless of the shape of the Brillouin zone, the integral in Eq. (3.29) does not diverge, which means that there must be a minimum value of J below which there is no solution. For the purposes of the example, we continue by approximating the Brillouin zone as a circular disk of radius k_{max}, which allows us perform the integral to get

$$\frac{4}{J} = \frac{1}{\pi k_{\mathrm{max}}^2}\int_0^{2\pi}\int_0^{k_{\mathrm{max}}} \frac{2k}{\sqrt{k^2+\Delta^2}}\,\mathrm{d}k\,\mathrm{d}\theta \tag{3.30}$$

$$\frac{4}{J} = \frac{4}{k_{\mathrm{max}}^2}\left(\sqrt{k_{\mathrm{max}}^2+\Delta^2} - |\Delta|\right) \tag{3.31}$$

$$\Leftrightarrow |\Delta| = \frac{J}{2} - \frac{k_{\mathrm{max}}^2}{2J} = \frac{1}{2J}\left(J^2 - k_{\mathrm{max}}^2\right). \tag{3.32}$$

This can only have a solution if $J > k_{\mathrm{max}}$, showing that a QCP emerges due to the Dirac point. In other words, a linear dispersion near the Fermi surface is not enough for pairing to be possible with an arbitrarily weak interaction. On the contrary, if we assume a quadratic dispersion, $\epsilon_{\boldsymbol{k}} = k_x^2 + k_y^2$, Eq. (3.27) becomes (in polar coordinates)

$$\frac{4}{J} = \frac{1}{A} \int \int_{\text{B.Z.}} \frac{2k}{\sqrt{k^4 + \Delta^2}} \, \mathrm{d}k \, \mathrm{d}\theta. \tag{3.33}$$

This time, the integral on the right-hand side diverges near $\Delta = 0$ (as long as $\boldsymbol{k} = 0$ is included in the Brillouin zone), and thus a solution exists for any finite J.

If we now move the Fermi surface away from the band-touching point by changing to a non-zero chemical potential, there is always a solution even with linear dispersion. In the linear case, the radial parts of the two integrals in Eq. (3.27) become of the form

$$\int \frac{k}{\sqrt{(k \pm \mu)^2 + \Delta^2}} \, \mathrm{d}k = \sqrt{(k \pm \mu)^2 + \Delta^2} \pm \mu \ln \left(\sqrt{(k \pm \mu)^2 + \Delta^2} - k \mp \mu \right), \tag{3.34}$$

where now the logarithmic term gives the desired divergence: we have $\sqrt{(k \pm \mu)^2 + \Delta^2} - k \mp \mu \to |\mu| \mp \mu$ when $\Delta, k \to 0$, which means that depending on the sign of μ, the argument of the logarithm resulting from either the first or the second integral goes to zero. Note that this is an indefinite integral, and the divergence is achieved when plugging in the lower bound value $k = 0$. The quadratic case gives a similar logarithmic term with a divergence.

The model developed in this section offers an explanation of why pairing in some cases might not be possible at low interaction strengths. The main gist is that since all we really care about is whether the integrals in Eq. (3.27) diverge or not, we conclude that only the behaviour of the single-particle spectrum near the Fermi surface matters. We should therefore expect that even though a globally linear dispersion was assumed here, a locally linear dispersion near a band-touching point (i.e. a Dirac point) should be sufficient to cause a QCP. Physically, it seems that at a Dirac point there are not "enough" states near the Fermi energy for pairing to occur at low interaction strengths. Indeed, even though with both linear and quadratic band touchings the Fermi surface shrinks to a single point, in the first case the density of states goes to zero, while in the latter case it does not.

Moreover, it is reasonable to assume that a similar mechanism could produce a QCP even if we give up the uniform s-wave pairing assumption. This would introduce a $\boldsymbol{k}$-dependence to the order parameters in band basis and thus a bunch of new degrees of freedom, but when the Fermi surface is set to a Dirac point, we still cannot make the integrals in Eq. (3.27) diverge by just tuning the order parameters; the $(\epsilon_{\boldsymbol{k}m} - \mu)^2$ term in the denominator grows too fast near the Fermi surface. On the other hand, the issue of adding inter-band pairing is more complicated. In that case, the energies in Eq. (3.24) no longer have such a simple form, and it is not as straightforward to take derivatives to see what happens in the small-order-parameter limit.

Nevertheless, because we have minimized the grand potential with extra assumptions, i.e. extra restrictions, the value for the critical interaction strength obtained by considering the $\Delta \to 0$ limit in Eq. (3.27) is an upper bound for the true QCP, even if the uniform s-wave assumption is not satisfied. Furthermore, the numerical results we

present later in Section 5 indicate that, at least in some cases, this simplified analysis gives surprisingly accurate results even with more complicated pairing schemes. However, this upper bound is applicable only to systems that *could* have uniform s-wave pairing. By the analysis done at the start of this section, this means exactly those systems with only on-site pairing, since uniform s-wave pairing is equivalent to uniform on-site pairing in real space. In particular, these results are not applicable to RVB pairing, since in that case there is no way to choose the real-space order parameters $\Delta_{i\alpha j\beta}$ so that $\Delta^{\text{band}}_{\boldsymbol{k}}$ is proportional to identity. Luckily, using a slightly different pairing symmetry assumption, it is possible to do derive an analogous result for RVB pairing. Next, we will do just that, before discussing the nature of these upper bounds and the pairing symmetry assumptions in more detail.

3.2.2 RVB Interactions: Extended s-wave Pairing

In the previous section we assumed only intra-band pairing with uniform s-wave pairing symmetry, which is equivalent to assuming on-site interactions with $\boldsymbol{k}$-independent uniform pairing at all sites. It turns out that, in a similar fashion, we can construct an argument for models with RVB interactions to explain why and when a QCP exists. This time, we are going to consider a situation where the orbital-basis order parameter matrix, $\Delta_{\boldsymbol{k}}$, is a multiple of the kinetic Hamiltonian $H_{\boldsymbol{k}}$ (we assume TRS and drop the spin indices in this section). Recalling the definitions of these matrices (with RVB pairing),

$$[H_{\boldsymbol{k}}]_{\alpha,\beta} = \sum_j t_{0\alpha j\beta} e^{i\boldsymbol{k}\cdot\boldsymbol{r}^{\Delta}_{0\alpha j\beta}}, \tag{3.35}$$

$$[\Delta_{\boldsymbol{k}}]_{\alpha,\beta} = -\sum_j I_{0\alpha j\beta}\Delta_{0\alpha j\beta} e^{i\boldsymbol{k}\cdot\boldsymbol{r}^{\Delta}_{0\alpha j\beta}}, \tag{3.36}$$

we see that this is the case when the real-space order parameters are given by some fixed multiple of the corresponding hopping amplitude, i.e. when $\Delta_{0\alpha j\beta}/t_{0\alpha j\beta}$ is a constant. One typical scenario where this situation arises is when both the hopping amplitudes and the real-space order parameters are uniform, i.e. constant. There is, however, one important restriction: with RVB (or any other nearest-neighbour) interactions, $\Delta_{\boldsymbol{k}}$ cannot have constant ($\boldsymbol{k}$-independent) terms on its diagonal, because this would imply that $\Delta_{0\alpha 0\alpha} \neq 0$ for some orbital α, i.e on-site pairing. The order parameter matrix $\Delta_{\boldsymbol{k}}$ thus cannot be a multiple of $H_{\boldsymbol{k}}$ if the diagonal of $H_{\boldsymbol{k}}$ has constant terms. This means that for the results of this section to apply, the on-site energies of all sites must be equal, and furthermore the chemical potential μ must be defined in such a way that this on-site energy is zero. Note that this does not necessarily mean that the diagonal of $H_{\boldsymbol{k}}$ must be zero, as an orbital could be connected to itself in another unit cell, producing a $\boldsymbol{k}$-dependent term to the diagonals of both $H_{\boldsymbol{k}}$ and $\Delta_{\boldsymbol{k}}$ without needing on-site pairing. Apart from this restriction, it is always possible to choose the real-space order parameters $\Delta_{0\alpha j\beta}$ such that $\Delta_{\boldsymbol{k}}$ is a multiple of $H_{\boldsymbol{k}}$.

Let us assume a lattice where the this criterion is satisfied, and denote simply

$\Delta_{0\alpha \boldsymbol{j}\beta}/t_{0\alpha \boldsymbol{j}\beta} = \Delta$. Using the phase freedom, we can choose this constant to be real. This gives the BdG-Hamiltonian in orbital basis

$$H_{\mathrm{BdG}}(\boldsymbol{k}) = \begin{pmatrix} H_{\boldsymbol{k}} - \mu\mathbf{1} & -\Delta H_{\boldsymbol{k}} \\ -\Delta H_{\boldsymbol{k}} & -H_{\boldsymbol{k}} + \mu\mathbf{1} \end{pmatrix}, \tag{3.37}$$

where $\mathbf{1}$ is the identity matrix of appropriate dimensions. The main consequence of this assumption is that the blocks of the BdG-Hamiltonian are simultaneously diagonalizable. Moving to band basis, we have

$$\tilde{H}_{\mathrm{BdG}}(\boldsymbol{k}) = \begin{pmatrix} \boldsymbol{\epsilon}_{\boldsymbol{k}} - \mu\mathbf{1} & -\Delta\boldsymbol{\epsilon}_{\boldsymbol{k}} \\ -\Delta\boldsymbol{\epsilon}_{\boldsymbol{k}} & -\boldsymbol{\epsilon}_{\boldsymbol{k}} + \mu\mathbf{1} \end{pmatrix}, \tag{3.38}$$

where $\boldsymbol{\epsilon}_{\boldsymbol{k}}$ is a diagonal matrix containing the single-particle energies $\epsilon_{\boldsymbol{k}m}$. Similarly to the on-site case in the previous section, we have only intra-band pairing since the order parameter matrix is diagonal, $\Delta_{\boldsymbol{k}}^{\mathrm{band}} = -\Delta\boldsymbol{\epsilon}_{\boldsymbol{k}}$. The difference is that now the band-basis order parameters have a $\boldsymbol{k}$-dependence. More specifically, they have the same $\boldsymbol{k}$-dependence as the dispersion relations; this is called the extended s-wave symmetry.

From here, we can perform the same analysis as in the previous section: diagonalize $\tilde{H}_{\mathrm{BdG}}(\boldsymbol{k})$, calculate the grand potential Ω, and find its minimum with respect to Δ. First, the energies are

$$E_{\boldsymbol{k}m}^{\pm} = \pm\sqrt{(\epsilon_{\boldsymbol{k}m} - \mu)^2 + \Delta^2\epsilon_{\boldsymbol{k}m}^2}, \tag{3.39}$$

which gives the grand potential (from Eq. (2.41), at zero temperature)

$$\Omega = \sum_{\boldsymbol{k}m}\left(-\sqrt{(\epsilon_{\boldsymbol{k}m} - \mu)^2 + \Delta^2\epsilon_{\boldsymbol{k}m}^2}\right) + \frac{CN_c}{J}\Delta^2 \tag{3.40}$$

with $C = \sum_{\boldsymbol{j}\alpha\beta}|t_{0\alpha \boldsymbol{j}\beta}|^2$. Taking the derivative and setting it to zero gives, in the thermodynamical limit $N_c \to \infty$,

$$\frac{\mathrm{d}\Omega}{\mathrm{d}\Delta} = \sum_{\boldsymbol{k}m} -\frac{\Delta\epsilon_{\boldsymbol{k}m}^2}{\sqrt{(\epsilon_{\boldsymbol{k}m} - \mu)^2 + \Delta^2\epsilon_{\boldsymbol{k}m}^2}} + \frac{2CN_c}{J}\Delta = 0 \tag{3.41}$$

$$\Rightarrow \frac{2C}{J} = \sum_m \frac{1}{A}\int_{\mathrm{B.Z}} \frac{\epsilon_{\boldsymbol{k}m}^2}{\sqrt{(\epsilon_{\boldsymbol{k}m} - \mu)^2 + \Delta^2\epsilon_{\boldsymbol{k}m}^2}}\mathrm{d}^2\boldsymbol{k}, \tag{3.42}$$

where the integral is over the first Brillouin zone (B.Z), with A its area (volume in 3D). Once we again we arrive at a situation where, for a solution to exist for an arbitrarily small interaction strength J, we need one of the integrals on the right-hand side to

diverge as $\Delta \to 0$. However, there is an important distinction to the on-site case and Eq. (3.27): the $\epsilon_{\boldsymbol{k}m}^2$ in the numerator (and as a coefficient of Δ in the denominator) of the integrands. The presence of this term means that states at zero energy have no weight in this integral. This holds also for $\mu = 0$, corresponding to the fact that the energies in Eq. (3.39) reduce to $\pm\mu$ when $\epsilon_{\boldsymbol{k}m} = 0$, which, curiously, means that the states at zero energy do not contribute to pairing even if they are exactly on the Fermi surface. We shall comment on the physical meaning of this result later, but for now, let us continue with Eq. (3.42). We conclude again that there needs to be "enough" states near the Fermi surface so that some of the integrals on the right-hand side can diverge when $\Delta \to 0$. The details depend on the specific form of $\epsilon_{\boldsymbol{k}m}$, but rough analysis shows that once again linear dispersion near μ is likely not enough: with $\epsilon_{\boldsymbol{k}m} = \mu + |\boldsymbol{k}|$ near μ, the numerator becomes of the form $|\boldsymbol{k}|(\mu + |\boldsymbol{k}|)^2$ (with the extra $|\boldsymbol{k}|$ from a switch to polar coordinates), while the denominator is of first order in $|\boldsymbol{k}|$ when $\Delta \to 0$. The factors of $|\boldsymbol{k}|$ cancel out, and the resulting integral does not diverge.

In the special case $\mu = 0$ we can actually solve Eq. (3.42) for Δ analytically, as the order parameter becomes disentangled from the integrals. We get

$$\frac{2C}{J} = \frac{1}{\sqrt{1+\Delta^2}} \sum_m \frac{1}{A} \int_{\mathrm{B.Z}} \frac{\epsilon_{\boldsymbol{k}m}^2}{\sqrt{\epsilon_{\boldsymbol{k}m}^2}} \mathrm{d}^2\boldsymbol{k} \tag{3.43}$$

$$\Leftrightarrow \sqrt{1+\Delta^2} = \frac{J}{2C} S \tag{3.44}$$

$$\Leftrightarrow \Delta = \sqrt{\frac{J^2 S^2}{4C^2} - 1}, \tag{3.45}$$

where

$$S = \sum_m \frac{1}{A} \int_{\mathrm{B.Z}} |\epsilon_{\boldsymbol{k}m}| \mathrm{d}^2\boldsymbol{k}. \tag{3.46}$$

Since Δ is real, a solution exists only if $J > 2C/S$. Note that S can never diverge, so with the extended s-wave pairing symmetry and $\mu = 0$, there is always a QCP, i.e. pairing is not possible for low enough interaction strengths. With the Fermi surface set to zero energy, S can be interpreted as n_{orb} times the average distance (in energy) from the Fermi surface, where n_{orb} is the number of orbitals. At first glance this seems counterintuitive, since it indicates that taking states away from the Fermi surface would enhance pairing. However, we must remember that the constant C, defined as $C = \sum_{\boldsymbol{j}\alpha\beta} |t_{0\alpha\boldsymbol{j}\beta}|^2$, also depends on the single-particle energies (or the other way around, physically speaking): if the overall scale of the hopping amplitudes is t, then $S \sim t$ and $C \sim t^2$, so that for a given J increasing the hopping amplitudes weakens pairing, as we would expect.

At this point, let us briefly consider the specific example of the Lieb lattice with uniform hopping amplitudes $t = 1$ and $\mu = 0$, i.e. with the Fermi energy set to the

flat band. The structure of the lattice was shown in Fig. 2, while the single-particle energies were calculated in Eqs. (3.11)-(3.13). Then, with the assumption of extended s-wave pairing, Eq. (3.45) gives

$$\Delta = \sqrt{\frac{J^2 S^2}{4C^2} - 1} \approx \sqrt{0.057 J^2 - 1}, \tag{3.47}$$

with $C = 8$, and

$$S = 2 \cdot \frac{1}{4\pi^2} \int_{-\pi}^{\pi} \int_{-\pi}^{\pi} 2\sqrt{\cos^2 \frac{k_x}{2} + \cos^2 \frac{k_y}{2}} \, \mathrm{d}k_x \, \mathrm{d}k_y \approx 3.83. \tag{3.48}$$

The QCP is then predicted to be at $J = 2C/S \approx 4.18$. In Section 5 we will see that the Lieb lattice with RVB interactions indeed has a QCP, and furthermore the value we get for it numerically is very close to this prediction, even though it turns out that the actual ground state does not have the extended s-wave symmetry.

Some remarks on the results of this section are in order. First, in theoretical models we are typically free to choose the zero-point of energy as we please: only energy differences matter. With this is mind, Eq. (3.42) begs the question: what is so special about the states that have zero energy? Why do they not contribute to pairing? Mathematically, the answer is simple enough: we have assumed that $\Delta_{\boldsymbol{k}}$ is a multiple of $H_{\boldsymbol{k}}$, which necessarily means that the order parameters vanish at the same $\boldsymbol{k}$-points where the energies are zero. What happens if we now shift the energy bands by some constant? Recalling the discussion at the start of this section, this would introduce constant terms to the diagonal of $\Delta_{\boldsymbol{k}}$ and as such, extended s-wave pairing is no longer possible for a system with RVB interactions. The zero-point of energy therefore has a fixed meaning in this context: the chemical potential must be defined in such a way that on-site energies of the lattice sites are zero; otherwise, for extended s-wave pairing to be possible, the whole Hamiltonian of the model must be changed to include on-site interactions on top of RVB, which would naturally drastically alter the properties of the system.

A second point we want to emphasize is that the results of this section hold only for the specific case of extended s-wave pairing. Typically, for a given lattice there could be multiple competing order parameter symmetries, meaning multiple local minima of the grand potential. Which one of these is most favorable, i.e. the global minimum, depends on the specific model parameters. We emphasize that it is not at all clear whether the results of this section should hold, quantitatively or qualitatively, for any other type of pairing symmetry. That is, if the extended s-wave symmetry is a possible solution to a given system and it yields a QCP at some $J = J_{\mathrm{min}}$, there could still be other solutions with a different transition point, or without a QCP at all. A priori, it is entirely feasible that below J_{min} there could be some other configuration of non-zero order parameters that lowers Ω from its value in the case without pairing, even if the extended s-wave configuration requires a larger J to produce such a solution. Put another way, the QCP predicted by assuming an extended s-wave solution might not

be a true QCP of the system. However, similarly to the conclusion at the end of the previous section, we can conclude that the predicted QCP is necessarily an upper bound for the true QCP. This is because we have minimized Ω with the additional restriction of extended s-wave pairing, which means that with an interaction strength larger than the predicted $J_{\min}$ a solution with a value of Ω lower than in the zero-pairing case must exists by definition.

To summarize the results of this section, we have shown that solutions with the extended s-wave symmetry are susceptible to QCPs depending on the behaviour of the single-particle energies near the Fermi surface. For a given interaction strength J, Eq. (3.42) gives $\Delta = \Delta_{0\alpha j\beta}/t_{0\alpha j\beta}$, the coefficient linking the real-space order parameters to the corresponding hopping amplitudes (this coefficient being a constant by assumption). Conversely, the QCP can be solved from the same equation by solving for J while letting $\Delta \to 0$, with the understanding that if any of the integrals on the right-hand side diverge, there is no QCP. This is in parallel to the previous section, where the analogous equation is Eq. (3.27). Here, in the particular case of $\mu = 0$, Δ can be solved explicitly and is given by Eq. (3.45), in which case a QCP is always present. An extended s-wave solution is mathematically possible whenever the kinetic Hamiltonian $H_{\boldsymbol{k}}$ does not have constant terms on its diagonal, and when this is the case, the critical value of J predicted with the extended s-wave assumption is an upper bound of the real critical value, even if the ground state of the system does not have the extended s-wave symmetry.

These results have a strong resemblance to the results of Section 3.1, so let us take a moment to compare them. In Section 3.1, we showed that for bipartite lattices with unequal sublattice sizes, the states on the flat band at zero energy (which every such lattice necessarily has) do not contribute to pairing in the sense that (1) intra-flat-band pairing is forbidden, and (2) when the chemical potential is set to the flat band, $\mu = 0$, the BdG-spectrum also has flat bands at zero energy. In the context of the analysis done in this section, the important thing is that the flat bands of the BdG-spectrum do not depend on Δ, which means that they do not contribute the derivative of Ω. Furthermore, we showed that for non-zero μ, the flat band splits into $\pm\mu$ if the size difference between the sublattices is large enough. These results are independent of any assumptions about order parameter symmetries (they assume only a generic nearest-neighbour interaction), but they do require a specific structure from the lattice. In contrast, in this section we have only assumed the absence of on-site energies in the lattice, but we have additionally assumed a specific order-parameter symmetry, namely the extended s-wave symmetry. This led us to a similar result in that the states at zero energy do not contribute to pairing.

3.2.3 Beyond Density of States: the Weighted Density of Pairs

So far we have presented mathematical arguments why a QCP might emerge when there are not enough states near the Fermi surface of the non-interacting system. In this section, we are going to discuss this more intuitively. The previous results suggest that the density of states could be used as a heuristic for the existence of a QCP: a vanishing density of states at the Fermi surface led to a QCP. The idea behind this is

that in a non-interacting scenario, the states of the system are filled up to the Fermi surface. When we then add an interaction with a small strength J, pairing first occurs between states near the Fermi surface. Thus, if there are very few states at the Fermi surface, no pairs form for very weak interactions, since J sets the energy scale of the pairing process.

Let us further refine this concept. We argue that a non-zero DoS is a necessary, but not a sufficient condition for pairing to occur at arbitrarily low interaction strenghts. Cooper pairs do not form between any two states; they form between states with quasi-momenta $\boldsymbol{k}$ and $-\boldsymbol{k}$, and with spin singlet pairing such as RVB, their spins also have to be of opposite signs. Moreover, when we have nearest-neighbour interactions, the states must be at least partially localized on neighboring sites in real space; otherwise, they cannot form a pair since they do not interact by definition. In systems with TRS, the first two points are largely irrelevant, since $\epsilon_{\boldsymbol{k}m\uparrow} = \epsilon_{-\boldsymbol{k}m\downarrow}$ guarantees that for each state at the Fermi surface we also have a state with the same energy but opposite quasi-momentum and spin. On the other hand, in light of the results from Section 3.1, the matter of localization deserves some attention. In the Lieb lattice example, we saw that with nearest-neighbour interactions, intra-band pairing in the flat band is not possible at all due to the localization properties of the wave functions. In accordance with the results of the previous section, and foreshadowing the results that we will present in Section 5, it could thus make sense to simply ignore the flat band and its associated diverging density of states when analyzing the weak-interactions règime.

Using this idea, we define a concept analogous to the density of states called the *weighted density of pairs* (WDoP). Whereas the DoS simply calculates the number of states at a certain energy,

$$\mathrm{DoS}(\epsilon) \propto \sum_{\boldsymbol{k}m\sigma} \delta(\epsilon - \epsilon_{\boldsymbol{k}m\sigma}), \tag{3.49}$$

where δ is the Dirac delta function, the WDoP calculates the number of suitable pairs of states to form Cooper pairs, weighted by how localized they are to neighboring orbitals. In particular, we define

$$\mathrm{WDoP}(\epsilon) \propto \sum_{\boldsymbol{k}mn} w_{\boldsymbol{k}mn} \delta(\epsilon - \epsilon_{\boldsymbol{k}m\uparrow}) \delta(\epsilon - \epsilon_{-\boldsymbol{k}n\downarrow}), \tag{3.50}$$

where the weights $w_{\boldsymbol{k}mn}$ are given by

$$w_{\boldsymbol{k}mn} = \sum_{\alpha\beta} I_{\alpha\beta} |[\mathcal{G}_{\boldsymbol{k}\uparrow}]_{\alpha,m}|^2 |[\mathcal{G}_{-\boldsymbol{k}\downarrow}]_{\beta,n}|^2, \tag{3.51}$$

where $I_{\alpha\beta} = 1$ if orbitals α and β are nearest neighbours (for nearest-neighbour interactions), and zero otherwise. Recall that the columns of $\mathcal{G}_{\boldsymbol{k}\uparrow}$ and $\mathcal{G}_{-\boldsymbol{k}\downarrow}$ are the Bloch states, so $|[\mathcal{G}_{\boldsymbol{k}\uparrow}]_{\alpha,m}|^2$ and $|[\mathcal{G}_{-\boldsymbol{k}\downarrow}]_{\beta,n}|^2$ give the localization coefficient of the

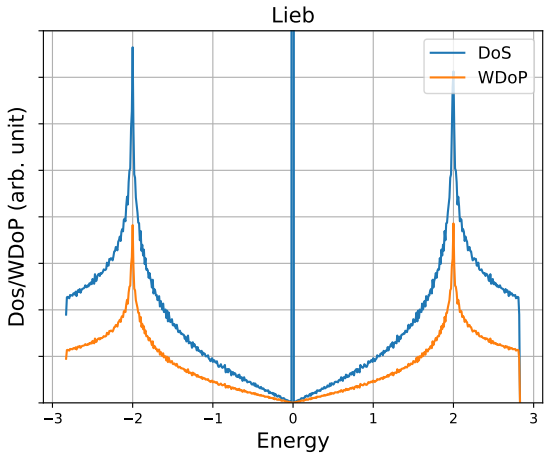

Figure 4: The density of states (DoS) and the weighted density of pairs (WDoP) for the Lieb lattice. The units are arbitrary in both cases, and the values should be compared only qualitatively.

state at band m or n to orbital α or β. To get the weights, we take the sum of the products of these localization coefficients, but only include the terms that correspond to those pairs of orbitals that can interact. As an example, for the Lieb lattice with nearest-neighbour interactions, $I_{AB} = 0$, since orbitals A and B are not nearest neighbours (see Fig. 2 for the orbital naming convention). The consequence of this is that all the weights for the flat band (weights where both m and n point to the flat band) are zero, because the flat band states are completely localized on orbitals A and B as per Eq. (3.12). Put another way, the localization coefficient of orbital C is zero for all $\boldsymbol{k}$. This reason of the weights being zero is essentially the same as why the intra-flat-band pairing vanishes in Eq. (3.9) (indeed, the right-hand sides of Eqs. (3.9) and (3.51) have a very similar structure).

Figure 4 shows both the DoS and the WDoP for the Lieb lattice. These curves are calculated numerically; the procedure will be detailed in Section 4. For now, let us compare the behaviour of the two quantities. For the most part, the curves look qualitatively similar. The major difference is that while the DoS diverges at the flat band (at zero energy), the WDoP instead goes to zero. This is, of course, why we defined the WDoP in the first place: it can take into account that while there is a large number of states at the flat band, they cannot form Cooper pairs with each other.

Next, we shall discuss some general properties of the weighted density of pairs. First, in systems with TRS we have $\epsilon_{\boldsymbol{k}m\uparrow} = \epsilon_{-\boldsymbol{k}m\downarrow}$ and $\mathcal{G}_{\boldsymbol{k}\uparrow} = \mathcal{G}^*_{-\boldsymbol{k}\downarrow}$, which means that instead of considering quasi-momenta $\boldsymbol{k}$ and $-\boldsymbol{k}$, we can focus on just $\boldsymbol{k}$ in Eq. (3.51). The double sum over the band indices m and n in Eq. (3.50) then collapses to a single summation everywhere except at band touching points, where we can have states at the same energy from different bands.

Second, if all orbitals can interact with each other, i.e. $I_{\alpha\beta} = 1$ for all α, β, we have $w_{\boldsymbol{k}mn} = 1$ for all $\boldsymbol{k}, m, n$ since the Bloch states are normalized. If we also have TRS, the WDoP reduces to essentially just the density of states (up to appropriate normalization).

For the Lieb lattice, this would be the case if we, on top of the nearest-neighbour interactions, added, for example, next-nearest-neighbour interactions, or alternatively on-site interactions as well as a link between the A and B orbitals. It is worth noticing that to achieve $I_{\alpha\alpha} = 1$ for some orbital α, we can have either on-site interactions, or an interaction between two α sites in different unit cells (or both). An example of a lattice with $I_{\alpha\beta} = 1$ for all α, β with just nearest-neighbour interactions is the π-flux square lattice, which we will encounter later in Section 5.

Third, if we have (at least) on-site interactions so that $I_{\alpha\alpha} = 1$ for all α, then in systems with TRS, $w_{\boldsymbol{k}mm}$ can never be zero. This is a consequence of the fact that the localization coefficients across orbitals must add up to unity, so at least one of them has to be non-zero (i.e. the particle has to be somewhere). Comparing the WDoP to the DoS, this means that for on-site interactions with TRS, the contribution of any quasi-momentum $\boldsymbol{k}$ cannot be completely "zeroed out" due to localization effects. In contrast, this is exactly what happens for all $\boldsymbol{k}$ on the flat band with the Lieb lattice with nearest-neighbour interactions. This makes sense, since with on-site interactions, wherever a particle is localized, it can always interact with its opposite quasi-momentum and spin counterpart at the same site.

4 Numerical Methods

We use multiple different lattice models to test the results of Sections 2-3 numerically. The details of the lattices will be presented in Section 5 alongside the corresponding results, but in this section, we go through details of the numerical implementation of the models.

4.1 Simulation of Lattices and Solving the Gap Equation

For a given lattice, we use a finite system with 50×50 unit cells with periodic boundary conditions, corresponding to 50×50 $\boldsymbol{k}$-points in the Brillouin zone. Determining the ground state of the system involves solving the gap equation of the interaction type in question, namely Eq. (2.34) (for RVB) or Eq. (2.37) (for on-site). This means solving the real-space order parameters $\Delta_{i\alpha j\beta}$ or Δ_α self-consistently so that the corresponding gap equation is satisfied. This is done through a fixed-point iteration scheme: namely, we start with a random guess for the order parameters, calculate the resulting BdG-Hamiltonian from Eq. (2.23), and diagonalize it numerically. The obtained eigenvalues and eigenvectors are fed into the right-hand side of the gap equation, and the resulting values are the new estimates for the order parameters. At this point we have a choice: what to use as the input for the next iteration? One approach is to simply use the output of the previous iteration. However, we find that this approach sometimes leads to oscillation so that the iteration never converges. Because of this, we use linear mixing, where the input of the next iteration is a combination of the input and the output of the last iteration. Concretely,

$$\Delta_{i+1} = (1-\gamma)\Delta_i + \gamma f(\Delta_i), \tag{4.1}$$

where Δ is a generic order parameter (one of the $\Delta_{i\alpha j\beta}$ or Δ_α), i is the iteration number, $f(\cdot)$ represents the gap equation, and $\gamma \in [0, 1]$ is a mixing parameter. When $\gamma = 1$ this corresponds to simply using the previous output as the new input. Decreasing γ helps avoid oscillation. We use $\gamma = 0.6$ in most cases. The iterations are carried out until convergence is reached, i.e. until we have such values of the order parameters that the left- and right-hand sides of the gap equation differ by at most a certain user-specified tolerance.

Fixed-point iteration is a ubiquitous method in computational fields, and we note that more sophisticated mixing methods, such as Pulay mixing (also known as the DIIS method) and its variants [52, 53], have been developed for accelerating convergence. For our purposes however, the simple linear mixing described above provides adequate computation times.

On the topic of computation times, we find that solving the gap equation for RVB interactions takes a significantly longer time than solving it in the on-site case, likely due to the added complexity from the $\boldsymbol{k}$-dependence of $\Delta_{\boldsymbol{k}}$, the off-diagonal block in the BdG-Hamiltonian. While the number of iterations required depends on multiple parameters, including the tolerance and the random initial guess, we find that for

on-site interactions this number typically ranges from a couple dozen to a hundred or two, while with RVB interactions a couple hundred iterations is the norm, and it is not uncommon to see the counter reach thousands. The Lieb lattice in particular behaves badly in this regard, with close to 10^4 iterations needed in some cases.

There are often multiple possible solutions to the gap equation, corresponding to different order parameter symmetries. These solutions have typically roughly the same magnitude, but they differ in how this total magnitude is divided between the orbitals (for on-site pairing) or the nearest-neighbour pairs (for RVB), and in the relative phases of the order parameters. The solutions to the gap equation are equivalently minima of the grand potential Ω, so the different solutions correspond to different local minima. To which of these minima the iteration converges is random due to the random initial guess, so we run the iteration for a few initial guesses, and pick the result with the lowest value of grand potential, obtained from Eq. (2.41), to be the global minimum. As a last step, we compare this lowest value of Ω to the case without pairing. If the latter value is smaller still, we output zeroes as the order parameter values.

4.2 Finite-size Effects

As mentioned above, we use a finite lattice with 50×50 unit cells in the simulations. This induces some finite-size effects to the numerical results, when they are compared to theoretical results that are derived in the thermodynamical limit of an infinite lattice. These effects are typically quite small, in absolute terms, but with our focus being on the transition points between normal and BCS states, even a small deviation in the order parameters is significant to the analysis, if the difference is between the order parameters being exactly zero or small, but non-zero. Regarding the QCPs, in Section 3.2 we demonstrated the importance of the density of states at the Fermi surface. We find that whether the order parameters below a predicted transition point come out to be exactly zero or not in the numerics depends on the size of the system. More precisely, it seems to depend on how close to the Fermi surface the closest $\boldsymbol{k}$-point in the discrete grid happens to be. Indeed, looking at Eqs. (3.27) and (3.42), if we were to replace the integrals with sums and even a single $\boldsymbol{k}$-point lands exactly on the Fermi surface, the whole sum diverges, and there is no QCP. In contrast, as shown in Section 3.2, in the thermodynamical limit a single diverging point is sometimes not enough if the density of states at the Fermi surface is zero.

The takeaway from this is that the accuracy of the numerical simulations has an inherent limit, and this should be kept in mind when drawing conclusions from the results. No significant meaning should be given to the difference of exactly zero versus, say, 10^{-4} in order parameter values. For example, on the Lieb lattice with RVB interactions and $\mu = 0$, a 50×50 grid gives small-but-nonzero order parameters for any non-zero interaction strength J, while (as shown in Section 5) a 51×51 grid yields exactly zero order parameters until $J \approx 4.16$. With our $\boldsymbol{k}$-point spacing, in the former case the energy at one $\boldsymbol{k}$-point lands exactly on the Fermi surface, while in the latter case this does not happen.

4.3 Calculation of the DoS and the WDoP

The main numerical concern in calculating the DoS (Eq. (3.49)) and the WDoP (Eq. (3.50)) is how to deal with Dirac delta functions. We take a very simplistic approach where the energy spectrum is split into bins of length 10^{-2}, and we then count how many states (for the DoS) or pairs (for the WDoP, with the appropriate weights included) land in each bin. For the DoS, this is thus just the histogram of energies. For the WDoP, this is a weighted histogram of pairs, where a pair is included in the count if the energies of the two states are less than 10^{-2} apart, and when that is the case, the average of their energies are used to determine the bin.

This method is roughly equivalent with replacing the delta functions with a constant "box" function f

$$\delta(x) \to f(x) = \begin{cases} 1 & |x| < \frac{10^{-2}}{2}, \\ 0 & \text{otherwise.} \end{cases} \tag{4.2}$$

This is a very crude approximation of the delta function. First of all, f doesn't integrate to unity: it should be multiplied by 10^2 to achieve that. We do not worry about this, since the units of the DoS and the WDoP are arbitrary, and we only care about their qualitative behaviour, and do not need to quantitatively compare the DoS to the WDoP. Second, f has a hard cut-off, i.e. a discontinuity, at $|x| = 10^{-2}/2$. Continuous alternatives include, for example, a Lorentzian

$$\delta(x) \approx \frac{1}{\pi} \frac{c}{c^2 + x^2} \tag{4.3}$$

for some small parameter $c > 0$. After some trials, it was deemed that such alternatives only increase the computation time (due to the larger range of non-zero values in the delta function), while providing no noticable improvements to the results. By improvements we mean simply visibly smoother DoS/WDoP curves; since we are only going to make qualitative arguments based on the curves (i.e. the values themselves are not used in any further calculations), this is enough for our purposes. Instead of choosing a better approximation for the delta function, we increase the size of the lattices to 500×500 for these calculations, which does visibly improve the results.

4.4 Numerical Brillouin Zone Integrals

In addition to direct simulations, we use the method developed in Section 3.2 to obtain some semi-analytical results. In particular, to get an estimate of the critical interaction strength J required for pairing using the uniform s-wave (for on-site interactions) or extended s-wave (for RVB) assumption, we wish to calculate the integrals in Eqs. (3.27) and (3.42) in the limit $\Delta \to 0$. The equations themselves are exact, but the integrals usually have to be evaluated numerically. This can be seen as equivalent to doing simulations on a finite lattice, but with specific numerical integration algorithms, the effective lattice size is much larger than the 50×50 used for the direct simulations.

Evaluating Brillouin zone integrals numerically is often difficult, because the integrands one is interested in often contain badly-behaving features, such as singularities and Dirac delta functions. This is a big enough problem in condensed matter physics that plenty of research has been done to develop methods specifically for these kind of integrals [54–58]. Our situation is no different: the integrands in Eqs. (3.27) and (3.42) have a spike near the Fermi surface, and this spike becomes increasingly narrow and pronounced as Δ becomes smaller, resulting in a singularity in the limit $\Delta \to 0$. Numerical integration methods have trouble calculating the values of such integrals, because the spike determines most of the integral's value, while accounting for a very small portion of the integration region.

With our previous discussion of finite-size effects in mind, we deal with this problem by simply not going all the way to $\Delta \to 0$, but instead use $\Delta = 10^{-2}$. Thus, the resulting values of J we get are strictly speaking not the critical values of J where Δ transitions from zero to non-zero, but the values where Δ reaches 10^{-2}. We take this as an acceptable compromise, because these results are compared to the direct simulations, and due to finite-size effects the results of the simulations are not accurate for very low values of Δ anyway. Setting $\Delta = 10^{-2}$ lets us use standard numerical integration methods; specifically, we use both SciPy's dblquad with Python and Mathematica's NIntegrate with default options. We find that with $\Delta = 10^{-2}$ these methods agree typically to 6-7 digits of precision, while deviations and increased error estimates start to occur were we to go an order of magnitude or two lower. This approximation means that we sligthly overestimate the critical values of J. Thus, our results still work well as upper bounds for the true values.

5 Computational Results

In this section, we are going to put the theoretical results from Sections 3.1-3.2 to the test. What follows are numerical results for the ground-state order parameters for various model systems, with emphasis on analysing the transitions from a normal to a BCS state. In particular, we will assess the utility of the weighted density of pairs, as well as results derived with the uniform s-wave and extended s-wave assumptions, in predicting whether a system has a QCP, and what is the value of the interaction strength when the transition occurs.

All of the systems we consider have TRS. As such, we will generally drop the spin indices of all quantities, with the understanding that quantities without the spin index will refer to the spin up case (e.g. $H_{\boldsymbol{k}} = H_{\boldsymbol{k}}^{\uparrow}$), while the corresponding spin down quantities can be obtained via transforming $\boldsymbol{k} \longrightarrow -\boldsymbol{k}$ and taking the appropriate complex conjugates as detailed in Section 2 (e.g., $(H_{-\boldsymbol{k}}^{\downarrow})^* = H_{\boldsymbol{k}}^{\uparrow}$). In addition, the temperature is set to zero for all the results that will be presented.

5.1 First Examples of Quantum Criticality

5.1.1 Lieb and π-Flux Square Lattices

We start our numerical exploration of RVB superconductivity with the Lieb and π-flux square lattices. As discussed in Section 3.1, the Lieb lattice is a three-orbital bipartite lattice, with sublattice sizes two and one. Thus, it has particle-hole symmetry and features a flat band at zero energy, i.e. at half-filling. The dispersions as well as the structure of the lattice are shown in Fig. 5. As shown in the figure, we use staggered hopping amplitudes with a parameter δ that varies between zero and one. When $\delta = 0$, the hopping amplitudes are uniform, and the two dispersive bands touch the flat band at Dirac points in the corners of the Brillouin zone. A non-zero δ opens a gap to the spectrum, and in the limit $\delta \longrightarrow 1$ the lattice becomes disconnected. To calculate the dispersion relations, we use Eq. (2.24) to get

$$H_{\boldsymbol{k},\text{Lieb}} = \begin{pmatrix} 0 & 0 & \overline{a}_{\boldsymbol{k}} \\ 0 & 0 & \overline{b}_{\boldsymbol{k}} \\ \overline{a}_{\boldsymbol{k}}^* & \overline{b}_{\boldsymbol{k}}^* & 0 \end{pmatrix}, \tag{5.1}$$

where $\overline{a}_{\boldsymbol{k}} = 2\cos\frac{k_x}{2} + i\delta\sin\frac{k_x}{2}$, $\overline{b}_{\boldsymbol{k}} = 2\cos\frac{k_y}{2} + i\delta\sin\frac{k_y}{2}$, and the overline is to make a distinction to the analogous values defined in Eq. (3.10). The lattice spacing here and henceforth is set to unity. Diagonalizing $H_{\boldsymbol{k},\text{Lieb}}$ gives the dispersion relations

$$\epsilon_{\boldsymbol{k}1,\text{Lieb}} = -2\sqrt{1+\delta^2+(1-\delta^2)(\cos k_x + \cos k_y)/2}, \tag{5.2}$$

$$\epsilon_{\boldsymbol{k}2,\text{Lieb}} = 0, \tag{5.3}$$

$$\epsilon_{\boldsymbol{k}3,\text{Lieb}} = 2\sqrt{1+\delta^2+(1-\delta^2)(\cos k_x + \cos k_y)/2}. \tag{5.4}$$

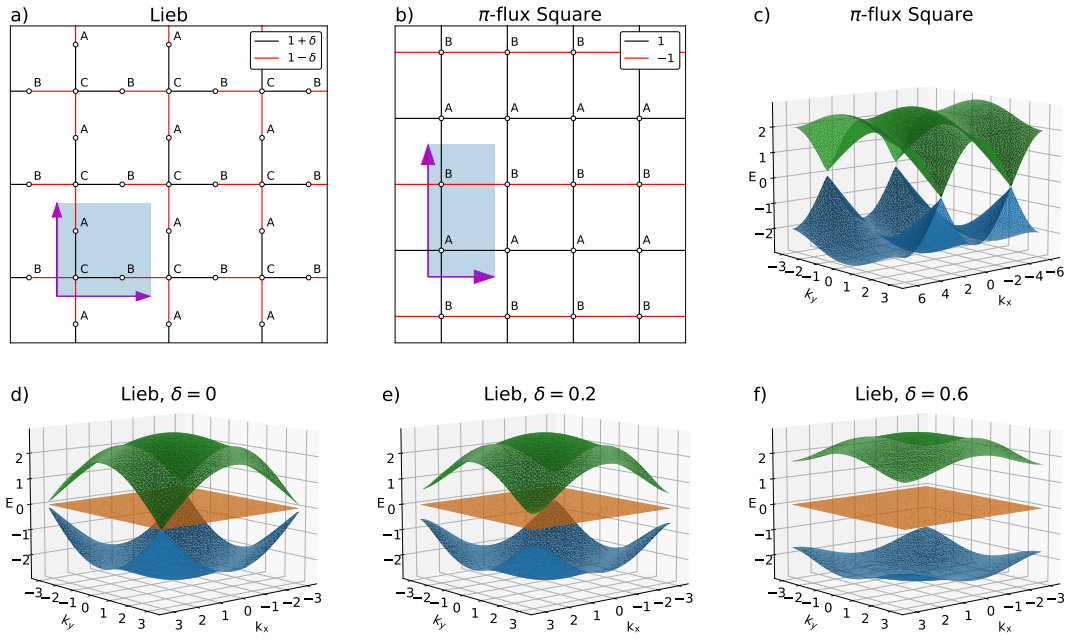

Figure 5: **(a-b)**: Lattice structures for the Lieb and π-flux square lattices. The dots indicate lattice sites, and the lines connecting them show the hoppings. Lines with different colors indicate different hopping amplitudes. The arrows depict the basis vectors of the lattices, and one unit cell is shown shaded. **(c-f)**: Single-particle dispersions for the lattices over the Brillouin zone; for the Lieb lattice, the dispersions are shown for three different values of the hopping staggering δ. For $\delta = 0$, the π-flux square lattice has the same dispersion as the Lieb lattice, save for the missing flat band, and with the Brillouin zone extended twice as long in the k_x-direction. For the Lieb lattice, a non-zero δ opens a gap of $2\sqrt{2}\delta$ between the bands.

For all values of $\delta \in [0, 1]$, the minimum energy of the higher dispersive band, as well as the maximum energy of lower dispersive band, occur at $\boldsymbol{k} = (\pm\pi, \pm\pi)^T$, yielding a band gap of $2\sqrt{2}\delta$.

As a reference point to the Lieb lattice, we use the π-flux square lattice. This is a simple square lattice where the magnitudes of the hopping amplitudes are uniform, but the phases are modified in such a way that a particle acquires a phase π while hopping around a square. We choose the gauge so that the hopping amplitudes are 1 along three sides of a given square, and -1 along the fourth side, as depicted in Fig. 5b. This structure gives the kinetic Hamiltonian

$$H_{\boldsymbol{k},\pi\text{-flux}} = 2\begin{pmatrix} \cos\frac{k_x}{2} & \cos\frac{k_y}{2} \\ \cos\frac{k_y}{2} & -\cos\frac{k_x}{2} \end{pmatrix}, \tag{5.5}$$

and the corresponding dispersion relations

$$\epsilon_{\boldsymbol{k}1,\pi\text{-flux}} = -2\sqrt{\cos^2\frac{k_x}{2} + \cos^2\frac{k_y}{2}}, \tag{5.6}$$

$$\epsilon_{\boldsymbol{k}2,\pi\text{-flux}} = 2\sqrt{\cos^2\frac{k_x}{2} + \cos^2\frac{k_y}{2}}. \tag{5.7}$$

The π-flux square lattice is useful for comparing with the Lieb lattice, since its two energy bands have the same dispersion relations as the dispersive bands of the Lieb lattice without staggering (to see this, set $\delta = 0$ in Eqs. (5.2) and (5.4), and use $\cos 2\theta = 2\cos^2\theta - 1$). Thus, the band structure is similar to the Lieb lattice; only the flat band is missing. In particular, it also features Dirac points where the two bands touch. Besides the missing flat band, the second difference is that the Brillouin zone is a $[-2\pi, 2\pi] \times [-\pi, \pi]$ rectangle, double the size of the usual $[-\pi, \pi] \times [-\pi, \pi]$ square Brillouin zone of the Lieb lattice, as can be seen in Fig. 5c.

We are now ready to discuss the results shown in Fig. 6. The figure shows the mean order parameter magnitudes as a function of the interaction strength J for the two lattices (for now, we set $\delta = 0$ for the Lieb lattice), with the Fermi surface set to the Dirac points ($\mu = 0$). In addition to RVB interactions, the results for on-site interactions are also shown for reference. In the RVB case, the resulting curves show a transition at $J \approx 4.2$; we see clear QCPs as both of the lattices transition from a normal (non-superconducting) to a BCS state. The small-but-nonzero order parameters before the transition point for the Lieb lattice are attributed to finite-size effects; see Section 4.2 for a more detailed discussion. On the other hand, with on-site interactions a QCP is present only for the π-flux square lattice, but not for the Lieb lattice.

To explain these QCPs, we turn to the results of sections 3.1 and 3.2. For the π-flux square lattice with $\mu = 0$, the Fermi surface is set to the Dirac points between the bands, where the density of states is zero. The vanishing DoS is also shown in Fig. 6c, and a zero DoS also means a zero WDoP. Thus, we interpret that for low interaction strengths, there are not enough available states near the Fermi surface for pairs to form. This holds for both RVB and on-site interactions. For the Lieb lattice

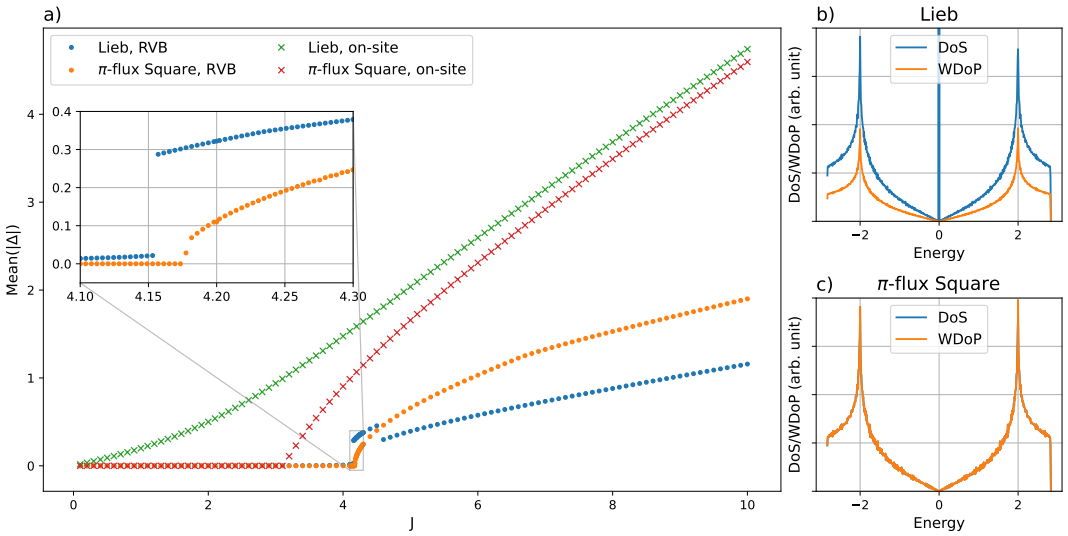

Figure 6: **(a)**: Average magnitude of the real-space order parameters ($|\Delta_{0\alpha j\beta}|$ for RVB, $|\Delta_\alpha|$ for on-site) for RVB and on-site interactions. Here, the hopping staggering δ is set to zero for the Lieb lattice, and the chemical potential μ is zero for both of the lattices. The π-flux square lattice shows a QCP for both types of interactions, while for the Lieb lattice a QCP exists only for RVB interactions. **(b-c)**: The densities of states (DoS) and the weighted densities of pairs (WDoP) for both of the lattices. For the π-flux square lattice, the curves are on top of each other. The units for both quantities are arbitrary, and their values should be compared only qualitatively. Note that while the DoS for the Lieb lattice diverges at zero energy, the WDoP instead goes to zero, resulting in the QCP in the RVB case.

however, looking at only the DoS, it would seem that there should be plenty of states available. The Fermi energy is precisely at the flat band, where the density of states diverges. This is where the nature of nearest-neighbour interactions and the structure of bipartite lattices comes into play: as shown in Section 3.1, in the RVB case particles at the flat band cannot form pairs with each other, because the flat band states are completely localized on the larger sublattice, which means that they are not nearest neighbours and cannot interact. As seen in Fig. 6b, this manifests itself in a vanishing WDoP at the flat band, even though the DoS diverges.

These results indicate that with intra-band pairing forbidden in the flat band, the Lieb lattice with RVB interactions behaves, regarding the QCP, *as if the flat band wasn't there* (this is not exactly true, since particles at the flat band can still form pairs with particles from the dispersive bands). This is in stark contrast to previous flat-band literature, where flat bands are generally predicted to enhance superconducting effects [14, 15, 42–46]. These results are often obtained for on-site interactions, and indeed we see in Fig. 6a that for the Lieb lattice, the QCP disappears with on-site interactions, and the order parameters are significantly larger than for the π-flux square lattice at low interaction strengths. This is now simple to explain: with on-site interactions, there are no more restrictions regarding intra-band pairing in

the flat band. Thus, suddenly the abundance of states at the Fermi energy are ready to form pairs. On the other hand, when changing from RVB to on-site interactions, for the π-flux square lattice the situation hasn't qualitatively changed: the DoS, and thus also the WDoP, at the Fermi surface are still zero, and we get a QCP at a finite interaction strength for both types of interactions.

Some quantitative comments of the results in Fig. 6a are in order. We find that with RVB interactions in particular, there are often multiple competing order parameter symmetries at given values of J, meaning multiple local minima of the grand potential. Which one of these is the global minimum depends on J, among other factors. This can induce discontinuities when looking at the mean order parameter magnitudes. One such discontinuity is visible in Fig. 6a for the Lieb lattice with RVB interactions around $J \approx 4.5$, when the optimal order parameter symmetry changes. Another such case happens for the π-flux square lattice with RVB interactions around $J \approx 6.5$, where there is a slight, but abrupt change in the derivative of the curve. The latter one is hardly visible in Fig. 6a, but we will see later that it indeed corresponds to a change in order parameter symmetry.

We also note the glaring result from Fig. 6a that with RVB interactions, for the Lieb lattice the order parameter magnitudes themselves have a discontinuity at the critical interaction strength, while for the π-flux square lattice only the derivative seems to be discontinuous. This, of course, implies that the phase transitions could be of different types, but we leave further analysis of the subject outside the scope of this thesis.

5.1.2 Kagome and Honeycomb Lattices

For a second pair of lattices we take a look at the kagome and honeycomb lattices. The lattice structures and the corresponding dispersions are shown in Fig. 7. Both of the lattices are hexagonal, and the kagome lattice has three orbitals, while the honeycomb lattice has two. For the kagome lattice, the kinetic Hamiltonian and the corresponding dispersion relations are

$$H_{\boldsymbol{k},\text{kagome}} = -2\begin{pmatrix} 0 & \cos\frac{k_1}{2} & \cos\frac{k_2}{2} \\ \cos\frac{k_1}{2} & 0 & \cos\frac{k_1-k_2}{2} \\ \cos\frac{k_2}{2} & \cos\frac{k_1-k_2}{2} & 0 \end{pmatrix}, \tag{5.8}$$

$$\epsilon_{\boldsymbol{k}1,\text{kagome}} = -1 - \sqrt{3 + 2\Lambda(\boldsymbol{k})}, \tag{5.9}$$

$$\epsilon_{\boldsymbol{k}2,\text{kagome}} = -1 + \sqrt{3 + 2\Lambda(\boldsymbol{k})}, \tag{5.10}$$

$$\epsilon_{\boldsymbol{k}3,\text{kagome}} = 2, \tag{5.11}$$

where $k_i = \boldsymbol{k} \cdot \boldsymbol{a}_i$ with $a_1 = (1, 0)^T$ and $a_2 = (1/2, \sqrt{3}/2)^T$ the basis vectors of the lattice, and $\Lambda(\boldsymbol{k}) = \cos k_1 + \cos k_2 + \cos(k_1 - k_2)$. For the honeycomb lattice, we have

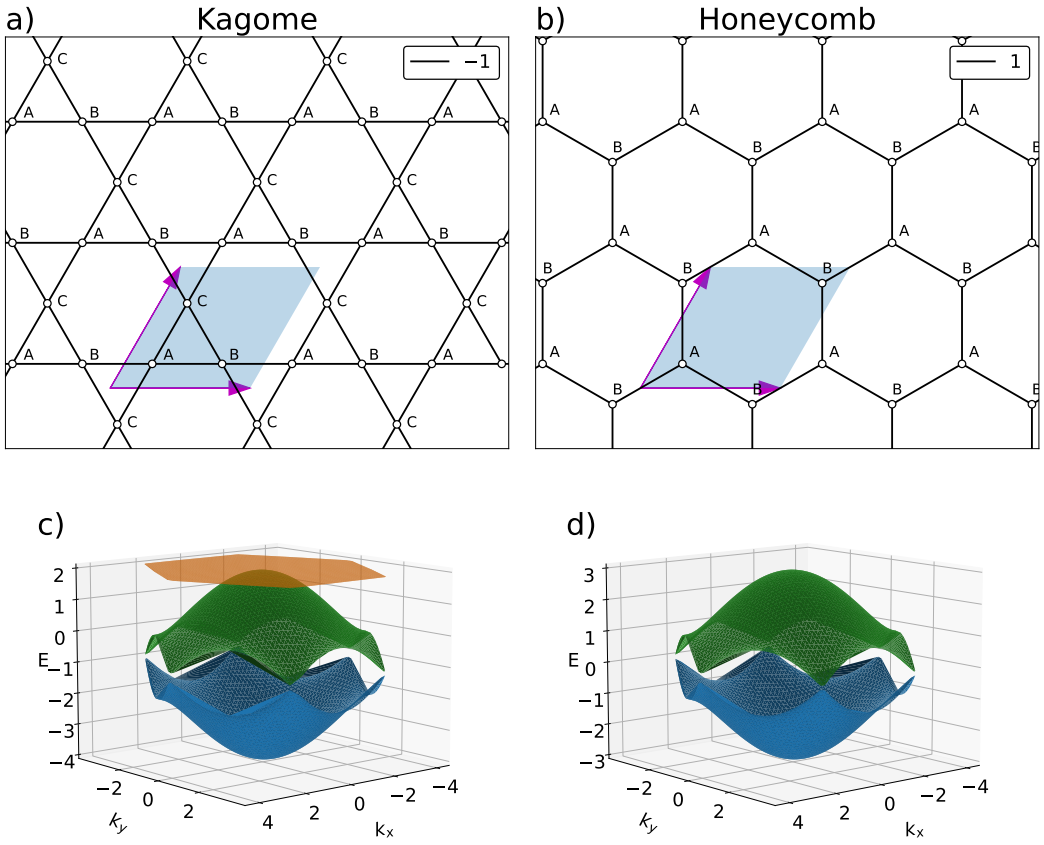

Figure 7: **(a-b)**: Lattice structures for the kagome and honeycomb lattices. The dots indicate lattice sites, and the lines connecting them show the hoppings. All of the hopping amplitudes are set to either -1 (for the kagome lattice) or $+1$ (for the honeycomb lattice). The arrows depict the basis vectors of the lattices, and one unit cell is shown shaded. **(c-d)**: Single-particle dispersions for the lattices over the Brillouin zone. The honeycomb lattice has, up to a constant shift of one energy unit, the same dispersion as the kagome lattice, apart from missing the flat band at the top of the kagome spectrum.

$$H_{\boldsymbol{k},\text{honeycomb}} = \begin{pmatrix} 0 & c_{\boldsymbol{k}} \\ c_{\boldsymbol{k}}^* & 0 \end{pmatrix}, \tag{5.12}$$

$$c_{\boldsymbol{k}} = e^{\frac{i}{3}(2k_1-k_2)} + e^{\frac{i}{3}(-k_1+2k_2)} + e^{\frac{i}{3}(-k_1-k_2)}, \tag{5.13}$$

$$\epsilon_{\boldsymbol{k}1,\text{honeycomb}} = -\sqrt{3+2\Lambda(\boldsymbol{k})}, \tag{5.14}$$

$$\epsilon_{\boldsymbol{k}2,\text{honeycomb}} = \sqrt{3+2\Lambda(\boldsymbol{k})}. \tag{5.15}$$

We selected these two lattices for a comparison, since, similarly to the Lieb and π-flux square lattices, they have very similar band structures. Indeed, apart from a constant shift of one energy unit, and an extra flat band in the kagome spectrum, they are identical. The kagome lattice is not bipartite, so its flat band is not a result of the mechanism explained in Section 3.1; hence, intra-band pairing is allowed also in the flat band. On the other hand, the honeycomb lattice is bipartite (refer to Fig. 7b; the A sites are only connected B sites, and vice versa), but its sublattices are of an equal size, so there is no flat band.

The kagome and honeycomb lattices have a few notable points in their spectra. First, the two dispersive bands touch at Dirac points in the corners of Brillouin zone at energy $\epsilon = -1$ ($\epsilon = 0$) for the kagome (honeycomb) lattice. Second, at energies $\epsilon = 0, -2$ ($\epsilon = \pm 1$), the spectra have van Hove singularities (vHSs) at the midpoints of the edges of the Brillouin zone, where the dispersion relation becomes flat and the density of states diverges. Finally, the upper dispersive band of the kagome lattice touches the flat band at a quadratic band touching point (QBTP) in the middle of the Brillouin zone at energy $\epsilon = 2$; for the honeycomb lattice the corresponding point is simply the top of the upper dispersive band at $\epsilon = 3$.

Next, we will take a look at how the order parameters behave as a function of interaction strength when the chemical potential is, in turn, set to each of these special points of the spectra. The results are shown in Fig. 8; in addition to RVB interactions, we have again included results also for on-site interactions for reference. First, a comment about the outliers and discontinuities in the order parameter curves. The outliers (when the order parameter magnitude for some J is distinctly different from the values around it) are local, but non-global, minima of the grand potential with competing order parameter symmetries. As discussed in Section 4, we run the semi-random process of solving the gap equation multiple times to find the global minimum, but for RVB interactions the values of Ω at the different local minima are often very close to each other, and sometimes the global minimum is not found despite multiple attempts. On the other hand, discontinuities such as those in Fig. 8e at $J \approx 5.3$ for the kagome lattice, and at $J \approx 7.4$ for the honeycomb lattice with RVB interactions signify points where the order parameter symmetry of the ground state does in fact change.

We turn now to the main results of Fig. 8, that is, the existence or absence of a QCP at a non-zero interaction strength. Most of these QCPs, or absences thereof, are explained by our preceding discussion in the previous section and in Section 3.2. First, at the Dirac point, both lattices show a QCP for both interaction types; similarly to the

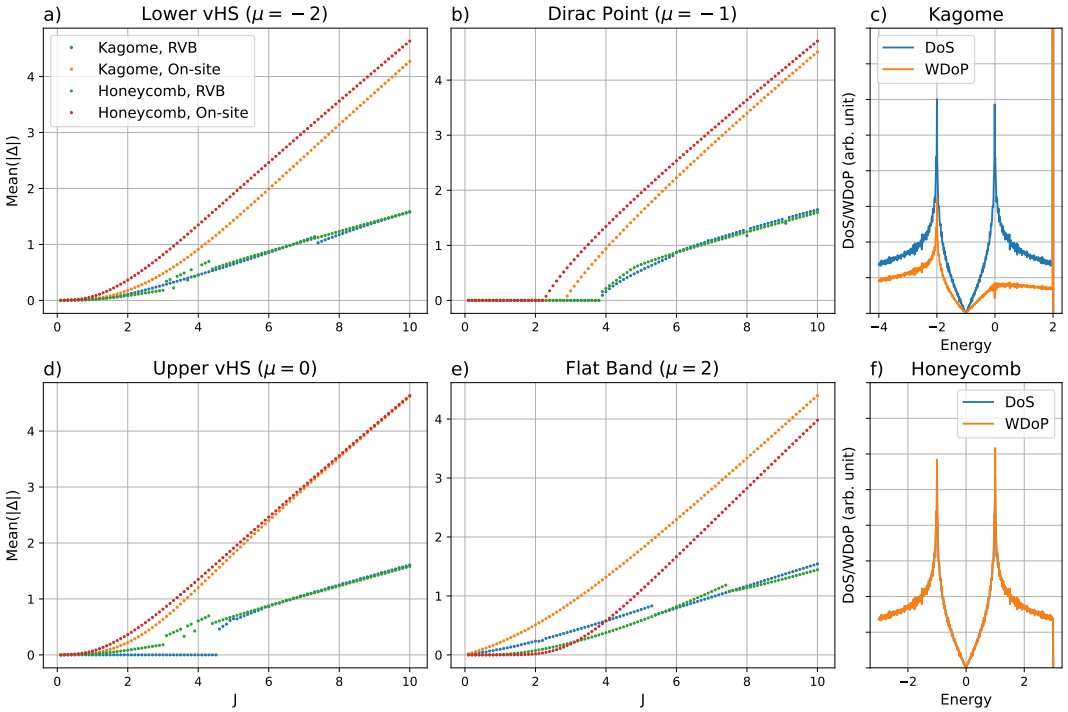

Figure 8: **(a-b)**, **(d-e)**: Average magnitude of the real-space order parameters ($|\Delta_{0\alpha j\beta}|$ for RVB, $|\Delta_\alpha|$ for on-site) for RVB and on-site interactions for the kagome and honeycomb lattices, with the chemical potential set, in turn, to both of the van Hove singularities, the Dirac point, and the flat band (top of the spectrum for the honeycomb lattice). The values of the chemical potential μ in the figures correspond to the kagome lattice; the values for the honeycomb lattice are this value plus one. At the Dirac point, a QCP emerges for both of the lattices and both interactions types, while at the upper vHS only the kagome lattice with RVB interactions yields a QCP. **(c)**, **(f)**: The densities of states (DoS) and the weighted densities of pairs (WDoP) for both of the lattices. For the honeycomb lattice the curves are on top of each other. The units for both quantities are abitrary, and the values should be compared only qualitatively. Notably, for the kagome lattice the DoS diverges at the upper vHS, while the WDoP does not, which explains the QCP with RVB interactions.

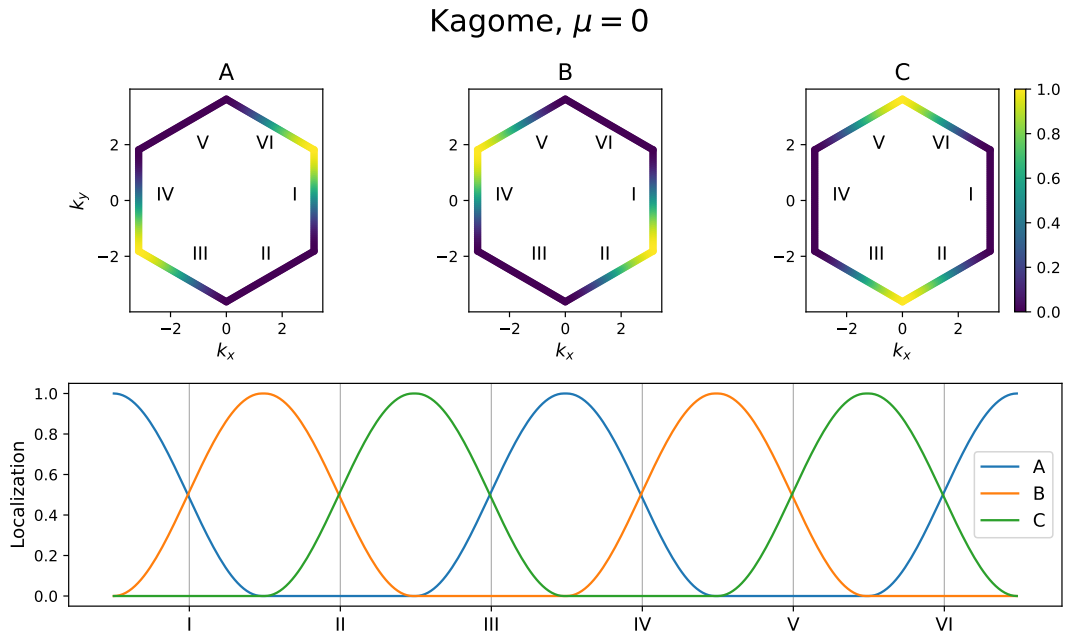

Figure 9: Upper row: the localization coefficients of orbitals A, B and C (see Fig. 7a for the naming convention), respectively, along the Fermi surface of the kagome lattice, with the chemical potential $\mu = 0$ set to the upper van Hove singularity (vHS). The vHSs occur at the corners of the Fermi surface. **Lower row**: the same information combined to a single graph. At the vHSs, the states are completely localized to a single orbital.

π-flux square lattice and the simplified models in Section 3.2, this is explained by the vanishing density of states.

Second, when the Fermi energy is at the flat band (for the kagome lattice), or on top of the upper dispersive band (for the honeycomb lattice), there are no QCPs; instead, any finite interaction strength yields non-zero order parameters, i.e. a BCS state (though the order parameters for the honeycomb lattice are very small for weak interactions). This is natural, since in these cases there are plenty of states available at the Fermi surface for pairing to occur, as seen in the DoS and WDoP graphs of Fig. 8. As mentioned before, here intra-band pairing in the flat band is possible, since, contrary to the Lieb lattice, the flat band states of the kagome lattice are not localized on non-neighboring sites. Indeed, with the Fermi surface on the flat band, the order parameters are noticably larger than those of the honeycomb lattice, which is missing the flat band. The effect is especially clear at low interaction strengths.

Third, for the lower vHS we also get a BCS state for any finite interaction strength for both lattices and interaction types, explained by the large density of states and WDoP.

The peculiar case is what happens when the chemical potential is set to the upper van Hove singularity. For both of the lattices, the dispersion near this point is a mirror image of the lower vHS, so one could expect the weak-interactions behaviour to be the same. This is indeed (qualitatively) the case for both of the lattices with on-site

interactions, and for the honeycomb lattice also with RVB interactions. However, the kagome lattice with RVB interactions has a QCP; a considerably large interaction strength J is needed before pairing occurs. With the large density of states at the vHS, why is this the case? Comparing the DoS of the kagome lattice to its WDoP in Fig. 8c yields the answer: while the former diverges at zero energy, the latter does not. There must thus be something unusual about the localization properties of the states at the upper vHS, and indeed there is, as noted previously by the authors in Refs. [59, 60]. Figure 9 shows the localization coefficients, i.e. $|[\mathcal{G}_{\boldsymbol{k}}]_{\alpha,m}|^2$, the absolute values squared of the elements of the Bloch state vectors, along the Fermi surface when the chemical potential is set to the upper vHS. The Fermi surface here is a hexagon, and each of the corners of this hexagon has a vHS. In each of the vHSs, the states are completely localized to a single orbital, A, B or C (refer to Fig. 7a for the labeling of the orbitals). Moreover, as dictated by TRS, the states at $\pm\boldsymbol{k}$, i.e. on the opposite sides of the hexagon, are localized to the same orbital. In our singlet-pairing model, Cooper pairs form between particles with quasi-momenta $\boldsymbol{k}$ and $-\boldsymbol{k}$, so the particles at the vHSs cannot form pairs, since any A site is not a neighbour of any other A site in the kagome lattice, and similarly for B and C. We note that similar behaviour, where the states at the vHSs are completely localized on a single orbital, does not occur at the lower vHS in the kagome lattice, or at either of the vHSs in the honeycomb lattice; hence QCPs do not appear in these cases.

This explains why there is a QCP on the kagome lattice with RVB interactions: the large density of states at the upper van Hove singularities does not help, since the particles at these states are unable to form pairs with each other. The reason is thus similar to the Lieb lattice: we have a large density of states, but the localization properties of these states forbid pairing. With the Lieb lattice, this holds all across the flat band due to the bipartiteness of the lattice, which is reflected by the vanishing WDoP. For the kagome lattice the situation is more subtle. Instead of pairing being forbidden throughout the Fermi surface, it is only forbidden at the vHSs. However, the vHSs contribute the most to the density of states at this energy, and "removing" just them seems to be enough to lower the WDoP substantially so that a QCP emerges.

It should be noted that, as seen in Fig. 8, the critical interaction strength for the kagome lattice is higher at the upper vHS than at the Dirac point. However, the WDoP is zero in the latter case, but non-zero in the former. The WDoP therefore does not necessarily offer predictions about where the transition point is; its usefulness comes mainly from comparisons to the DoS. If the behaviour of the WDoP looks significantly different from the DoS, one can expect that there is something unusual with the localization properties of the Bloch states and investigate them further, as we did in Fig. 9. In general, deviations between the WDoP and DoS imply that there are states that are at least partially localized on non-neighboring states. In itself, this does not necessarily mean that there has to be a QCP, but as we have seen with the Lieb and kagome lattices, when this kind of localization that prevents pairing coincides with a large density of states, the consequences can be significant.

5.2 Predicting the Transition Point

So far we have seen a few examples of QCPs caused by the non-availability of states in the vicinity of the Fermi surface. This could be due to just a low DoS, or, as demonstrated with the Lieb and kagome lattices with RVB interactions, due to localization effects preventing pairing in spite of a large DoS; in the latter case we instead saw a suppressed WDoP. This analysis offers a physical explanation of when we should expect there to be a QCP, but so far we have not quantitatively discussed where the transition point occurs. That is, what is the critical value for the interaction strength J when a given system transitions from a normal to a BCS state? As seen above, the WDoP is not an ideal metric for making this prediction. Instead, we will use a method based on the results of Sections 3.2.1 and 3.2.2. In particular, we will calculate an upper bound for the transition point based on a specific assumption about the order parameter symmetry, and compare those results to the simulations to see (1) how close the upper bound is to the real transition point, and (2) whether the simulated ground state actually has the assumed order parameter symmetry.

First, we revisit the results for the Lieb and π-flux square lattices. With RVB interactions, $\mu = 0$ and the hopping staggering $\delta = 0$ for the Lieb lattice, using the extended s-wave assumption of Section 3.2.2 predicts the QCP to be at $J \approx 4.18$ for both of the lattices via Eq. (3.45). In more detail, for the Lieb lattice the prediction is $2C_{\text{Lieb}}/S_{\text{Lieb}}$, where, recalling that $C = \sum_{j\alpha\beta} |t_{0\alpha j\beta}|^2$, we have $C_{\text{Lieb}} = 8$ since $t_{0\alpha j\beta} = 1$ for all $\boldsymbol{j}, \alpha, \beta$, and there are two edges starting from both of the orbitals A and B and four edges starting from orbital C (see Fig. 5a). Note that this is essientally a double count of the distinct hopping amplitudes. Furthermore, we have

$$S_{\text{Lieb}} = 2 \cdot \frac{1}{4\pi^2} \int_{-\pi}^{\pi} \int_{-\pi}^{\pi} 2\sqrt{\cos^2 \frac{k_x}{2} + \cos^2 \frac{k_y}{2}} \, \mathrm{d}k_x \, \mathrm{d}k_y \approx 3.83, \tag{5.16}$$

while for the π-flux square lattice we have also $C_{\pi\text{-flux}} = 8$ and

$$S_{\pi\text{-flux}} = 2 \cdot \frac{1}{8\pi^2} \int_{-\pi}^{\pi} \int_{-2\pi}^{2\pi} 2\sqrt{\cos^2 \frac{k_x}{2} + \cos^2 \frac{k_y}{2}} \, \mathrm{d}k_x \, \mathrm{d}k_y = S_{\text{Lieb}}. \tag{5.17}$$

The latter equality is due to the identical dispersion relations (apart from the extra flat band in the Lieb lattice, which doesn't contribute since it is at zero energy), with the effect of the larger Brillouin zone of π-flux square lattice canceling out, as the integrand is 2π-periodic in k_x and we divide by the area of the Brillouin zone. Looking at Fig. 6a, with the simulations we obtain transition points at $J \approx 4.16$ and $J \approx 4.18$ for the Lieb and π-flux square lattices, respectively. For the latter case the prediction is pretty much exact, and it is also very close for the Lieb lattice.

The pairing symmetry the ground state of a system features depends on at least the lattice, the interaction strength and the chemical potential. What we find in this case is that for the π-flux square lattice the ground state does have the extended s-wave symmetry at the transition point, while the Lieb lattice does not. It thus makes sense that the prediction for the π-flux square lattice matches numerical results, but it is not

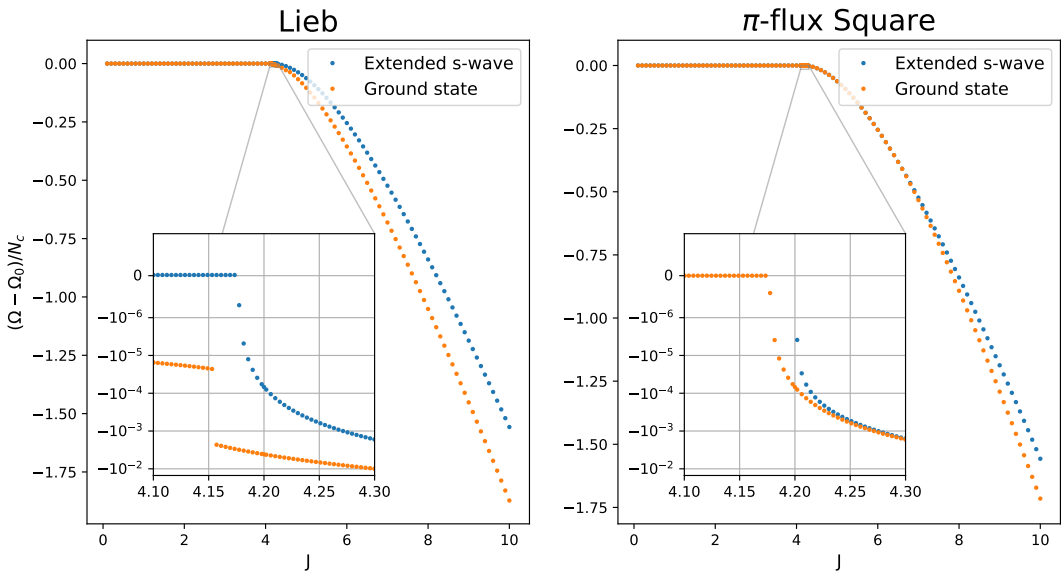

Figure 10: The value of the grand potential Ω (per unit cell) relative to Ω_0, the value without pairing, as a function of the interaction strength J for the real ground state, and with the extended s-wave assumption. The chemical potential μ is set to zero for both of the lattices, and also the staggering δ is zero for the Lieb lattice. The constant values of Ω before the BCS transition at $J \approx 4.18$ correspond to the normal state, i.e. the minimum of Ω occurs with no pairing. The insets are zoomed in near the transition point; note the logarithmic scale. For the π-flux square lattice, the extended s-wave solution is the real solution from the transition point to around $J \approx 6.5$. For the Lieb lattice the extended s-wave solution is not the ground state for any value of J, but it gives a very close prediction to where the QCP is. For the Lieb lattice, the small discrepancy between the ground state values of Ω and Ω_0 below the critical interaction strength is a finite-size artefact, corresponding to the small-but-nonzero order parameter values before the QCP in Fig. 6a.

immediately obvious why this should be the case for the Lieb lattice. The situation is clarified in Fig. 10 where we show the values of the grand potential Ω as a function of interaction strength for both the real ground state and the extended s-wave solution. What we find is that even though the extended s-wave solution is not the actual ground state for the Lieb lattice, i.e. it does not minimize Ω, the transitions from a normal to a BCS state, at least in this case, occur at almost the same time. We note that the small discrepancy in the predicted value $J \approx 4.18$ and our numerical result $J \approx 4.16$ could be due to finite-size effects, but it could just as well be a real difference between the two solutions.

Next, we turn again to the kagome and honeycomb lattices, where we have a larger collection of QCPs to predict in Fig. 8. By assuming uniform s-wave pairing (for on-site interactions) or extended s-wave pairing (for RVB), we can get an upper bound for the critical interaction strength from Eqs. (3.27) and (3.42), respectively. Before, with the special case of RVB interactions with $\mu = 0$ we had access to the

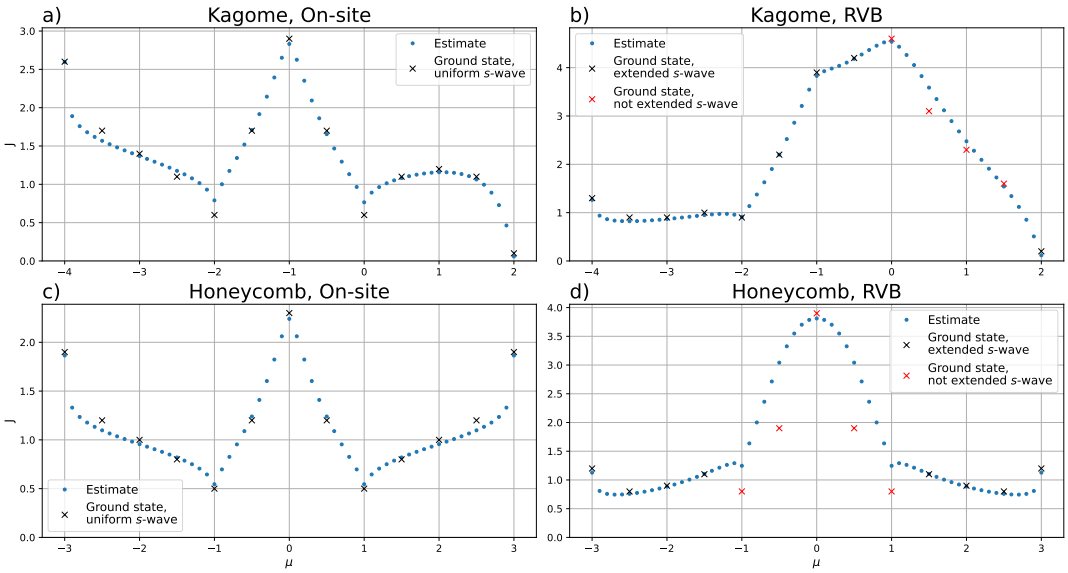

Figure 11: Minimum interaction strength J required for an average order parameter magnitude of 10^{-2} as a function of the chemical potential μ. The upper-bound estimates (the blue dots) are obtained by assuming uniform s-wave pairing (for on-site interactions, (**a**) and (**c**)), or extended s-wave pairing (for RVB, (**b**) and (**d**)). The real ground states (the crosses) are obtained by numerically solving the gap equation without pairing symmetry assumptions. The color of the crosses indicates whether the real ground state has the pairing symmetry of the estimate. See the main text for discussion of the discrepancies of the estimates and ground state results.

exact transition point from Eq. (3.45), but in general we have to resort to the two formerly-mentioned equations. Due to finite-size effects and numerical stability, we use the small-but-finite value $\Delta = 10^{-2}$ as a proxy for the transition point; see Section 4 for more discussion of the numerics. In particular, in each case we set $\Delta = 10^{-2}$ in the equations (while taking into account that in Eq. (3.42) Δ is defined as the ratio $\Delta_{0\alpha j\beta}/t_{0\alpha j\beta}$), perform the integrals numerically, and solve for J. This value can then be compared to the interaction strength where the average order parameter magnitude becomes larger than 10^{-2} with the actual, simulated ground state. This comparison is shown in Fig. 11 as a function of the chemical potential μ. We also indicate for which values of μ the ground state near the transition point satisfies the corresponding pairing symmetry assumption (uniform s-wave or extended s-wave). It should be noted that due to the finite threshold used for Δ, the corresponding minimum interaction strengths here are larger than zero even in cases where there is no QCP.

As a first observation, Fig. 11 retells the story from Fig. 8: for both lattices and interaction types, setting the Fermi surface to the Dirac point ($\mu = -1/0$ for kagome, honeycomb respectively) results in a large value for the threshold interaction strength, while in all cases, the lower van Hove singularity ($\mu = -2/-1$) yields the opposite result. With the upper vHS ($\mu = 0/1$), the kagome lattice with RVB interactions is the odd one out due to its Bloch state localization properties, as described in the previous

section.

The main message of Fig. 11 is that most of the time, the upper bound given by the simplifying pairing symmetry assumption also predicts quite well when the real transition happens. We find that with on-site interactions, the ground state of both of the lattices has uniform s-wave symmetry near the transition point for all values of μ covered. It is thus to be expected that Eq. (3.27) should give the same values for the order parameters as we get by directly solving the gap equation. The minor discrepancies in these cases are explained by finite-size effects, since in Eq. (3.27) we work in the thermodynamical limit, while the simulations involve a finite-sized lattice. With RVB interactions, there are also large ranges of μ for both of the lattices where the ground state solution matches the assumed pairing symmetry, i.e. extended s-wave, and in these cases the order parameters obtained by the two methods are again in close agreement. However, with RVB there are also some values of μ where the assumed pairing symmetry is not correct. When this happens, the extended s-wave prediction is sometimes (such as when $\mu = 0$ for either of the lattices) very close to the correct value, as was the case earlier with the Lieb lattice. At other times (such as with $\mu = \pm\frac{1}{2}$ or $\mu = \pm 1$ for the honeycomb lattice, or with $\mu = \frac{1}{2}$ for the kagome lattice), the prediction does not perform as well. Additional insight is offered in Fig. 12, where we show how the minimum of the grand potential Ω evolves as a function of J for both the extended s-wave and real ground state solutions. In this figure, we have picked data from the cases where the ground state does not coincide with the extended s-wave solution. We observe that for $\mu = 0$, for both of the lattices the QCP indeed occurs at the same time for both of the solutions, i.e. we are able to correctly predict the location of the transition point by assuming the extended s-wave solution, even though the assumption ends up being incorrect. On the other hand, for other values of μ the real critical point occurs at a lower value of J than predicted, which means that there is a range of J where a BCS state is possible even though a solution with the extended s-wave symmetry does not exist. This is most notably the case for the honeycomb lattice with $\mu = 0.5$, shown in Fig. 12e, where the discrepancy between the real transition point and the extended s-wave prediction is quite significant, explaining the corresponding large discrepancy in Fig. 11d.

5.3 Effects of Band Touching Points and Band Gaps

In this section, we return to the Lieb lattice with RVB interactions. So far we have only considered the Lieb lattice with $\mu = 0$, i.e. with the Fermi surface set to the flat band, and with the hopping staggering $\delta = 0$, i.e. with Dirac points in the corners of the Brillouin zone. Earlier, the conclusion was that the Lieb lattice with RVB interactions has a QCP when $\mu = 0$ because localization effects prevent the flat band from contributing to pairing, and thus the WDoP at the flat band is zero. There are several factors we can modify to change this situation. First, we can change μ, which should give us a non-zero WDoP to possibly help with pairing. Second, we can change δ to impose a band gap to the spectrum; here, we should expect there to be a QCP at least while the Fermi energy is located in the gap, since both the DoS and the WDoP are zero. Finally, using a method described in Ref. [61] we can tune the dispersion

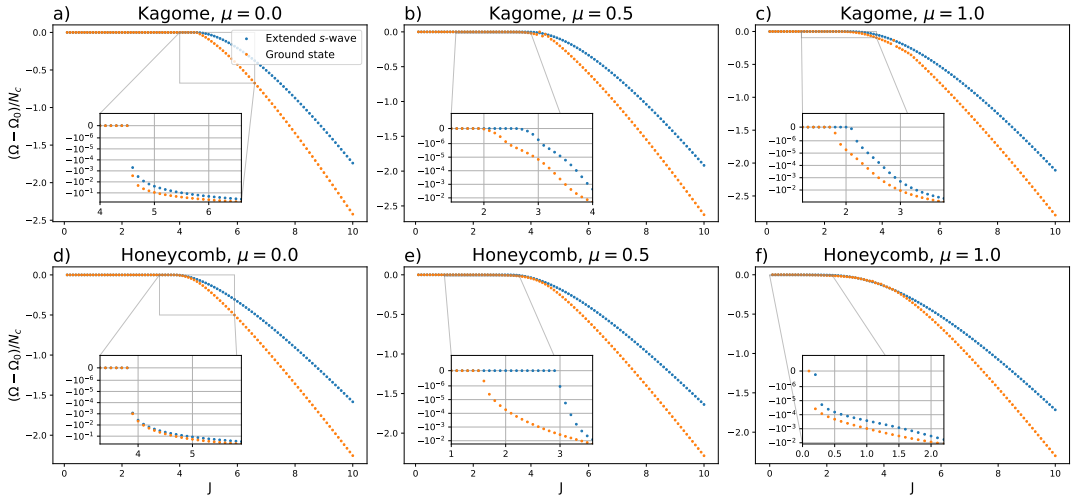

Figure 12: The values of the grand potential Ω relative to Ω_0, the value without pairing, for the extended s-wave and the real ground state solutions; a value of zero indicates no pairing. The insets are zoomed in near the QCPs; notice the log-scale. The cases shown here correspond to some of the red crosses in Fig. 11, i.e. the extended s-wave solution is not the real ground state near the transition point.

near the band touching point from linear (a Dirac point) to quadratic. This should make the contribution of the dispersive bands to the DoS non-zero at the BTP, so the WDoP should be non-zero as well even if the flat band still does not participate. The details of this method are presented later; for now, we focus on the first two points.

In Fig. 13 we show the average order parameter magnitudes as a function of both J and μ for the cases $\delta \in \{0, 0.2, 0.6\}$. Recall that the corresponding band gap is $2\sqrt{2}\delta$, which is clearly visible from the DoS and WDoP graphs that are also shown in the figure (see also the visualizations of the dispersion relations in Fig. 5). We have also used the extended s-wave assumption and Eq. (3.42) to come up with an upper-bound estimate of where the QCP is in each case (strictly speaking, we calculate the value of J needed for an order parameter magnitude of 10^{-2}, similarly to what was done with the kagome and honeycomb lattices). These estimates are shown alongside the simulated results in Fig. 13.

Let us start unpacking these results by looking at the case $\delta = 0$ (Figs. 13a and 13d). The curve for $\mu = 0$ is the same one we saw in Fig. 6a, but now we have data for more values of μ alongside it. As hypothesized above, what we find is that $\mu = 0$, i.e. setting the Fermi energy to the flat band, is actually the worst option with RVB interactions in the sense that the critical interaction strength for the BCS transition there is the highest. As μ is increased and the Fermi surface moves to the dispersive band, the WDoP starts to increase, and correspondingly the QCP moves to a lower value of J. The strongest pairing with weak interactions is achieved around $\mu = 2$, where the WDoP peaks. The real transition points also closely follow the estimates obtained with the extended s-wave assumption.

A non-zero staggering δ opens a band gap in the system, and as seen in Figs. 13e-f,

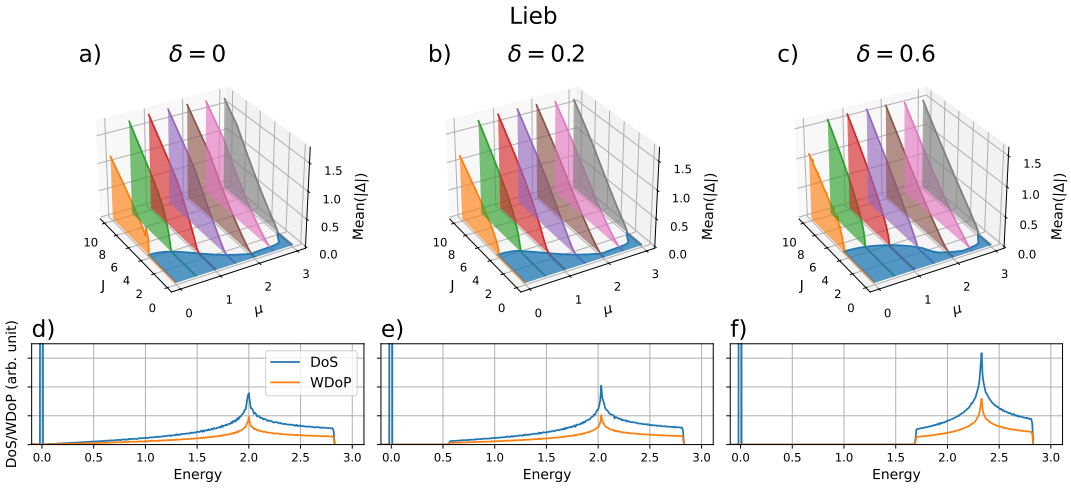

Figure 13: Upper row (a-c): Average real-space order parameter magnitude as a function of the interaction strength J and the chemical potential μ for the Lieb lattice, with RVB interactions, and with three different hopping staggerings, $\delta \in \{0, 0.2, 0.6\}$. The blue shade at the bottom shows estimates (upper bounds) for the transition point obtained with the extended s-wave assumption; the real transition points largely follow the estimates. **Lower row (d-f)**: The corresponding densities of states (DoS) and weighted densities of pairs (WDoP). The units for both quantities are arbitrary, and their values should be compared only qualitatively. Note the singularities in the DoS at zero energy, and the absence of those singularities in the WDoP. Due to particle-hole symmetry, only non-negative values of μ are shown.

it also shifts the maxima of the DoS and the WDoP to a higher energy. Compared to the case with $\delta = 0$, Figs. 13b-c reflect these changes: the "best" value of μ is increased with the peak in WDoP, while the critical interaction strength increases for those values of μ that now are in a band gap. These results thus reinforce the notion of the importance of the WDoP at the Fermi surface. We note, though, that in this case the WDoP and the DoS have qualitatively similar behaviour everywhere but at the flat band, so the effects of changing δ can mostly be inferred from the DoS alone. We also note that once again, the extended s-wave assumption is able to capture the changes in the system and yields quite good predictions of where the transition happens.

As promised in the beginning of this section, for our final point of analysis we investigate what happens with the Lieb lattice (with $\delta = 0$) if we tune the band-touching points from linear Dirac points to quadratic. For this, we need to change the lattice structure according to the method developed in Ref. [61]. The important property of this transformation is that it doesn't affect the Bloch states of the flat band nor its dispersion. This point is crucial for our purposes, since it allows us to keep the flat band states localized on non-neighboring states. This way, we can change the BTP from linear to quadratic while still keeping intra-flat-band pairing forbidden. For the Lieb lattice, this transformation was done in Ref. [44]. The resulting quadratic lattice is depicted in Fig. 14, which yields the kinetic Hamiltonian

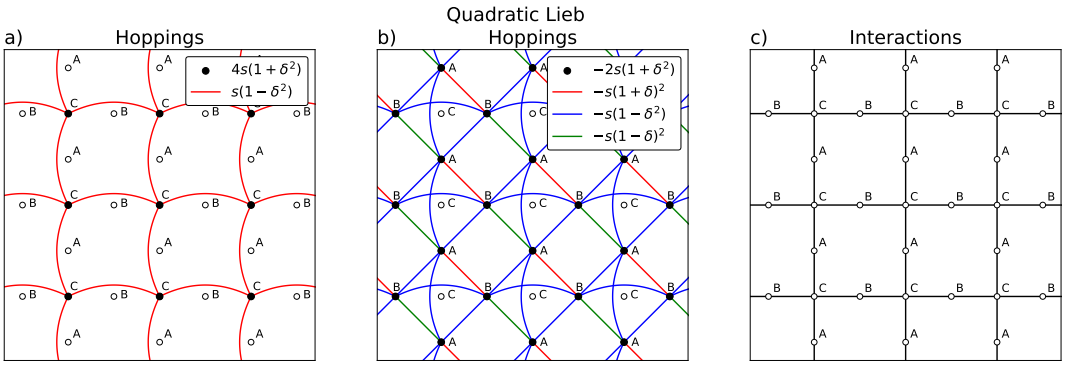

Figure 14: The structure of the quadratic Lieb lattice. In terms of hoppings, the lattice is split into two disconnected parts, the first sublattice consisting of orbital C (**a**), and the second one of orbitals A and B (**b**). The hopping amplitudes are given in terms of the constant $s = 1/(2\sqrt{2})$. To keep the flat band states not being able to interact with each other, interaction still occurs between the original nearest-neighbour pairs (**c**), although this makes the model highly unrealistic; see the main text for more discussion.

$$H^{\text{quad}}_{\boldsymbol{k},\text{Lieb}} = -\frac{1}{\sqrt{2}}\begin{pmatrix} \nu+\eta\cos k_y & \chi(\boldsymbol{k},\delta)^* & 0 \\ \chi(\boldsymbol{k},\delta) & \nu+\eta\cos k_x & 0 \\ 0 & 0 & -2\nu-\eta(\cos k_x+\cos k_y) \end{pmatrix}, \tag{5.18}$$

where $\nu = 1+\delta^2, \eta = 1-\delta^2$, and $\chi(\boldsymbol{k},\delta) = 2(\cos\frac{k_x}{2} - i\delta\sin\frac{k_x}{2})(\cos\frac{k_y}{2} + i\delta\sin\frac{k_y}{2})$. The corresponding dispersion relations are

$$\epsilon^{\text{quad}}_{\boldsymbol{k}1,\text{Lieb}} = -\sqrt{2}(1+\delta^2) - \frac{1}{\sqrt{2}}(1-\delta^2)(\cos k_x + \cos k_y), \tag{5.19}$$

$$\epsilon^{\text{quad}}_{\boldsymbol{k}2,\text{Lieb}} = 0, \tag{5.20}$$

$$\epsilon^{\text{quad}}_{\boldsymbol{k}3,\text{Lieb}} = \sqrt{2}(1+\delta^2) + \frac{1}{\sqrt{2}}(1-\delta^2)(\cos k_x + \cos k_y). \tag{5.21}$$

The above equations are given with the hopping staggering δ included, but we will only focus on the case $\delta = 0$ here. We note, first, that the flat band at zero is unaffected and, second, that the BTPs are now quadratic, as cosine behaves quadratically near its minimum. In this procedure, we have altered the structure of the lattice significantly: the two sublattices have become disconnected in the sense that particles cannot hop between them. However, as discussed above, the flat band states are still localized on orbitals A and B, so to keep intra-flat-band pairing forbidden, we must not alter the interaction pairs. Consequently, in this model hopping and interactions occur between different sets of pairs. For clarity, the interacting pairs are marked separately in Fig. 14c.

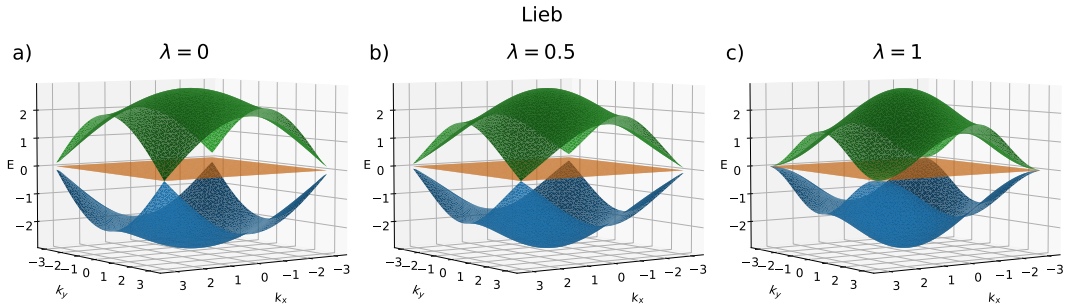

Figure 15: Dispersion relations for regular, linear Lieb lattice (**a**), the quadratic lattice (**c**), and a mix between the two (**b**). Here, the staggering δ is set to zero. While moving from the linear to the quadratic lattice, the band-touching points continuously change from linear to quadratic.

It must be emphasized that this division of the hopping and interacting pairs is highly unrealistic, as the physical origin of the RVB pairing is in the virtual hopping processes in the strong-repulsion limit of the Hubbard model, as discussed in Section 1. It thus makes little sense, physically speaking, to have an interaction between lattice sites between which hopping cannot occur. Nevertheless, we shall proceed with this model for the moment as a curiosity, because it has desirable mathematical properties, namely it allows for tuning the BTP from linear to quadratic without including the flat band to the pairing.

Having defined the quadratic lattice, we can shift continuously between it and the regular Lieb lattice with Dirac points by introducing the mixing parameter λ, and defining

$$H^{\text{mixed}}_{\boldsymbol{k},\text{Lieb}} = D_\lambda \Big((1-\lambda) H^{\text{linear}}_{\boldsymbol{k},\text{Lieb}} + \lambda H^{\text{quad}}_{\boldsymbol{k},\text{Lieb}} \Big), \tag{5.22}$$

where $H^{\text{linear}}_{\boldsymbol{k},\text{Lieb}}$ is the kinetic Hamiltonian of the regular Lieb lattice, and D_λ is a constant chosen such that the bandwidth of the dispersive bands always remains equal to the bandwidth of the dispersive bands of the regular linear lattice (which happens to be $2\sqrt{2}$). Then, $\lambda = 0$ corresponds the linear lattice, while $\lambda = 1$ gives the quadratic one. Figure 15 shows the dispersion relations for the cases $\lambda \in \{0, 0.5, 0.1\}$; the corresponding values of D_λ are $D_0 = 1, D_{0.5} = \sqrt{2}, D_1 = 1$.

With this setup, we can study how the type of the BTPs affect the transition points. The expectation is that making the BTP quadratic increases the WDoP at the flat band, since the dispersive bands now have a non-zero contribution to the DoS there; as before, the flat band itself does not contribute to the WDoP. This increase in WDoP should lower the critical interaction strength, when the Fermi surface is set to the flat band ($\mu = 0$). In Fig. 16 we present the simulated mean order parameter magnitudes as a function of both J and μ for the cases $\lambda \in \{0, 0.5, 0.1\}$, as well as the corresponding DoS/WDoP curves. This time, the upper bounds for the transition point provided by

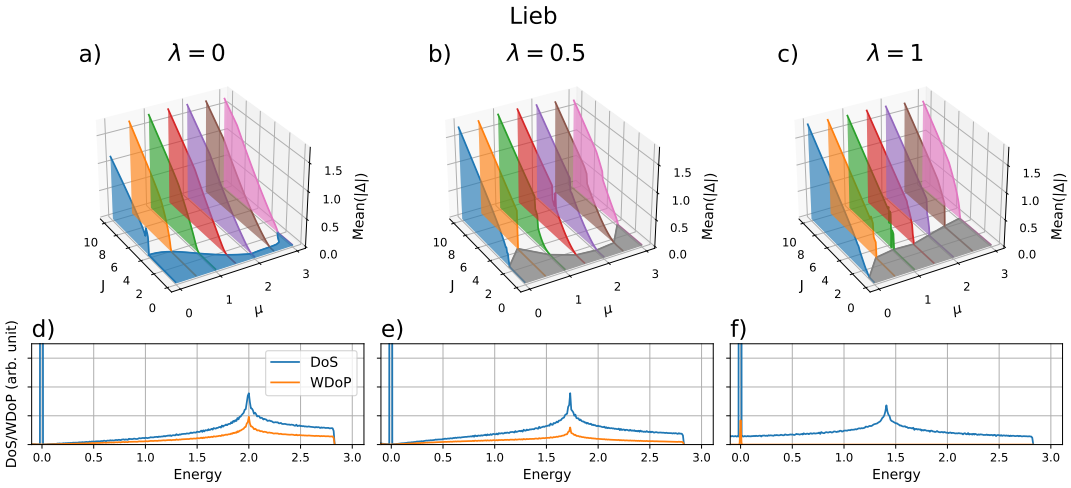

Figure 16: Upper row (a-c): Average real-space order parameter magnitude as a function of the interaction strength J and the chemical potential μ for the Lieb lattice, with RVB interactions, and with three different values of the mixing parameter, $\lambda \in \{0, 0.5, 1\}$. The blue shade at the bottom in (**a**) shows the upper-bound estimates for the transition points obtained with the extended s-wave assumption; for (**b-c**) they are not available because of the modified lattice structure. Instead, the gray shade shows the approximate transition points obtained directly from the simulations. **Lower row (d-f)**: The corresponding densities of states (DoS) and weighted densities of pairs (WDoP). The units for both quantities are arbitrary, and their values should be compared only qualitatively. Note the singularities in the DoS at zero energy, and the absence of those singularities in the WDoP. Due to particle-hole symmetry, only non-negative values of μ are shown.

the extended s-wave assumption are only presented for the case $\lambda = 0$, because for $\lambda \neq 0$ extended s-wave pairing is no longer a possible option for the system due to the unequal on-site energies (see Section 3.2.2 for more discussion). Focusing on the $\mu = 0$ case for each value of λ, we find our expectations confirmed. Tuning the BTPs from linear to quadratic does indeed increase the WDoP at the flat band, and correspondingly, the QCP moves to a significantly lower value of J. What is perhaps surprising, however, is what happens when $\mu \neq 0$. Looking at the fully quadratic case with $\lambda = 1$ in Figs. 16c and 16f, we see that the WDoP is non-zero only at exactly zero energy, and correspondingly in all other cases than $\mu = 0$ the critical value of the interaction strength is quite high. This is a consequence of the fact that in this unrealistic model, in terms of hoppings there are two disconnected sublattices, but interaction happens between the sublattices. Because the sublattices are disconnected, all Bloch states are necessarily localized either on orbital C or on orbitals A and B, but interaction exists only between orbitals C and A, or between orbitals C and B. In other words, any state cannot interact with any other state at the same band, and thus the only places where there are states that can interact at the same energy are the band touching points.

Physically, this model is obscure enough that these odd results for $\mu \neq 0$ need not

be looked too much into, but the case with $\mu = 0$ nicely illustrates mathematically that a QBTP is indeed favorable to a Dirac point when the Fermi surface is at the band touching point.

6 Discussion and Conclusions

The main message of the results presented in this thesis is that nearest-neighbour interactions, such as the RVB pairing considered here, can cause highly non-trivial behaviour regarding whether or not the ground state of a system could be superconducting at low interaction strengths. With the more standard on-site interactions, it is often enough to look at the dispersion relations of the system, as the density of states at the Fermi surface is a good predictor for what happens with weak interactions. Indeed, in both our results and in the literature [14, 15, 42–46], flat bands, where the DoS diverges, tend to enhance pairing at low interaction strengths, while Dirac points, where the DoS vanishes, tends to cause a finite critical interaction strength. In stark contrast, we have shown that with RVB pairing, for the Lieb lattice, the flat band is actually the worst place to put the Fermi energy to (see Fig. 13a), causing the largest possible critical interaction strength. Similarly, for the kagome lattice the largest critical interaction strength occurs when the Fermi surface is at the upper van Hove singularity (see Fig. 11b), where the DoS diverges. The explanation in both of these cases lies in the localization properties of the Bloch states: with nearest-neighbour interactions, particles that form a Cooper pair must be, at least partially, localized on neighboring states.

For the Lieb lattice, the problem is structural: as was shown in Section 3.1, for the class of semi-bipartite lattices with unequal sublattice sizes, the same mechanism that causes these lattices to have a flat band forces the corresponding Bloch states to be completely localized on non-neighboring states, rendering the flat band in this regard of little use. This is quite significant, since flat band models are one of the current paths that are pursued in hopes of finding high-temperature superconductivity, but we have shown that with RVB pairing, for many (but not all) of those models the flat band doesn't really matter.

For the kagome lattice, there are no such problems at the flat band; instead, low-interaction pairing is indeed enhanced compared to the honeycomb lattice (see Fig. 8e), which has the same dispersion relations, but without the flat band. On the other hand, a similar problem occurs for the upper vHS at zero energy, where the DoS also diverges: at the specific points of the Brillouin zone where the vHSs occur, the Bloch states are localized on non-neighboring states. The exact cause for this is, as of yet, unclear. That is, is there some clear structural reason that causes the upper vHS (but, notably, not the lower vHS) to behave in this way? For the Lieb lattice and other lattices fitting the definition of Section 3.1, one can simply look at the lattice structure and understand the problem. Is there something similar happening with the kagome lattice? While we have no clear answer, we have proposed the concept of the weighted density of pairs as a tool to analyze these situations. The WDoP is basically an improved version of the DoS for the purpose of determining the amount of candidate Cooper pairs available at the Fermi surface. As we have shown, the WDoP for the Lieb lattice at the flat band is zero, despite the diverging density of states, correctly reflecting that the states at the flat band cannot interact with each other. The WDoP is also able to correctly spot that something unusual happens with the kagome lattice at the higher vHS.

Having observed that a critical value for the interaction strength exists, the natural question is what exactly this value is, and what it depends on. The second main contribution of this thesis is the derivation of upper bounds for the critical interaction strength in Section 3.2, given by Eqs. (3.27) and (3.42), the first one suitable for on-site interactions, and the other for RVB interactions. These upper bounds are derived using an assumption of a specific pairing symmetry, namely uniform s-wave pairing for on-site interactions, and extended s-wave pairing for RVB interactions. In Section 5.2 we provided numerical results indicating that this upper bound is often quite close to the real critical value, even in cases where the ground state does not have the pairing symmetry in question.

Eqs. (3.27) and (3.42) reinforce the notion that the vicinity of the Fermi surface is the most important portion of the Brillouin zone for enhancing pairing. However, the latter equation, concerning RVB pairing, provides the curious result that states at zero energy would not contribute to pairing, even if they are exactly on the Fermi surface. While already discussed in Section 3.2.2, in light of our numerical results, we will revisit the topic of what is so special about these states. Mathematically, the answer is clear: assuming extended s-wave pairing implies that order parameters vanish at those $\boldsymbol{k}$-points where the single-particle energies are zero. For all four of the lattices considered in this work, it is indeed the case that RVB pairing is suppressed when the Fermi energy is set to zero. In other words, we saw large critical interaction strengths for all lattices when $\mu = 0$. For the π-flux square and honeycomb lattices, the Fermi surface is a collection of Dirac points when $\mu = 0$, and the vanishing DoS explains the suppressed pairing. For the Lieb and kagome lattices, the reasons are related to the localization properties of the Bloch states, as discussed above. The point is that in all of these cases there is an underlying physical reason behind the suppressed pairing, and it is not clear whether Eq. (3.42), derived from an often-incorrect assumption, provides a more general truth of there being a problem with pairing for states at zero energy, or whether this result is just a mathematical artefact of the extended s-wave assumption. As discussed in Section 3.2.2, the zero point of energy is not arbitrary here, since for extended s-wave pairing to be possible in a system with nearest-neighbour interactions, the energy spectrum has to be defined in such a way that the on-site energies for all lattice sites are zero. Does this condition somehow simultaneously inhibit pairing for the states at zero energy in general? On the other hand, the results shown in this thesis cannot rule out the possibility that this is simply a mathematical effect, and that in some other lattice the extended s-wave assumption predicts a large value for the critical interaction strength, while in reality there is some other pairing symmetry that has no such problems.

The matter of possible pairing symmetries brings about an important omission of this work. Using group theory and the symmetries of a given lattice, it is often possible to determine the possible pairing symmetries the order parameters could have directly from the lattice structure. While this is becoming a standard tool in condensed matter physics (see, e.g. Refs. [28, 47, 62] for starters), such analysis has mostly been left outside the scope of this thesis – we have only talked about the uniform s-wave pairing and extended s-wave pairing from a mathematical standpoint. In light of the discussion above, it would be interesting to see what effect (if any) the lattice

symmetries have on how close to the true critical point the extended s-wave prediction is. As a hypothesis, there could, for example, be some pairing symmetry that doesn't have similar problems with zero energy as the extended s-wave pairing, but one that the lattices considered here cannot have. If this was the case, there could be a lattice with this symmetry, where the extended s-wave assumption wildly overestimates the value for the critical interaction strength when $\mu = 0$.

A second natural direction to extend the work done in this thesis towards is the calculation of the superfluid weight with RVB interactions. The main focus of this thesis, the transition from a normal to a BCS or an RVB state, only marks the point where the formation of Cooper pairs is possible. The superfluid weight measures the stability of the pairs, and a non-zero superfluid weight is needed in addition to non-zero order parameters for supercurrent to be possible. The superfluid weight was calculated for a model of twisted bilayer graphene with RVB interactions in Ref. [63], but it was recently shown in Ref. [44] that defining the superfluid weight correctly is a more subtle issue than previously thought. While Ref. [44] gives the corrected equations for the superfluid weight with on-site interactions, it is yet unclear how to do the calculations properly with RVB interactions.

In addition to the points discussed above, we mention a few more possibilities for future work. First, one could widen the selection of lattices to see which other models might have unexpected QCPs with RVB interactions. Second, regarding the RVB model itself, in this work we have only included the attractive nearest-neighbour RVB interaction, obtained as the strong-repulsion limit of the on-site Coulomb repulsion. One could build on this model by adding other interaction terms to the Hamiltonian, such as an explicit on-site repulsion, or next-nearest-neighbour hoppings (and the corresponding RVB terms). Models with such terms were used, e.g., in Refs. [64, 65]. Third, all of our results are based on mean-field approximations. It would be interesting to see the effects of quantum fluctuations by using beyond-mean-field methods, such as dynamical mean-field theory or quantum Monte Carlo simulations. The latter method was used in Refs. [33, 36] for the honeycomb lattice with on-site interactions. In particular, in Ref. [33] a comparison to mean-field results was made showing that while mean-field correctly predicted the existence of a QCP for the honeycomb lattice at half-filling, it underestimated the value of the critical interaction strength, showing that quantum fluctuations can be important to obtain quantitatively accurate results.

As a final summary, in this thesis we have shown how localization properties of the Bloch states can suppress pairing at the Fermi surface and induce a finite critical interaction strength for the BCS transition. This is in particular exemplified by the Lieb and kagome lattices, with the Fermi surface set to the flat band and the upper van Hove singularity, respectively, where such localization prevents a BCS state from forming at low interaction strengths despite a diverging density of states. Correspondingly, we have proposed the concept of weighted density of pairs as an improved measure for the purpose of counting candidate Cooper pairs at the Fermi surface. In addition, we have derived analytical upper bounds for the critical interaction strength for both on-site and RVB pairing. While our results indicate that this upper bound can often be quite close to the true critical value, more work remains to be done regarding when exactly can the upper bound be expected to be a good approximation.

References

[1] K. O. H., "The superconductivity of mercury," *Comm. Phys. Lab. Univ. Leiden*, vol. 122, pp. 122–124, 1911.

[2] M. I. Eremets, V. S. Minkov, A. P. Drozdov, P. P. Kong, V. Ksenofontov, S. I. Shylin, S. L. Bud'ko, R. Prozorov, F. F. Balakirev, D. Sun, and et al., "High-temperature superconductivity in hydrides: Experimental evidence and details," *Journal of Superconductivity and Novel Magnetism*, vol. 35, no. 4, p. 965–977, 2022.

[3] A. P. Drozdov, M. I. Eremets, I. A. Troyan, V. Ksenofontov, and S. I. Shylin, "Conventional superconductivity at 203 Kelvin at high pressures in the sulfur hydride system," *Nature*, vol. 525, no. 7567, p. 73–76, 2015.

[4] Q. Cao, F. Grote, M. Hußmann, and S. Eigler, "Emerging field of few-layered intercalated 2D materials," *Nanoscale Advances*, vol. 3, no. 4, p. 963–982, 2021.

[5] J. G. Bednorz and K. A. Müller, "Possible high T_c superconductivity in the Ba-La-Cu-O system," *Zeitschrift für Physik B Condensed Matter*, vol. 64, no. 2, pp. 189–193, 1986.

[6] J. Nagamatsu, N. Nakagawa, T. Muranaka, Y. Zenitani, and J. Akimitsu, "Superconductivity at 39 K in magnesium diboride," *Nature*, vol. 410, no. 6824, p. 63–64, 2001.

[7] Y. Kamihara, H. Hiramatsu, M. Hirano, R. Kawamura, H. Yanagi, T. Kamiya, and H. Hosono, "Iron-based layered superconductor: LaOFeP," *Journal of the American Chemical Society*, vol. 128, no. 31, p. 10012–10013, 2006.

[8] J. Bardeen, L. N. Cooper, and J. R. Schrieffer, "Theory of superconductivity," *Phys. Rev.*, vol. 108, pp. 1175–1204, Dec. 1957.

[9] L. N. Cooper, "Bound electron pairs in a degenerate Fermi gas," *Phys. Rev.*, vol. 104, pp. 1189–1190, Nov. 1956.

[10] E. Maxwell, "Isotope effect in the superconductivity of mercury," *Phys. Rev.*, vol. 78, pp. 477–477, May 1950.

[11] J. Hubbard and B. H. Flowers, "Electron correlations in narrow energy bands," *Proceedings of the Royal Society of London. Series A. Mathematical and Physical Sciences*, vol. 276, no. 1365, pp. 238–257, 1963.

[12] D. P. Arovas, E. Berg, S. A. Kivelson, and S. Raghu, "The Hubbard model," *Annual Review of Condensed Matter Physics*, vol. 13, pp. 239–274, Mar. 2022.

[13] M. Qin, T. Schäfer, S. Andergassen, P. Corboz, and E. Gull, "The Hubbard model: A computational perspective," *Annual Review of Condensed Matter Physics*, vol. 13, pp. 275–302, Mar. 2022.

[14] T. T. Heikkilä, N. B. Kopnin, and G. E. Volovik, "Flat bands in topological media," *JETP Letters*, vol. 94, pp. 233–239, Oct. 2011.

[15] N. B. Kopnin, T. T. Heikkilä, and G. E. Volovik, "High-temperature surface superconductivity in topological flat-band systems," *Phys. Rev. B*, vol. 83, p. 220503, June 2011.

[16] P. W. Anderson, "The resonating valence bond state in La_2CuO_4 and superconductivity," *Science*, vol. 235, no. 4793, pp. 1196–1198, 1987.

[17] P. Anderson, "Who or what is RVB?," *Physics Today*, vol. 61, pp. 8–9, Apr. 2008.

[18] W. Heisenberg, "Zur Theorie des Ferromagnetismus," *Z. Phys.*, vol. 49, no. 9-10, pp. 619–636, 1928.

[19] K. A. Chao, J. Spałek, and A. M. Oleś, "Canonical perturbation expansion of the Hubbard model," *Phys. Rev. B*, vol. 18, pp. 3453–3464, Oct. 1978.

[20] P. W. Anderson, G. Baskaran, Z. Zou, and T. Hsu, "Resonating–valence-bond theory of phase transitions and superconductivity in la_2cuo_4-based compounds," *Phys. Rev. Lett.*, vol. 58, pp. 2790–2793, June 1987.

[21] G. Baskaran, Z. Zou, and P. Anderson, "The resonating valence bond state and high-T_c superconductivity — a mean field theory," *Solid State Communications*, vol. 63, no. 11, pp. 973–976, 1987.

[22] S. A. Kivelson, D. S. Rokhsar, and J. P. Sethna, "Topology of the resonating valence-bond state: Solitons and high-T_c superconductivity," *Phys. Rev. B*, vol. 35, pp. 8865–8868, June 1987.

[23] T. C. Choy and B. A. McKinnon, "Significance of nonorthogonality in tight-binding models. II. the possibility of high-T_c superconductivity in intercalation compounds," *Phys. Rev. B*, vol. 52, pp. 14539–14543, Nov. 1995.

[24] G. Baskaran, "Resonating-valence-bond contribution to superconductivity in MgB_2," *Phys. Rev. B*, vol. 65, p. 212505, May 2002.

[25] A. M. Black-Schaffer and S. Doniach, "Resonating valence bonds and mean-field d-wave superconductivity in graphite," *Physical Review B*, vol. 75, Apr. 2007.

[26] B. Edegger, V. N. Muthukumar, and C. Gros, "Gutzwiller–RVB theory of high-temperature superconductivity: Results from renormalized mean-field theory and variational Monte Carlo calculations," *Advances in Physics*, vol. 56, no. 6, pp. 927–1033, 2007.

[27] S. Pathak, V. B. Shenoy, and G. Baskaran, "Possible high-temperature superconducting state with a $d + id$ pairing symmetry in doped graphene," *Physical Review B*, vol. 81, Feb. 2010.

[28] A. M. Black-Schaffer, W. Wu, and K. L. Hur, "Chiral d-wave superconductivity on the honeycomb lattice close to the Mott state," *Physical Review B*, vol. 90, Aug. 2014.

[29] G. Baskaran, "Resonating valence bond theory of superconductivity: Beyond cuprates," 2017. arXiv:1709.10070.

[30] P. A. Lee and N. Nagaosa, "Gauge theory of the normal state of high-T_c superconductors," *Phys. Rev. B*, vol. 46, pp. 5621–5639, Sept. 1992.

[31] P. A. Lee and N. Read, "Why is T_c of the oxide superconductors so low?," *Phys. Rev. Lett.*, vol. 58, pp. 2691–2694, June 1987.

[32] Z. Y. Weng, "Why T_c is too high when antiferromagnetism is underestimated?—an understanding based on the phase-string effect," *AIP Conference Proceedings*, vol. 483, no. 1, pp. 147–152, 1999.

[33] S. Sorella and E. Tosatti, "Semi-metal-insulator transition of the Hubbard model in the honeycomb lattice," *Europhysics Letters*, vol. 19, p. 699, Aug. 1992.

[34] B. Uchoa and A. H. Castro Neto, "Superconducting states of pure and doped graphene," *Phys. Rev. Lett.*, vol. 98, p. 146801, Apr. 2007.

[35] N. B. Kopnin and E. B. Sonin, "BCS superconductivity of Dirac electrons in graphene layers," *Phys. Rev. Lett.*, vol. 100, p. 246808, June 2008.

[36] K. L. Lee, K. Bouadim, G. G. Batrouni, F. Hé bert, R. T. Scalettar, C. Miniatura, and B. Grémaud, "Attractive Hubbard model on a honeycomb lattice: Quantum Monte Carlo study," *Physical Review B*, vol. 80, Dec. 2009.

[37] L.-K. Lim, A. Lazarides, A. Hemmerich, and C. M. Smith, "Strongly interacting two-dimensional Dirac fermions," *Europhysics Letters*, vol. 88, p. 36001, Nov. 2009.

[38] G. Mazzucchi, L. Lepori, and A. Trombettoni, "Semimetal–superfluid quantum phase transitions in 2D and 3D lattices with Dirac points," *Journal of Physics B: Atomic, Molecular and Optical Physics*, vol. 46, p. 134014, June 2013.

[39] F. Parisen Toldin, M. Hohenadler, F. F. Assaad, and I. F. Herbut, "Fermionic quantum criticality in honeycomb and π-flux Hubbard models: Finite-size scaling of renormalization-group-invariant observables from quantum Monte Carlo," *Phys. Rev. B*, vol. 91, p. 165108, Apr. 2015.

[40] E. G. Santos, J. R. Iglesias, C. Lacroix, and M. A. Gusmão, "A two-band model for superconductivity in the checkerboard lattice," *Journal of Physics: Condensed Matter*, vol. 22, p. 215701, Apr. 2010.

[41] S. Peotta and P. Törmä, "Superfluidity in topologically nontrivial flat bands," *Nature Communications*, vol. 6, p. 8944, Nov. 2015.

[42] A. Julku, S. Peotta, T. I. Vanhala, D.-H. Kim, and P. Törmä, "Geometric origin of superfluidity in the Lieb-lattice flat band," *Phys. Rev. Lett.*, vol. 117, p. 045303, July 2016.

[43] L. Liang, T. I. Vanhala, S. Peotta, T. Siro, A. Harju, and P. Törmä, "Band geometry, Berry curvature, and superfluid weight," *Phys. Rev. B*, vol. 95, p. 024515, Jan. 2017.

[44] K.-E. Huhtinen, J. Herzog-Arbeitman, A. Chew, B. A. Bernevig, and P. Törmä, "Revisiting flat band superconductivity: Dependence on minimal quantum metric and band touchings," *Phys. Rev. B*, vol. 106, p. 014518, July 2022.

[45] J. Herzog-Arbeitman, A. Chew, K.-E. Huhtinen, P. Törmä, and B. A. Bernevig, "Many-body superconductivity in topological flat bands," 2022.

[46] P. Törmä, S. Peotta, and B. A. Bernevig, "Superconductivity, superfluidity and quantum geometry in twisted multilayer systems," *Nature Reviews Physics*, vol. 4, pp. 528–542, Aug. 2022.

[47] D. Călugăru, A. Chew, L. Elcoro, Y. Xu, N. Regnault, Z.-D. Song, and B. A. Bernevig, "General construction and topological classification of crystalline flat bands," *Nature Physics*, vol. 18, pp. 185–189, Dec. 2021.

[48] J. R. Schrieffer and P. A. Wolff, "Relation between the Anderson and Kondo hamiltonians," *Phys. Rev.*, vol. 149, pp. 491–492, Sept. 1966.

[49] S. Bravyi, D. P. DiVincenzo, and D. Loss, "Schrieffer–Wolff transformation for quantum many-body systems," *Annals of Physics*, vol. 326, pp. 2793–2826, Oct. 2011.

[50] M. Noga, "Superconductivity in heavy electron metals," *Czechoslovak Journal of Physics B*, vol. 38, pp. 210–223, Feb. 1988.

[51] N. N. Bogoljubov, V. V. Tolmachov, and D. V. Širkov, "A new method in the theory of superconductivity," *Fortschritte der Physik*, vol. 6, no. 11-12, pp. 605–682, 1958.

[52] P. Pulay, "Convergence acceleration of iterative sequences. The case of SCF iteration," *Chemical Physics Letters*, vol. 73, no. 2, pp. 393–398, 1980.

[53] R. Shepard and M. Minkoff, "Some comments on the DIIS method," *Molecular Physics*, vol. 105, no. 19-22, pp. 2839–2848, 2007.

[54] B. I. Reser, "On the Brillouin zone integration," *Physica Status Solidi (b)*, vol. 116, no. 1, pp. 31–40, 1983.

[55] M. Methfessel and A. T. Paxton, "High-precision sampling for Brillouin-zone integration in metals," *Phys. Rev. B*, vol. 40, pp. 3616–3621, Aug. 1989.

[56] P. E. Blöchl, O. Jepsen, and O. K. Andersen, "Improved tetrahedron method for Brillouin-zone integrations," *Phys. Rev. B*, vol. 49, pp. 16223–16233, June 1994.

[57] D. Zaharioudakis, "Tetrahedron methods for Brillouin zone integration," *Computer Physics Communications*, vol. 157, no. 1, pp. 17–31, 2004.

[58] M. Kawamura, Y. Gohda, and S. Tsuneyuki, "Improved tetrahedron method for the Brillouin-zone integration applicable to response functions," *Phys. Rev. B*, vol. 89, p. 094515, Mar. 2014.

[59] M. L. Kiesel and R. Thomale, "Sublattice interference in the kagome Hubbard model," *Phys. Rev. B*, vol. 86, p. 121105, Sept. 2012.

[60] W.-S. Wang, Z.-Z. Li, Y.-Y. Xiang, and Q.-H. Wang, "Competing electronic orders on kagome lattices at van Hove filling," *Phys. Rev. B*, vol. 87, p. 115135, Mar. 2013.

[61] A. Graf and F. Piéchon, "Designing flat-band tight-binding models with tunable multifold band touching points," *Phys. Rev. B*, vol. 104, p. 195128, Nov. 2021.

[62] A. Zee, *Group theory in a nutshell for physicists*. Princeton University Press, 2016.

[63] A. Julku, T. J. Peltonen, L. Liang, T. T. Heikkilä, and P. Törmä, "Superfluid weight and Berezinskii-Kosterlitz-Thouless transition temperature of twisted bilayer graphene," *Phys. Rev. B*, vol. 101, p. 060505, Feb. 2020.

[64] M. L. Kiesel, C. Platt, W. Hanke, D. A. Abanin, and R. Thomale, "Competing many-body instabilities and unconventional superconductivity in graphene," *Phys. Rev. B*, vol. 86, p. 020507, July 2012.

[65] C. Honerkamp, "Density waves and Cooper pairing on the honeycomb lattice," *Phys. Rev. Lett.*, vol. 100, p. 146404, Apr. 2008.